

An Experimental Study of the decay

$$D^0 \rightarrow K^- K^- K^+ \pi^+$$

by

Shiral C. Devmal

May 2000

University of Cincinnati

High Energy Physics

An Experimental Study of the decay

$$D^0 \rightarrow K^- K^- K^+ \pi^+$$

A dissertation submitted to the

Division of Research and Advanced Studies
of the University of Cincinnati

in partial fulfillment of the
requirements for the degree of

DOCTORATE OF PHILOSOPHY (Ph.D.)

in the Department of Physics
of the College of Arts and Science

May 2000

by

Shiral C. Devmal

B.Sc., University of Colombo, Sri Lanka, 1991

M.Sc., University of Cincinnati, 1995

Committee Chair: Michael D. Sokoloff

Abstract

An Experimental Study of the Decay $D^0 \rightarrow K^- K^- K^+ \pi^+$

by

Shiral C. Devmal

Using data from the E791 experiment at Fermi National Accelerator Laboratory (Fermilab), we have studied the Cabibbo favored, but phase space suppressed decay $D^0 \rightarrow K^- K^- K^+ \pi^+$ with the normalization channel $D^0 \rightarrow K^- \pi^- \pi^+ \pi^+$. We report the branching ratio of $D^0 \rightarrow K^- K^- K^+ \pi^+$ relative to the branching ratio of $D^0 \rightarrow K^- \pi^- \pi^+ \pi^+$. This value is $(0.54 \pm 0.13 \pm 0.07)\%$. We see a clear signal of $K^- K^+$ resonance in the decay $D^0 \rightarrow K^- K^- K^+ \pi^+$ from which we conclude that about $(60 \pm 30)\%$ of $KKK\pi$ comes from $D^0 \rightarrow \phi K^- \pi^+; \phi \rightarrow K^- K^+$. We also set the range $(0.30\% - 0.90\%)$ for the ratio $P_{q\bar{q}}/P_{NoPop}$ where $P_{q\bar{q}}$ is the contribution from either $D^0 \rightarrow K^- K^- K^+ \pi^+$ terms that pop an $s\bar{s}$ or corresponding $D^0 \rightarrow K^- \pi^- \pi^+ \pi^+$ terms that pop either $u\bar{u}$ or $d\bar{d}$ pair and P_{NoPop} is the contributions from the $D^0 \rightarrow K^- \pi^- \pi^+ \pi^+$ terms that do not have such corresponding popping.

Acknowledgments

It has been a wonderful experience reading for a Ph.D. in physics. I express my sincere gratitude to the Department of Physics at the University of Cincinnati for giving me the privilege for pursuing graduate studies in physics and am also thankful to the US government and the American public for welcoming me to the USA. My special thanks go to Professor Mike Sokoloff for being my thesis adviser, his lessons in experimental particle physics, his generous help both professionally and personally, and being there whenever I needed him. I should also thank Professor Brian Meadows for being my co-advisor, giving me a good start in research, advising me for the work I did in BaBar experiment at SLAC, and various help he has given to me. I also thank Professors Peter Suranyi and Howard Jackson for serving in my thesis committee and Professors Randy Johnson and Alan Schwartz and all the other professors in the Physics Department for various help they have given to me. I am also grateful to Peg Frantz, Melody Whitlock, Lynne McEneny, Donna Deutenberg, David Will and all the other staff members in the Physics Department for the help given and the courtesy they have shown to me.

My sincere thanks are also due to Jeff Appel and Milind Purohit for closely following my work and making comments and suggestions. I also thank Jean Slaughter, Lucien Cremaldi, Ray Stefanski, and Howard Rubin for their comments and sugges-

tions. My thanks to Lalith Perera and Kevin Stenson for the help given to me during the analysis. I thank all the E791 collaborators for welcoming me to the collaboration and helping me in various ways. I am also grateful to the Fermilab technical staff for the courtesy and support they gave me during the time I read data.

I am also grateful to Terry Geld, Ted Fieguth, Martin Nordby, and Mike Sullivan for the help they gave me when I was working in BaBar experiment at SLAC. I extend my sincere gratitude to Professor Mara Helmuth for making my graduate years even more enjoyable by giving me the opportunity to learn electronic and computer music at CCM. My thanks also go to all my teachers for sharing their knowledge with me.

I am truly grateful to my parents for their guidance, encouragement, protection, love, and care. I extend my sincere gratitude to my wife for her loving care, encouragement, patience, and being my best friend. I am also grateful to my brothers and sisters for being there in happiness and sorrow and also to their families for all the help they gave. My thanks also go to my special aunt who helped me so much when I was in college. I thank all my relatives and friends for various help they have given to me. I sincerely thank Professor Mike Sokoloff, Professor Paul Shanley of University of Notre Dame, and my friends Rohana, Jagath, and Chandima for helping me at a time I really needed it. Finally, I would like to thank all of you who have helped me in various ways; I am sure you all know that I am grateful to you.

Contents

1	Introduction	1
1.1	Standard Model	2
1.1.1	Type of Constituents	3
1.1.2	Types of Interactions	4
1.1.3	Weak Interaction and CKM Matrix	6
1.2	Weak Decay of Charm Quark	8
1.2.1	Tree Level Decay Models	9
1.2.2	Hadronic, Semileptonic, and Leptonic Decays	11
1.2.3	Cabibbo Favored and Single and Doubly Suppressed Cabibbo Decays	12
1.3	The Decay $D^0 \rightarrow K^- K^- K^+ \pi^+$	12
2	The E791 Experiment	16

2.1	History of TPL Spectrometer	16
2.2	Why Fixed Target	18
2.3	The E791 Coordinate System	19
2.4	The Beam	20
2.5	TPL Spectrometer	21
2.5.1	The Beam Tracking System	24
2.5.2	The Target	25
2.5.3	Interaction Trigger Counter	27
2.5.4	Downstream SMD Planes	27
2.5.5	Downstream PWC Planes	30
2.5.6	Drift Chambers	30
2.5.7	Analysis Magnets (M1 and M2)	31
2.5.8	Čerenkov Counters	33
2.5.9	Calorimeters	33
2.5.10	Muon Wall	36
2.6	Trigger and Data Acquisition	37
3	Event Reconstruction and Selection	39
3.1	Track Reconstruction	40
3.1.1	ESTR and SESTR Tracks	43

3.1.2	Track Category	43
3.2	Topological Vertex Reconstruction	44
3.3	Particle Identification	45
3.4	Event Selection	46
3.4.1	Event Parameters	47
3.4.2	Filtering	53
3.4.3	Stripping	54
3.4.4	Substripping	54
3.4.5	Microstripping	55
4	Optimizing Event Selection Criteria	58
4.1	The Blind Analysis	59
4.2	Monte Carlo Data	59
4.3	Optimizing Analysis Cuts	61
4.3.1	Signal and Background Distributions	61
4.3.2	Plots of Sensitivity vs. Cut	62
4.3.3	FOM: The Figure of Merit	64
4.4	Cuts before FOM	65
4.4.1	DIP	65
4.4.2	SDZ	67

4.4.3	CVK, PCVK, and CVP	69
4.4.4	PTBL	73
4.4.5	SDCA	75
4.4.6	SDZT	77
4.4.7	PTSQ and SPTSQ	79
4.4.8	DELZ and ISOL	84
4.4.9	CHIS and CHIP	87
4.4.10	COSSP	89
4.4.11	CATs and RATs	89
4.4.12	TAU	91
4.5	FOM: Figure of Merit	91
4.5.1	Optimizing Sensitivity	92
4.5.2	Event Parameters Selected	95
4.5.3	Signal and Background Discrimination	102
4.5.4	Systematic Uncertainty due to Correlations	107
4.6	Optimizing the FOM Cut	109
4.6.1	Estimating the Expected Number of Signal Events	110
4.6.2	Estimating the Expected Number of Background Events	113
4.6.3	The Three Types of FOM	113

4.6.4	Selecting the Optimal FOM Cut	114
4.7	The Optimized Cuts for $D^0 \rightarrow K^- K^- K^+ \pi^+$	122
5	Branching Ratio and Resonance Structure	124
5.1	Branching Ratio of $D^0 \rightarrow K^- K^- K^+ \pi^+$	125
5.2	Efficiency Corrections and Systematic Errors	128
5.2.1	Statistical Fluctuations in Monte Carlo Data	130
5.2.2	Difference in Monte Carlo and Real Data	132
5.2.3	FOM Predictions	145
5.2.4	Signal and Background Shape	147
5.2.5	$D^0 \rightarrow \phi K^- \pi^+$	149
5.2.6	In Summary	152
5.3	KK Resonance	153
6	Conclusions	159
A	Sphericity	163
B	Kaon Čerenkov Efficiencies	165

List of Figures

1.1	Tree level Feynman diagrams for charm decay	10
1.2	Examples of Cabibbo favored (a), singly Cabibbo suppressed (b), and doubly Cabibbo suppressed (c) decays.	13
1.3	Some of the Feynman Diagrams that contribute to the decays $D^0 \rightarrow$ $K^- K^- K^+ \pi^+$ and $D^0 \rightarrow K^- \pi^- \pi^+ \pi^+$	15
2.1	E791 Detector Coordinate System.	19
2.2	TPL Spectrometer	22
2.3	Types of particles each detector type detects.	23
2.4	E791 target and interaction trigger counter region	28
3.1	The geometry of a decay	47
3.2	$KKK\pi$ mass with microstrip cuts	57

4.1	DIP distributions of SEED4 $KKK\pi$ and $K\pi\pi\pi$ signal and background events and the variation of $KKK\pi$ sensitivity with the DIP cut. . . .	63
4.2	DIP distributions of SEED3 $KKK\pi$ and $K\pi\pi\pi$ signal and background events and the variation of $KKK\pi$ sensitivity with the DIP cut. . . .	66
4.3	SDZ distributions of SEED4 $KKK\pi$ and $K\pi\pi\pi$ signal and background events and the variation of $KKK\pi$ sensitivity with the SDZ cut. . . .	67
4.4	SDZ distributions of SEED3 $KKK\pi$ and $K\pi\pi\pi$ signal and background events and the variation of $KKK\pi$ sensitivity with the SDZ cut. . . .	68
4.5	SEED4 and SEED3 σ_z distribution of $KKK\pi$ and $K\pi\pi\pi$ signal events.	69
4.6	CVK distributions of SEED4 $KKK\pi$ signal and background events and $K\pi\pi\pi$ signal events.	70
4.7	CVK distributions of SEED3 $KKK\pi$ signal and background events and $K\pi\pi\pi$ signal events.	71
4.8	SEED4 and SEED3 product CVK (PCVK) distributions of $KKK\pi$ signal and background events.	72
4.9	PTBL distributions of SEED4 $KKK\pi$ and $K\pi\pi\pi$ signal and background events and the variation of $KKK\pi$ sensitivity with the PTBL cut.	74

4.10 PTBL distributions of SEED3 $KKK\pi$ and $K\pi\pi\pi$ signal and background events and the variation of $KKK\pi$ sensitivity with the PTBL cut.	75
4.11 SEED4 and SEED3 SDCA distributions of $KKK\pi$ signal and background events and sensitivity vs. SDCA cut.	76
4.12 SEED4 and SEED3 SDZT distributions of $KKK\pi$ and $K\pi\pi\pi$ signal and background events and SEED4 sensitivity vs. SDCA cut.	78
4.13 PTSQ distributions of SEED4 $KKK\pi$ and $K\pi\pi\pi$ signal and background events, sensitivity vs. PTSQ cut, and PTSQ vs. $KKK\pi$ mass distribution for SEED4 Monte Carlo signal and real data background events.	80
4.14 SPTSQ distributions of SEED4 $KKK\pi$ and $K\pi\pi\pi$ signal and background events, sensitivity vs. PTSQ cut, and SPTSQ vs. $KKK\pi$ mass distribution for SEED4 Monte Carlo signal and real data background events.	81
4.15 PTSQ distributions of SEED3 $KKK\pi$ and $K\pi\pi\pi$ signal and background events, sensitivity vs. PTSQ cut, and PTSQ vs. $KKK\pi$ mass distribution for SEED3 Monte Carlo signal and real data background events.	82

4.16	SPTSQ distributions of SEED3 $KKK\pi$ and $K\pi\pi\pi$ signal and background events, sensitivity vs. PTSQ cut, and SPTSQ vs. $KKK\pi$ mass distribution for SEED3 Monte Carlo signal and real data background events.	83
4.17	SEED4 and SEED3 DELZ vs. ISOL scatter plots of $KKK\pi$ Monte Carlo signal and real data background events.	84
4.18	SEED4 and SEED3 CHIS distribution of $KKK\pi$ signal and background events, the plot of sensitivity vs. CHIS cut for SEED3 $KKK\pi$ events, and CHIS distributions for SEED3 $KKK\pi$ signal events. . . .	88
4.19	SEED4 and SEED3 COSSP distributions of $KKK\pi$ signal and background events and sensitivity vs. SDCA cut.	90
4.20	SEED4 $KKK\pi$ CVK Monte Carlo signal and real data background distributions of the events that pass and fail an FOM cut at .5. . . .	103
4.21	SEED4 $KKK\pi$ DIP and COSSP Monte Carlo signal and real data background distributions of the events that pass and fail an FOM cut at .5.	104
4.22	SEED3 $KKK\pi$ CVK Monte Carlo signal and real data background distributions of the events that pass and fail an FOM cut at 1.	105

4.23	SEED3 $KKK\pi$ DIP, MRAT, and COSSP Monte Carlo signal and real data background distributions of the events that pass and fail an FOM cut at 1.	106
4.24	SEED4 and SEED3 $KKK\pi$ FOM Monte Carlo signal and real data background distributions on semilog plots.	107
4.25	Mass histograms for $K\pi\pi\pi$ real and Monte Carlo data.	111
4.26	SEED4 $KKK\pi$ Monte Carlo signal and real data background distributions before and after the optimized FOM cut $FOM > 0.5$	120
4.27	SEED3 $KKK\pi$ Monte Carlo signal and real data background distributions before and after the optimized FOM cut $FOM > 1.0$	121
5.1	Mass distributions of real data $KKK\pi$ events, real data $K\pi\pi\pi$ events, Monte Carlo $KKK\pi$ events, and Monte Carlo $K\pi\pi\pi$ events with optimized cuts applied.	126
5.2	SEED4 and SEED3 mass histograms made by running $D^0 \rightarrow K^- K^- K^+ \pi^+$ analysis algorithm on Monte Carlo $D^0 \rightarrow \phi K^- \pi^+$; $\phi \rightarrow K^- K^+$ data with final cuts.	150
5.3	KK mass histograms from $KKK\pi$ decays. The histograms were made from real data, $D^0 \rightarrow \phi K^- \pi^+$; $\phi K\pi$ Monte Carlo data, and non-resonant $D^0 \rightarrow K^- K^- K^+ \pi^+$ Monte Carlo data.	156

5.4	KK mass distribution from real data and that from a toy model showing individual contributions according according to the model.	157
5.5	KK mass distribution from real data and that from a toy model showing total contribution according according to the model.	158

List of Tables

1.1	Classification of the elementary particles.	3
1.2	The masses and the weak-decay lifetimes of the constituents	4
1.3	Interaction types according to the Standard Model	5
1.4	Hadronic, Semileptonic, and Leptonic Decays.	11
2.1	The numbers of charm events reconstructed at the Tagged Photon Laboratory at Fermilab.	17
2.2	Characteristics of the Proportional Wire Chambers (PWCs) in the beam tracking system	24
2.3	Characteristics of the Silicon Microstrip Detectors (SMDs) in the beam tracking system.	25
2.4	Characteristics of the E791 target	26
2.5	Characteristics of the downstream SMD planes	29
2.6	Characteristics of the Drift Chamber Assemblies	31

2.7	Characteristics of the analysis magnets	32
2.8	Characteristics of the Čerenkov counters.	34
2.9	Characteristics of the SLIC	35
2.10	Characteristics of the hadron calorimeter	36
3.1	Number of events reconstructed at different computer farms.	40
3.2	Common category values of the tracks that have hits in adjacent DCs	44
3.3	Estimated <i>a priori</i> probabilities for electrons, muons, pions, kaons, and protons.	46
3.4	Cuts used at Microstrip Level	56
4.1	SEED4 Monte Carlo $KKK\pi$ and $K\pi\pi\pi$ signal fractions with DELZ and ISOL.	86
4.2	SEED4 real data $K\pi\pi\pi$ signal fractions and $KKK\pi$ background frac- tions with DELZ and ISOL.	86
4.3	SEED3 real data $K\pi\pi\pi$ signal fractions and $KKK\pi$ background frac- tions with DELZ and ISOL.	87
4.4	FOM with one parameter (SEED4 DIP)	92
4.5	SPROBs, BPROBs, and FOM for DIP, CVK1, and DIP and CVK1 space.	94

4.6	SEED4 FOM from CVK1 alone along with the CVK1 ranges and CVK1 SPROBs and BPROBs used in SEED4 FOM.	97
4.7	SEED4 FOM from CVK2 alone along with the CVK2 ranges and CVK2 SPROBs and BPROBs used in SEED4 FOM.	97
4.8	SEED4 FOM from CVK3 alone along with the CVK3 ranges and CVK3 SPROBs and BPROBs used in SEED4 FOM.	98
4.9	SEED4 FOM from DIP alone along with the DIP ranges and DIP SPROBs and BPROBs used in SEED4 FOM.	98
4.10	SEED4 FOM from COSSP alone along with the COSSP ranges and COSSP SPROBs and BPROBs used in SEED4 FOM.	99
4.11	SEED3 FOM from CVK1 alone along with the CVK1 ranges and CVK1 SPROBs and BPROBs used in SEED3 FOM.	99
4.12	SEED3 FOM from CVK2 alone along with the CVK2 ranges and CVK2 SPROBs and BPROBs used in SEED3 FOM.	100
4.13	SEED3 FOM from CVK3 alone along with the CVK3 ranges and CVK3 SPROBs and BPROBs used in SEED3 FOM.	100
4.14	SEED3 FOM from DIP alone along with the DIP ranges and DIP SPROBs and BPROBs used in SEED3 FOM.	101

4.15 SEED3 FOM from COSSP alone along with the COSSP ranges and COSSP SPROBs and BPROBs used in SEED4 FOM.	101
4.16 SEED3 FOM from COSSP alone along with the COSSP ranges and COSSP SPROBs and BPROBs used in SEED4 FOM.	101
4.17 SEED4 signal and background fractions calculated directly from the FOM grid, “S (cell)” and “B (cell)” respectively, signal fractions from $KKK\pi$ Monte Carlo plots, “S (plot)”, background fractions from $KKK\pi$ real data histograms, “B (plot)” and the estimated system- atic uncertainty associated with signal and background estimates due to parameter correlations in FOM, ΔS_{sys} and ΔB_{sys} respectively. . .	109
4.18 SEED3 signal and background fractions calculated directly from the FOM grid, “S (cell)” and “B (cell)” respectively, signal fractions from $KKK\pi$ Monte Carlo plots, “S (plot)”, background fractions from $KKK\pi$ real data histograms, “B (plot)” and the estimated system- atic uncertainty associated with signal and background estimates due to parameter correlations in FOM, ΔS_{sys} and ΔB_{sys} respectively. . .	110
4.19 Expected number of SEED4 $KKK\pi$ signal and background events for various SEED4 FOM cuts.	115

4.20	Expected number of SEED3 $KKK\pi$ signal and background events for various SEED3 FOM cuts.	116
4.21	Expected number of total (SEED4 and SEED3 combined) $KKK\pi$ signal events and background events for various SEED3 FOM cuts. SEED4 FOM cut has been fixed at $\text{FOM} > 0.1$. The top row shows the results with no FOM cut at all.	117
4.22	Expected number of total (SEED4 and SEED3 combined) $KKK\pi$ signal events and background events for various SEED3 FOM cuts. SEED4 FOM cut has been fixed at $\text{FOM} > 0.2$	118
4.23	Expected number of total (SEED4 and SEED3 combined) $KKK\pi$ signal events and background events for various SEED3 FOM cuts. SEED4 FOM cut has been fixed at $\text{FOM} > 0.5$	118
4.24	Expected number of total (SEED4 and SEED3 combined) $KKK\pi$ signal events and background events for various SEED3 FOM cuts. SEED4 FOM cut has been fixed at $\text{FOM} > 1.0$	119
4.25	Expected number of total (SEED4 and SEED3 combined) $KKK\pi$ signal events and background events for various SEED3 FOM cuts. SEED4 FOM cut has been fixed at $\text{FOM} > 1.5$	119
4.26	The optimized cuts for $D^0 \rightarrow K^- K^- K^+ \pi^+$	123

5.1	Real data and Monte Carlo data $3K\pi$ and $K3\pi$ mass histogram fit results. All the tuned cuts have been applied.	127
5.2	Monte Carlo and real data $KKK\pi$ signal with tuned cuts and real data $K\pi\pi\pi$ signal with $K\pi\pi\pi$ box cuts.	130
5.3	Observed and estimated number of Monte Carlo $KKK\pi$ and $K\pi\pi\pi$ signal events with and without $CVK > .2$ cuts along with the \check{C} erenkov efficiencies. The estimation has been done using \check{C} erenkov efficiencies of real data.	139
5.4	$K\pi\pi\pi$ Monte Carlo and real data SDZ averages obtained with final cuts, their differences, and the modified $K\pi\pi\pi$ SDZ cut used in estimating the systematic uncertainty.	140
5.5	Average SIGMA of $KKK\pi$ and $K\pi\pi\pi$ Monte Carlo data with final cuts, ratio of the latter to the former, estimated difference between Monte Carlo and real data $KKK\pi$ SDZ averages, and the modified $KKK\pi$ SDZ cut.	141
5.6	Number of Monte Carlo $KKK\pi$ and $K\pi\pi\pi$ signal events obtained with the modified SDZ cuts and the other final cuts.	142
5.7	The $K\pi\pi\pi$ PTBL averages of Monte Carlo and real data with final cuts, their difference, and modified $K\pi\pi\pi$ PTBL cuts.	143

5.8	The average PTBL of $K\pi\pi\pi$ and $KKK\pi$ Monte Carlo data, estimated difference between average PTBL of $KKK\pi$ real and Monte Carlo data, and the modified $KKK\pi$ PTBL cuts.	144
5.9	Number of Monte Carlo $KKK\pi$ and $K\pi\pi\pi$ signal events with modified PTBL cut and other final cuts.	144
5.10	$KKK\pi$ predicted signal and background with the optimized cuts and the three types of Monte Carlo.	146
5.11	$KKK\pi$ real data fit results for different signal and background shapes.	148
5.12	Number of signal events obtained by fitting the mass histograms made by running the $D^0 \rightarrow K^- K^- K^+ \pi^+$ analysis algorithm on Monte Carlo $D^0 \rightarrow K^- K^- K^+ \pi^+$ data and $D^0 \rightarrow \phi K^- \pi^+$; $\phi \rightarrow K^- K^+$ data. . . .	151
5.13	Summary of corrections to the relative efficiency from Monte Carlo for reconstructing $KKK\pi$ and $K\pi\pi\pi$ final states.	152
5.14	Summary of systematic errors. The total has been calculated by adding the individual contributions in quadrature.	153
B.1	Kaon \check{C} erenkov efficiencies at $CVK > 0.2$ for a set of p and p_T ranges.	166

Chapter 1

Introduction

Though the Standard Model of particle physics [1] has shown much success in describing the fundamental constituent particles and the fundamental interactions in nature, the knowledge in that has been far from being complete. Besides the two lightest quarks: the *up* quark and the *down* quark and the lightest lepton: the *electron*, that constitute the stable material we encounter in real world, the Standard Model includes four more exotic quarks and more leptons. The *charm* quark, being the lightest of the three heavy quarks, has been a focus of research for several years in such studies due to its relatively easy production compared to producing the other two heavy quarks: the *bottom* quark and the *top* quark. The E791 experiment conducted at the Fermi National Accelerator Laboratory (Fermilab) is one such experiment that produced 20 billion events as the basis for a series of studies in charm physics.

In this thesis, I present a detailed study of the Cabibbo-favored charm decay $D^0 \rightarrow K^- K^- K^+ \pi^+$, which is suppressed by phase space restrictions due to low Q value, using data from E791 and estimate its branching ratio with respect to the topologically similar normalization channel, $D^0 \rightarrow K^- \pi^- \pi^+ \pi^+$. A theoretical picture for multibody decays is not yet complete due to the complexity of the calculation that arises from the strong interaction between the produced hadrons and pre-decay and post-decay gluon exchange among the quarks. Experimental evidence shows that most multibody decays go through one or more quasi-two-body or other resonant states. To understand these phenomena, it is important to study multi-body decays of heavy particles.

1.1 Standard Model

The Standard Model of particle physics is the most successful description that has emerged so far in describing the fundamental constituents of the matter and the laws that govern their interactions. At a macroscopic level, this model has explained most of nature's physical phenomena. According to the Standard Model, the elementary particles can be divided into two classes: constituents and mediators. These constituents —as the word implies— form the matter in nature while the exchange of mediators governs the interaction between the constituents.

1.1.1 Type of Constituents

According to the Standard Model, constituent particles further divide into two groups: *leptons* and *quarks*, which are both *fermions*, depending on whether or not they take part in strong interactions; quarks take part in strong interactions, but leptons do not. Though these are all spin one-half particles, each one has either different mass or different charge or both that makes each particle unique. They also show different ranges in their lifetimes. The leptons and quarks are, somehow, seen as coming from three generations: first, second, and third. Table 1.1 shows the classification of the quarks and the leptons according to generation and charge. Table 1.2 shows the masses and the weak-decay lifetimes of quarks and leptons.

Generation				
	First	Second	Third	Charge
Quarks	up (u)	charm (c)	top (t)	1/3
	down (d)	strange (s)	bottom (b)	-2/3
Leptons	e neutrino (ν_e)	μ neutrino (ν_μ)	τ neutrino (ν_τ)	0
	electron (e)	muon (μ)	tau (τ)	-1

Table 1.1: The first two rows show the quarks and the second two rows show the leptons. They are all spin half particles (fermions). In weak interaction, the leptons shown in the fourth row always come coupled with their counterpart neutrino shown in the third row.

quark	mass	τ_{weak}	lepton	mass	τ_{weak}
u	(2-8) MeV	∞	ν_e	0	∞
d	(5-15) MeV	10^3	e	.511 MeV	∞
c	(1.0-1.6) GeV	10^{-10}	ν_μ	0	∞
s	(0.1-0.3) GeV	10^{-13}	μ	106 MeV	10^{-6}
t	(180 \pm 12) GeV		ν_τ	0	∞
b	(4.1-4.5) GeV		τ	1.8 GeV	10^{-13}

Table 1.2: The masses and the weak-decay lifetimes of the constituents. The first, the second, and the third row respectively correspond to the first, the second, and the third generations.

1.1.2 Types of Interactions

The Standard Model of particle physics describes three types of interactions: strong, electromagnetic, and weak. The photon is the mediator gauge boson for electromagnetic interaction while W^\pm and Z^0 are responsible for the weak interaction. Further, there are eight gluons which are responsible for the strong interaction. These are all spin 1 particles. The Standard Model also predicts at least one Higgs boson which is a spin 0 mediator particle that results from the so-called spontaneous symmetry breaking mechanism that generates non-zero masses for W^\pm and Z^0 . These particles are too massive to create in the existing particle accelerators (Table 1.3).

Interaction Type	Rel. Strength	Mediator ($S = 1$)	Participants
Strong	1	8 gluons (g)	quarks and gluons
Electromagnetic	10^{-3}	Photons (γ)	charged particles
Weak	10^{-14}	W^\pm and Z^0	all but γ and g
Gravity	10^{-43}	Gravitons	All

Table 1.3: Interaction types according to the Standard Model. All mediator bosons have spin 1. The relative strengths that have been given in the table are calculated at proton mass. Gravity is not yet included in the picture, but has been included in the table for comparison. The Standard Model also predicts at least one Higgs boson whose spin is 0.

Table 1.3 summarizes the three interaction types strong, electromagnetic, and weak, that the Standard Model has so far addressed, and gravity. In Quantum Field Theory, which is the theoretical framework of particle physics, this is an $SU(3) \times SU(2) \times SU(1)$ gauge field theory that incorporates strong, electromagnetic, and weak interactions. Gravity is included in the table for comparison, but has not yet been addressed in the Standard Model. All the quarks and the gluons come in three colors. According to the Standard Model, all the isolated particles must be in colorless combinations.

Each particle that has been described so far also has its antiparticle¹. All in all, according to the Standard Model, there are 12 leptons, 36 quarks, and 12 mediators, and at least 1 Higgs boson.

¹Some zero charge particles are said to be their own antiparticle (*e.g.* π^0).

1.1.3 Weak Interaction and CKM Matrix

All the elementary particles except photons and gluons experience weak interactions which are mediated by W^\pm and Z^0 bosons coupled to the fermions which are either leptons or quarks. As first suggested by Bludman [2] in 1958 and later observed at CERN [3] in 1973, the Z^0 facilitates flavor conserving neutral current interactions. Whatever fermion goes in before the interactions emerges without change after the interaction².

The W^\pm facilitates flavor-changing charged-current interactions which is the case in the analysis presented in this thesis, $D^0 \rightarrow K^- K^- K^+ \pi^+$. The eigenstates-states of the Hamiltonian that describes this kind of interaction differ from the flavor eigenstates-states: d , s , and b , so as to give a set of weak eigenstates-states: d' , s' , and b' each of which is in turn a linear combination of d , s , and b . The matrix that connects these two sets is known as the Cabibbo, Kobayashi, Maskawa (CKM) matrix [6] which is given by,

$$\begin{pmatrix} d' \\ s' \\ b' \end{pmatrix} = \begin{pmatrix} V_{ud} & V_{us} & V_{ub} \\ V_{cd} & V_{cs} & V_{cb} \\ V_{td} & V_{ts} & V_{tb} \end{pmatrix} \begin{pmatrix} d \\ s \\ b \end{pmatrix}.$$

² $\bar{\nu} + e \rightarrow \bar{\nu} + e$ was the interaction observed at CERN in 1973.

The CKM Matrix has four independent parameters. It relates the first two generations, to a higher degree of accuracy, by,

$$\begin{pmatrix} d' \\ s' \end{pmatrix} = \begin{pmatrix} \cos \theta_c & \sin \theta_c \\ -\sin \theta_c & \cos \theta_c \end{pmatrix} \begin{pmatrix} d \\ s \end{pmatrix}$$

where $\theta_c = .22$ is known as Cabibbo angle; thus, the eigenstates-states of the charged current weak interaction, that change flavors, can be written as,

$$\begin{pmatrix} u \\ d' \end{pmatrix} = \begin{pmatrix} u \\ d \cos \theta_c + s \sin \theta_c \end{pmatrix} \quad \text{and} \quad \begin{pmatrix} c \\ s' \end{pmatrix} = \begin{pmatrix} c \\ s \cos \theta_c - d \sin \theta_c \end{pmatrix}$$

Cabibbo Suppression

In flavorodynamics³, u couples with d' and c couples with s' which in turn—as far as flavor eigenstates are concerned—means that both u and c couple either with d or with s . Since θ_c is small, $u - s$ and $c - d$ couplings are suppressed by a factor of $\tan^2 \theta$ compared to $u - d$ and $c - s$ couplings. This is known as Cabibbo suppression [4].

³The theory that addresses the weak interaction in Standard Model in particle physics is known as flavorodynamics.

GIM Cancellation

In the CKM Matrix, the $c - d$ coupling carries a vertex factor of $-\sin\theta_c$ while the $u - s$ coupling carries a vertex factor of $\sin\theta_c$, which is equal in magnitude but opposite in sign. If a particle can decay into the same final state through two decay amplitudes one of which carries a vertex factor of $-\sin\theta_c$ while the other one carries a vertex factor of $\sin\theta_c$, they can interfere destructively to suppress the decay. This phenomenon is known as GIM cancellation [5] after Glashow, Iliopoulos, and Maiani.

1.2 Weak Decay of Charm Quark

The charm quark emits a W^+ and turns in to an s' state producing a strange quark most of the time and a down quark otherwise. The W^+ decays either to a lepton and its anti-neutrino ($l\bar{\nu}_l$ pair) or to a quark and an anti-quark ($q\bar{q}'$ pair). The quarks thus produced along with the anti-quark in the original meson must form color singlet hadrons; thus, the strong interaction also plays an important role in the completion of the weak decay of the charm meson.

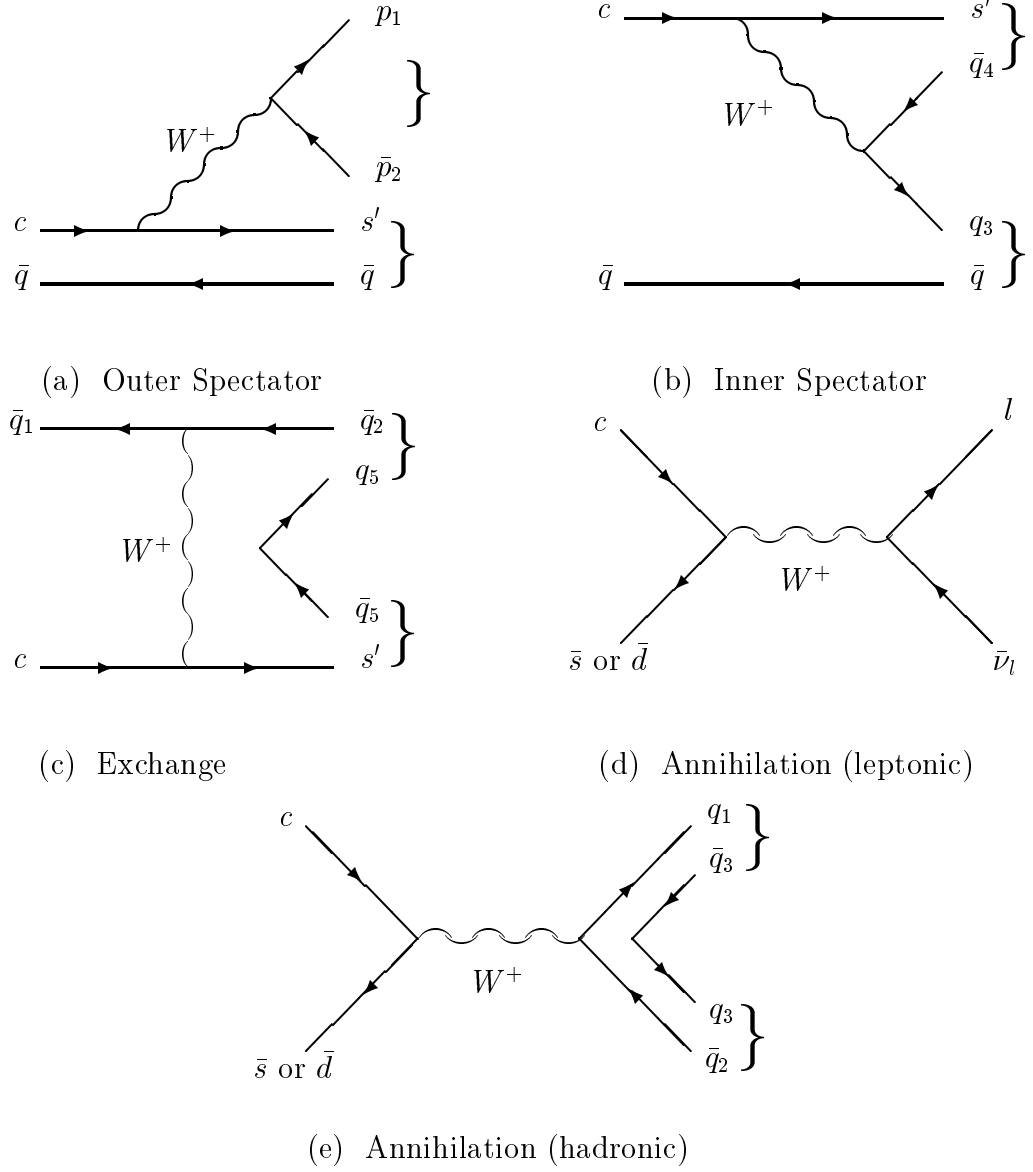
The charm quark can also annihilate with the anti-particle of the down quark or that of the strange quark producing a W^+ which then decays either in to an $l\bar{\nu}_l$ pair or in to a $q\bar{q}$ pair.

1.2.1 Tree Level Decay Models

At tree level, there are four Feynman diagram which contribute amplitudes to charm meson decay. Fig. 1.1 shows the three general decay models and the annihilation of the charm quark, in weak interaction, within a meson⁴. Figs. 1.1 (a) and (b) illustrates spectator decay modes. In this case, the charm quark decays into a W^+ and an s' and the original antiquark is a spectator without any interaction with the charm quark. In the outer spectator decay model (Fig. 1.1 (a)), the spectator antiquark coalesces with the produced s' to form a color singlet hadron, whereas in the inner spectator decay model (Fig. 1.1 (b)) the spectator coalesces with a decay product of the W^+ .

In exchange decays (Fig. 1.1(c)), the charm quark interacts with its accompanying antiquark by exchanging a W^+ with it. One or more $q\bar{q}$ pairs may pop out of the vacuum, and the final quarks then coalesce to give the hadronic final state. The charm quark can also annihilate with an \bar{s} or \bar{d} producing a W^+ . Figs. 1.1 (d) and (e) show the corresponding Feynman diagram for such decays. As with the exchange decay, the produced W^+ can decay either into a $l\bar{\nu}_l$ pair (Fig. 1.1 (d)) or $q\bar{q}'$ pair (Fig. 1.1 (e)). In the latter case, one or more $q\bar{q}$ pairs may pop out of the vacuum and coalesce with the produced quarks to form color singlet hadrons.

⁴Charm decay inside a meson has been considered as an example. The mechanism is basically the same for baryon-decay.



$$s' = s \cos\theta_c - d \sin\theta_c$$

Figure 1.1: Tree level Feynman diagrams for charm decay

Spectator decay amplitudes dominate the charm meson decay rate; unlike the other two mechanisms, they do not require the initial quark and anti-quark wave functions to overlap.

1.2.2 Hadronic, Semileptonic, and Leptonic Decays

In outer spectator and annihilation decay modes (Figs. 1.1 (a), (d), and (e)), the W^+ can decay either into an $l\bar{\nu}_l$ pair or into a $q\bar{q}'$ pair (particle p_1 and \bar{p}_2 in Fig. 1.1); thus, the final states can either be totally hadronic or totally leptonic or semileptonic (Table 1.4).

decay products of W^+	Decay Model	
	Outer Spectator	Annihilation
$u \ d'(d \cos\theta_c + s \sin\theta_c)$	Hadronic	Hadronic
$l \ \nu_l$	Semileptonic	Leptonic

Table 1.4: Hadronic, Semileptonic, and Leptonic Decays.

If the W^+ decays in to $q\bar{q}'$ pair, the decay products will all be hadrons; these are called hadronic decays. If the W^+ decays into an $l\bar{\nu}_l$ pair, depending on whether or not it is an outer spectator decay or an annihilation decay, the decay products will either be partly hadrons and partly leptons or all leptons. The decay is said to be

semileptonic when it comes from a spectator decay and it is said to be leptonic if it comes from an annihilation (Table 1.4).

1.2.3 Cabibbo Favored and Single and Doubly Suppressed Cabibbo Decays

The products of weak decay, at first place, are eigenstates of the weak interaction Hamiltonian, but the elementary particles we normally deal with are eigenstates of flavor. In the transition from the former to the latter, each vertex effectively picks up a factor of either $\cos \theta_c$ or $\sin \theta_c$; if the decaying particle is changing generations, the vertex factor is $\pm \sin \theta_c$, otherwise it is $\cos \theta_c$. A decay with a vertex that picks up a factor of $\sin \theta_c$ is suppressed by a factor of $\tan^2 \theta_c$ compared to a decay with vertices that pick up only factors of $\cos \theta_c$, because θ_c is small. This is called Cabibbo suppression. Decays are called Cabibbo-favored, singly Cabibbo-suppressed or doubly Cabibbo-suppressed decays depending on whether the decay has zero, one or two such vertices that pick up a factor of $\sin \theta_c$ (Fig. 1.2).

1.3 The Decay $D^0 \rightarrow K^- K^- K^+ \pi^+$

This thesis presents an analysis of the decay $D^0 \rightarrow K^- K^- K^+ \pi^+$. This is a Cabibbo favored charm decay which is suppressed by the phase space restrictions due to low Q value. In this analysis, the topologically similar decay $D^0 \rightarrow K^- \pi^- \pi^+ \pi^+$ has

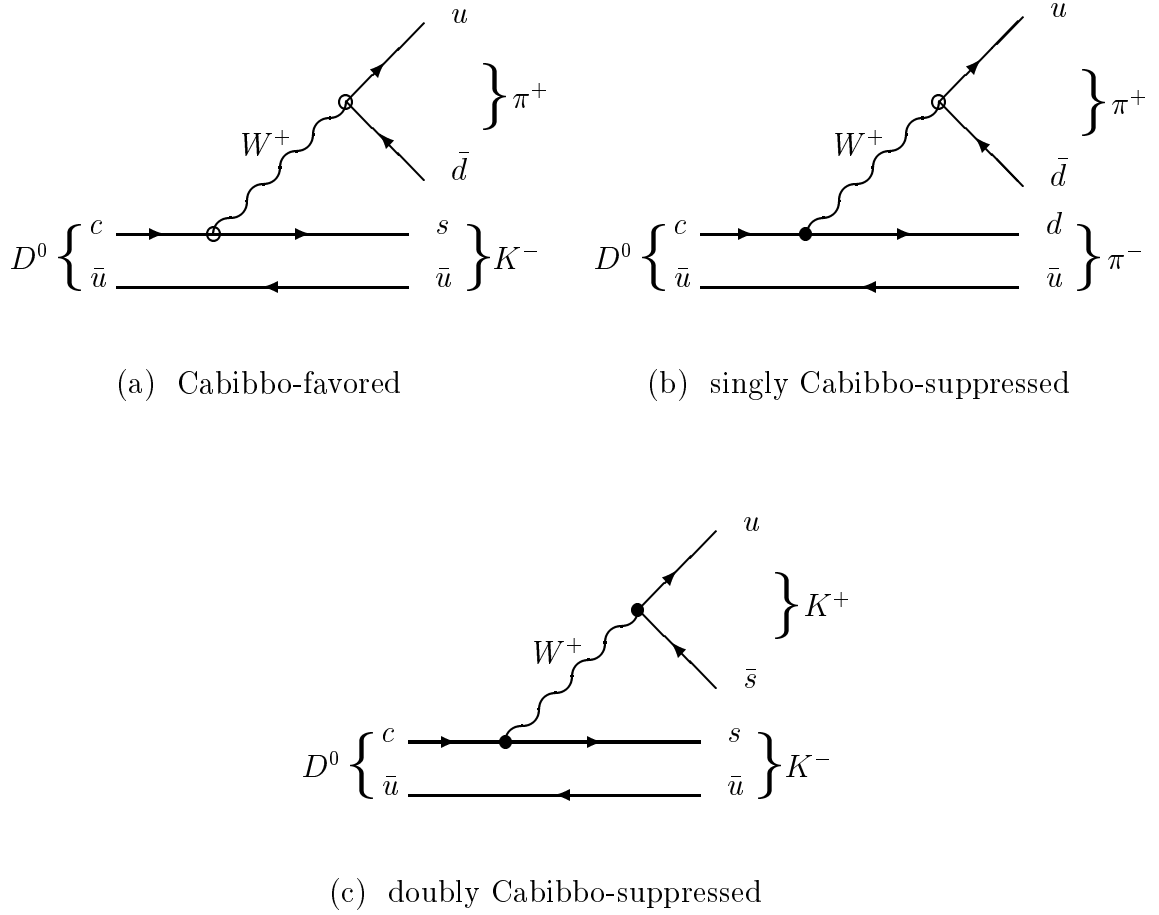


Figure 1.2: Examples of Cabibbo favored (a), singly Cabibbo suppressed (b), and doubly Cabibbo suppressed (c) decays. The vertices that are marked with circles denote those that pick up a vertex factor of $\cos\theta_c$ (Cabibbo-favored) whereas those that are marked with dots denote those that pick up a vertex factor of $\pm\sin\theta_c$ (Cabibbo-suppressed).

been used as the normalization channel. What is interesting about this analysis can be realized by comparing the Feynman diagrams that contribute to $D^0 \rightarrow K^- K^- K^+ \pi^+$ to those that contribute to $D^0 \rightarrow K^- \pi^- \pi^+ \pi^+$. The diagrams on the left of Fig. 1.3 show some of the Feynman diagrams that contribute to $D^0 \rightarrow K^- K^- K^+ \pi^+$ while those on right show the diagrams for $D^0 \rightarrow K^- \pi^- \pi^+ \pi^+$. One can obtain a Feynman diagram for the $KKK\pi$ decay by replacing a light quark pair ($u\bar{u}$ or $d\bar{d}$) in corresponding $K\pi\pi\pi$ diagram by an $s\bar{s}$ pair at the right place. The two top left diagrams and the two top right diagrams show example Feynman diagrams for non-resonant decays of $KKK\pi$ and $K\pi\pi\pi$ decays respectively. The bottom left diagram shows a Feynman diagram for the resonant decay to $KKK\pi$ ($D^0 \rightarrow \phi K^- \pi^+; \phi \rightarrow K^- K^+$) while the bottom right shows one for a resonant decay to $K\pi\pi\pi$ ($D^0 \rightarrow K^- \rho \pi^+; \rho \rightarrow \pi^- \pi^+$).

Previous Measurement

The branching ratio of $D^0 \rightarrow K^- K^- K^+ \pi^+$, with respect to that of $D^0 \rightarrow K^- \pi^- \pi^+ \pi^+$, has been measured before by the E687 experiment at Fermilab [7] and a value has been set at $0.0028 \pm 0.0007 \pm 0.0001$. The value set in this thesis has been obtained by doing a “blind” analysis (section 4.1).

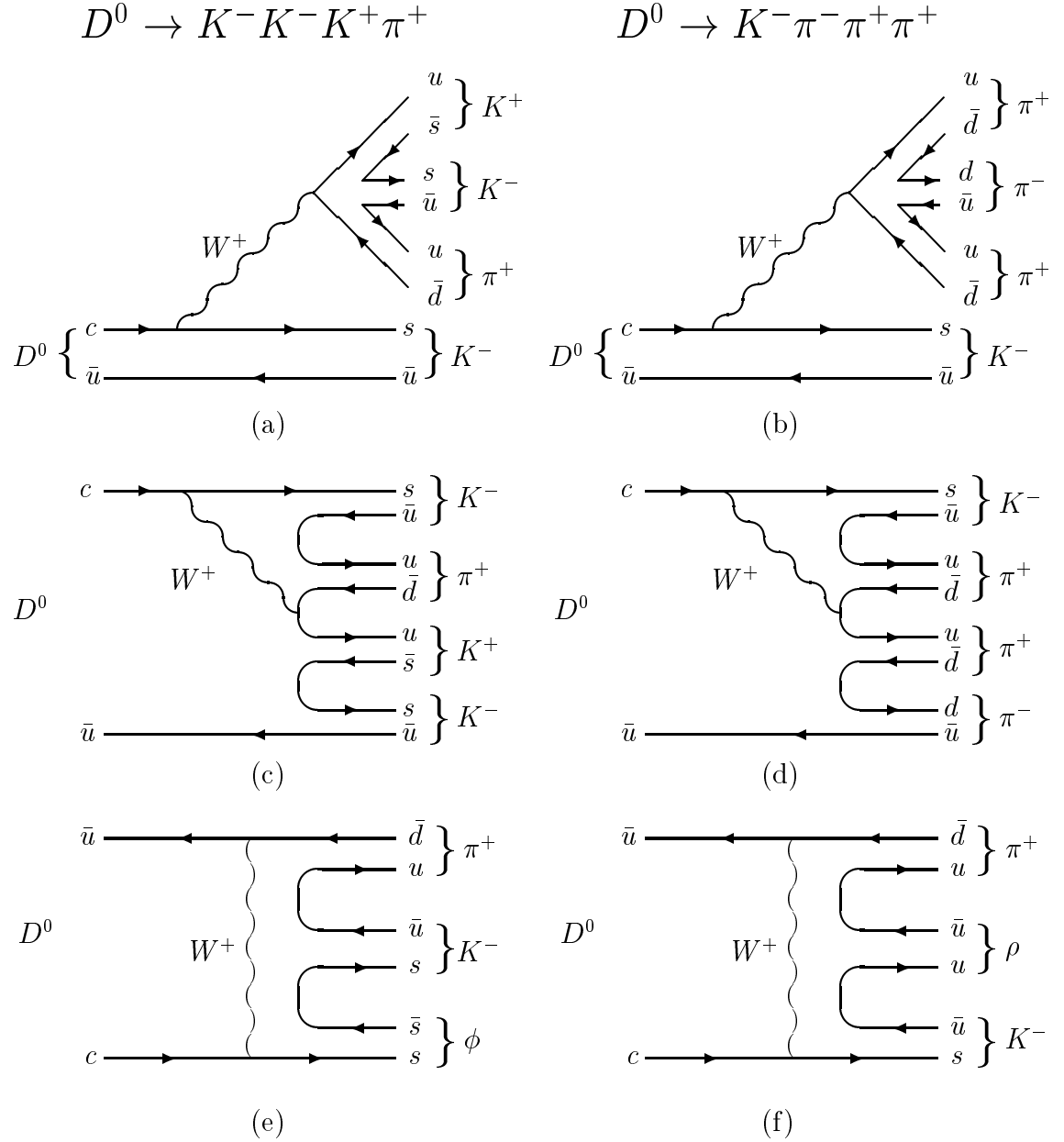


Figure 1.3: Some of the Feynman Diagrams that contribute to the decays $D^0 \rightarrow K^- K^- K^+ \pi^+$ and $D^0 \rightarrow K^- \pi^- \pi^+ \pi^+$. When the right light quark pair (either $d\bar{d}$ or $u\bar{u}$) in the latter is replaced by an $s\bar{s}$ pair, we get the former.

Chapter 2

The E791 Experiment

This is the fourth charm experiment that was performed at the Tagged Photon Laboratory **TPL** of the Fermi National Accelerator Laboratory **Fermilab, FNAL** at Batavia, Illinois. During the period: July 1991– January 1992, the experiment collected one of the world’s largest data samples with charm events. The data sample consisted of 40 TB worth of raw data with 20 billion events produced using a 500 GeV π^- beam incident on platinum and carbon targets.

2.1 History of TPL Spectrometer

The Tagged Photon Laboratory spectrometer was first designed and constructed in late 1970’s for the E516 experiment that was designed to study the photoproduction

of charm. In mid 1980's, it was used by the E691 experiment with improved tracking and vertexing, near the target region, especially with the addition of silicon microstrip detectors. The E769 experiment used the same spectrometer, in late 1980's, replacing the photon beam with hadron beams containing π , K , and p to study the hadroproduction of charm. The E791 experiment further improved the detector —among the other improvements— adding more silicon microstrip detectors for even better tracking and vertexing, enhancing the muon identification system, and adding a fast data acquisition system, and, in early 1990's, conducted the experiment collecting 20 billion events. Table 2.1 summarizes the beam(s) used and the numbers of charm decays reconstructed in these experiments.

experiment	Year	Beam	Reconstructed Charm
E516	1979	photon	150
E691	1985	photon	10,000
E769	1988	π , K , and p	4,000
E791	1992	π^-	200,000

Table 2.1: The numbers of charm events reconstructed at the Tagged Photon Laboratory at Fermilab.

2.2 Why Fixed Target

The goal of the E791 experiment was to collect and reconstruct a large number of charm decays while rejecting non-charm events. The collider experiments, which involve the annihilation of e^+ and e^- , are cleaner, but they have significantly lower cross section than fixed target experiments do. For this reason, fixed target experiments suggested themselves to be more suitable for experiments that hope to collect large data samples.

The other reason relates to reconstructing charm events. A charm particle that is in its ground state decays by weak interaction. The lifetime of such a decay is long compared to that of resonant decays that take place by strong interaction and long enough to be observed in the laboratory. Therefore, the faster the particle in the laboratory, the greater separated the secondary vertex is from its production vertex and the decay vertices of the strong decays that occur almost instantaneously. Given the average lifetime of the charm decay, a boost in a typical fixed target experiment is sufficient to separate the charm decay vertex by at least a few mm from its production vertex. In e^+e^- experiments at lower energy, such as CLEO or BaBar, the separation is typically a few hundred μm or less.

2.3 The E791 Coordinate System

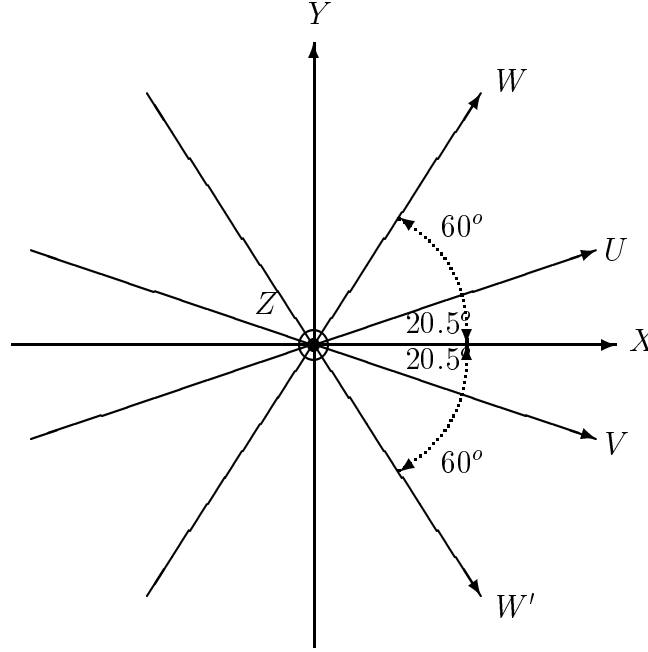


Figure 2.1: E791 Detector Coordinate System. The z direction is coming out of the paper and it nearly coincides with the beam direction. The z axis was directed towards the north; the x axis was directed toward the west and the y axis was pointing up.

Fig. 2.1 shows a schematic diagram of the E791 detector coordinate system. The Z direction extended from south to north and it very closely coincided with the direction of the beam and ran roughly through the centers of the detector elements. In Fig. 2.1, the Z axis is supposed to come out of the paper. The X direction extended from east to west while the Y direction extended from ground up. The three axes together formed a right handed system.

To reduce the ambiguity in pattern recognition, in addition to using track detectors which measured X and Y coordinates, some other detectors that measured stereo views in the U , V , W , and W' directions were also used. The U direction was defined to make an angle of 20.5° from positive X direction toward positive Y direction while V direction was defined to have the same angle from X direction, but toward negative Y direction. The W direction made an angle of 60° from X direction toward positive Y direction and W' made the same angle from positive X direction but toward negative Y direction (Fig. 2.1). The units of length were chosen to be cm.

When a wire in a proportional wire chamber (PWC) or a drift chamber (DC) is hit, which side of the wire the particle passed by is ambiguous. To help resolve such ambiguity, X' planes with the same direction as that of X , but displaced half the wire separation of the detector from the X were used.

2.4 The Beam

The charm-production cross section for pions is significantly higher than that for protons at the same energy because the gluons inside the pion are harder than those inside the proton; thus, a pion beam was preferred over a proton beam. The π beam was produced starting with a H^- beam. This hydrogen ion beam was accelerated to

750 KeV using a Cockroft-Walton generator and then a linear accelerator (LINAC) where it got further accelerated to 200 MeV. These H^- were then stripped of their electrons by passing through a carbon foil. The protons thus generated were then injected to the Booster, a 75 m diameter synchrotron, and accelerated to 8 GeV. These 8 GeV protons were then accelerated to 150 GeV in the Main Ring which was a synchrotron of 1 km radius. This proton beam was finally accelerated to 800 GeV in the Tevatron, which was a superconducting synchrotron that sat directly below the Main Ring in the same tunnel.

To generate the pion beam itself, the 800 GeV proton beam was directed to a 30 cm long beryllium primary target, and a 500 GeV negative pion beam was extracted using a system of collimators and magnets. The negative pion beam was preferred over the positive pion beam as the proton contamination was significantly higher in the latter. The negative pion beam, which had better than 98% purity, was then directed toward the TPL spectrometer using dipole and quadrupole magnets.

2.5 TPL Spectrometer

Fig. 2.2 shows a schematic diagram of the TPL Spectrometer. It had several detector components and electronics to measure the parameters associated with both beam and decay particle tracks. In addition to providing required computing

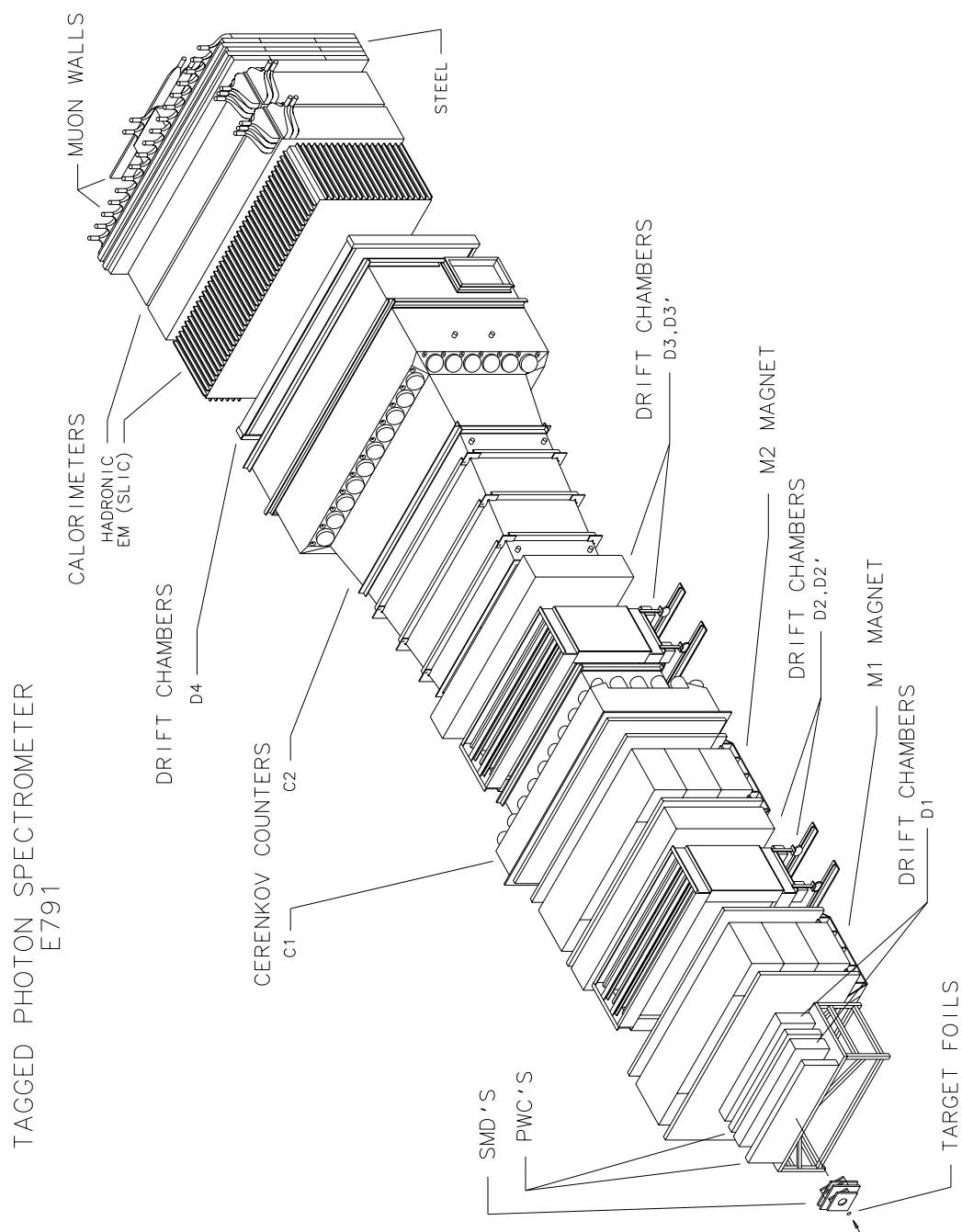


Figure 2.2: TPL Spectrometer

power for detection, electronics also played a significant role in triggering. The beam tracking system consisted of 8 Proportional Wire Chambers (PWCs) and 6 Silicon Microstrip Detectors (SMDs). The other major components of the spectrometer were the target, the interaction trigger, the downstream SMDs, the Drift Chambers (DCs), the downstream PWCs, the analysis magnets, the threshold Čerenkov counters, the electromagnetic calorimeter, the hadronic calorimeter, the muon wall and the data acquisition system. Fig. 2.3 shows a schematic diagram that illustrates what types of particles the tracking detectors (SMDs, PWCs and DCs), electromagnetic calorimeter, hadrometer, and muon wall detect.

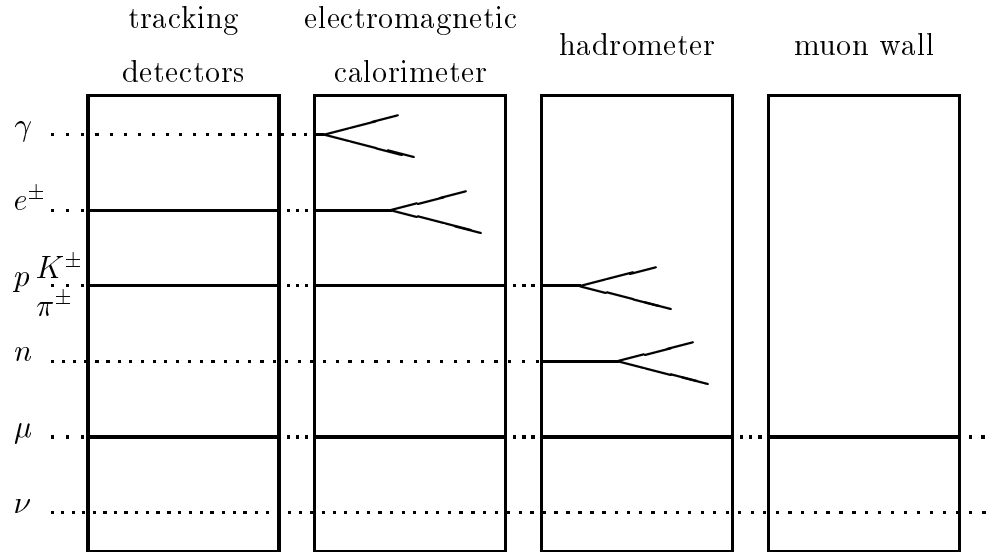


Figure 2.3: Types of particles each detector type detects. The dotted lines indicate passing through without being detected, the solid lines indicate detection without stopping, and the pronged lines indicate detection with stopping.

2.5.1 The Beam Tracking System

The beam tracking system consisted of eight PWCs and six SMDs; each type assembled in two groups: four PWCs in a PWC assembly and three SMDs in an SMD assembly. Table 2.2 and 2.3 list the characteristics of the PWC assemblies and SMD assemblies respectively. All four assemblies were located upstream of the target. The first and second assemblies of PWCs were located 31 m and 12 m upstream of the target respectively to provide good angular resolution of the beam. The SMDs were located closer to the target to provide good spatial resolution. The measurements thus made were used in the reconstruction of the primary vertex in the subsequent analyses.

	First PWC Assembly	Second PWC Assembly
Number of Planes	4	4
Dimensions (cm)	6×3	6×3
View Ordering	X, X', Y, W	X, X', Y, W
Wire Spacing (mm)	1.0	1.0
Resolution (μm)	145 (X, X'); 289 (Y, W')	145 (X, X'); 289 (Y, W')
Location in Z (cm)	-3117.0 to -3116.0	-1211.0 to -1209.0

Table 2.2: Characteristics of the Proportional Wire Chambers (PWCs) in the beam tracking system. The medium was a gas mixture of 82.7% Ar, 17% CO₂, and 0.3% freon.

	First SMD Assembly	Second SMD Assembly
Number of Planes	3	3
Dimensions (cm)	5×5	5×5
View Ordering	Y, X, W'	W', X, Y
Efficiency (%)	85, 85, 98	98, 98, 98
Strip Pitch (μm)	25	25
Resolution (μm)	7.2	7.2
Location in Z	-80.25 to -74.52	-33.163 to -29.483

Table 2.3: Characteristics of the Silicon Microstrip Detectors (SMDs) in the beam tracking system.

The PWC used a gas mixture of 82.7% Ar, 17% CO₂, and 0.3% freon. One reason for using this inorganic gas mixture was to prevent the cathode from being gradually coated with organic polymer compounds that are formed by the neutralization process of the organic ions, that would come from an organic mixture, on the cathode.

2.5.2 The Target

The E791 target consisted of five circular target foils: one platinum foil and four carbon (synthetic diamond) placed within plexiglass spacers. Table 2.4 gives the characteristics of the target foils. The charm production cross section increases linearly with the atomic number, A [8], while the inelastic cross section which produces most of the background only increases as $A^{0.71}$ [9]. These facts favor selecting material

Target Foil Number	1	2	3	4	5
Material	Platinum	Carbon	Carbon	Carbon	Carbon
Thickness (mm)	0.52	1.57	1.57	1.53	1.58
Diameter (cm)	1.606	1.369	1.377	1.368	1.355
Mass (g)	2.2396	0.7490	0.7507	0.7373	0.7300
Density (g/cc)	21.3	3.24	3.22	3.28	3.28
Radiation Lengths	0.169	0.012	0.012	0.012	0.012
Proton Interaction Lengths	0.00584	0.00590	0.00585	0.00582	0.00587
Position in Z (cm)	-8.191	-6.690	-5.154	-3.594	-2.060

Table 2.4: Characteristics of the E791 target. The number of π interaction lengths is about 2/3 of the number of proton interaction lengths.

with high A as target foils. Another advantage of high A material is the ability in attaining high interaction lengths in relatively short physical thickness. The short physical thickness of the target foil improves the precision of the primary vertex position determination. For these reasons, the first foil of the target was selected to be platinum which has relatively high A .

Nevertheless, high A also has disadvantages as materials that have high A also have high Z which leads to more multiple scattering which in turn decreases the precision of vertex and track measurements. The material with high Z also increases the probability of photons, that come from π^0 decays, convert into e^+e^- pairs. Thus, the other four target foils were carbon (synthetic diamond).

Given the energy scale of the experiment, a produced charm meson typically travels several mm before it decays. Therefore the spacing between target foils was chosen to be 15 mm so that most decays would take place in the air. This was important to minimize the background created by the secondary interactions of particles produced in the primary vertex.

2.5.3 Interaction Trigger Counter

The interaction trigger counter consisted of three scintillators. The beam counter and the veto counter were located in front of the target foils. The beam counter detected the beam and the veto counter vetoed the particles outside the target region. The interaction counter was located downstream of the target foils. This scintillator detected whether or not an interaction had occurred. The threshold was set at four minimum ionizing particles. Fig. 2.4 shows a layout of the target foils and the interaction trigger counter (not to scale).

2.5.4 Downstream SMD Planes

Given the lifetime of charm mesons and the energy scale of the experiment, a charm meson typically travels several mm in the lab frame before it decays; thus, a very good spatial resolution is needed for good vertexing. This goal was achieved by employing 17 SMD planes right after the target foils. Table 2.5 describes the

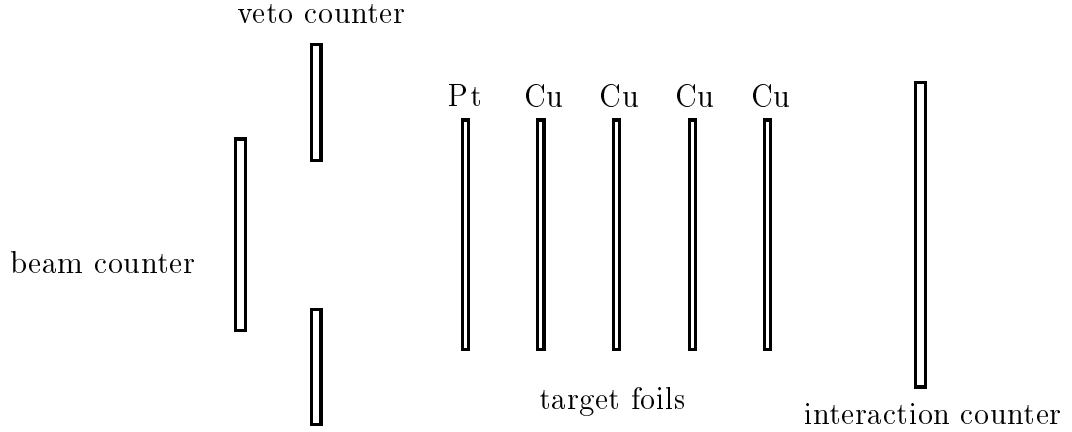


Figure 2.4: E791 target and interaction trigger counter region (not to scale)

characteristics of these downstream SMD planes. The overall geometrical acceptance of the downstream SMDs was about ± 150 milliradians around the beam axis. The strip pitch of the SMDs ranged from $25 \mu\text{m}$ to $200 \mu\text{m}$. Some planes had a different strip pitch for their inner strips than for their outer strips. Planes closer to the target had smaller the strip pitch to maintain good spatial resolution; thus, the inner strip pitch of the SMD planes that were closest to the target had an inner strip pitch as small as $25 \mu\text{m}$ while the outer strip pitch of the SMD planes located farther to the target was as large as $200 \mu\text{m}$. The efficiency of the SMDs ranged from 83% to 99%. The transverse resolution of the SMD system was typically about $15 \mu\text{m}$ when the tracks were projected back to the origin. Since there are multiple hits on the detectors, the V view was used in addition to the X and Y views to resolve ambiguities in pattern recognition.

SMD Plane	Z Position (cm)	Strip Pitch (μm)	Efficiency (%)	View
1	0.670	25, 50	83	<i>Y</i>
2	1.000	25, 50	85	<i>X</i>
3	1.931	25, 50	93	<i>X</i>
4	3.015	50, 50	95	<i>Y</i>
5	6.684	50, 50	96	<i>V</i>
6	11.046	50, 50	98	<i>Y</i>
7	11.342	50, 50	97	<i>X</i>
8	14.956	50, 50	94	<i>V</i>
9	19.915	50, 50	90	<i>X</i>
10	20.254	50, 50	88	<i>Y</i>
11	23.878	50, 50	93	<i>V</i>
12	27.558	50, 200	98	<i>V</i>
13	31.848	50, 200	96	<i>X</i>
14	34.548	50, 200	98	<i>Y</i>
15	37.248	50, 200	99	<i>X</i>
16	39.948	50, 200	99	<i>Y</i>
17	45.508	50, 200	99	<i>V</i>

Table 2.5: Characteristics of the downstream SMD planes. The pitch of inner strips of some of the SMD planes were different from that of outer strips. The two numbers in the third column gives the inner and outer strip pitch values.

2.5.5 Downstream PWC Planes

Two downstream PWCs were also used in the TPL spectrometer to measure the y position of the tracks. One PWC was located at 120.4 cm in z and the other was at 162.94 cm in z . They both had a wire spacing of 2.0 cm and the resolution of these two planes were measured to be $750\ \mu\text{m}$. The medium for these PWCs was also chosen to be a gas mixture of 82.7% Ar, 17% CO₂, and 0.3% freon.

2.5.6 Drift Chambers

The thirty five Drift Chambers (DCs) were the main detector elements, downstream of the SMDs, in particle track detection. These thirty five DCs were arranged in four modules: D1, D2, D3, and D4. Each module consisted on one or more assemblies each of which in turn consisted of three or four planes assembled in X , X' , U , and V . Table 2.6 gives the characteristics of each DC module.

The first module, D1, was located upstream of the first analysis magnets M1 and along with downstream SMDs and PWCs. This provided the initial measurements of the particle trajectories. The modules D2, D3, and D4 were located between the two magnets, M1 and M2, just after M2 and far downstream before the calorimeter respectively. The relatively poor resolution of D4 can be attributed not only to its

	D1	D2	D3	D4
Approximate Dimensions (cm)	130×75	280×140	320×140	500×250
U and V Cell Size (cm)	0.446	0.892	1.487	2.974
X Cell Size (cm)	0.476	0.953	1.588	3.175
Number of Assemblies	2	4	4	1
Total Number of Planes	8	12	12	3
View Ordering	X, X', U, V	U, X, V	U, X, V	U, X, V
Z Position of First Plane (cm)	142.5	381.4	928.1	1738.0
Z Position of Last Plane (cm)	183.7	500.8	1047.1	1749.2
Approximate Resolution (μm)	430	320	260	500
Approximate efficiency	92%	93%	93%	90%

Table 2.6: Characteristics of the Drift Chamber Assemblies. The medium was a gas mixture of $\sim 90\%$ Ar, $\sim 10\%$ CO₂, and $\sim 1\%$ freon.

relatively large cell size, but also to the high noise level due to the backscattering off the calorimeter.

As in PWCs, the medium was again chosen to be a gas mixture of Ar, CO₂, and freon, but the fraction of each component was a little bit different from that in PWC. The fractions for DC were $\sim 90\%$ Ar, $\sim 10\%$, CO₂, and $\sim 1\%$ freon.

2.5.7 Analysis Magnets (M1 and M2)

TPL spectrometer had two large-aperture copper coil magnets for measuring momenta of the particles. The major component of the magnetic fields were an-

tiparallel to the direction of Y and hence they bent the particles very nearly in the horizontal plane. The centers of the two magnets were 2.8 m and 6.2 m downstream of the targets. The magnetic field of these magnets was measured using zip track [10]. The maximum field strength B_y of the first magnet M1 was 5 kG and that of M2 was 7 kG. The average total integrated magnetic field strength, $\int \vec{\mathbf{B}} \times d\vec{\mathbf{z}}$, was about 17.5 kG m. The approximate P_T kick of the two magnets, M1 and M2, were 212 MeV and 324 MeV respectively. Table 2.7 gives the characteristics of the magnets M1 and M2.

	M1	M2
z Position of the Front (cm)	222.5	566.9
z Position of the Center (cm)	273.5	617.7
z Position of the Back (cm)	324.1	668.5
Aperture (cm ²)	183.2×81	182.9×85.6
Length (cm)	101.6	101.6
Current (A)	2500	1800
Maximum B_y (kG)	5	7
P_T kick (MeV)	212	320

Table 2.7: Characteristics of the analysis magnets. The average total field strength ($\int \vec{\mathbf{B}} \times d\vec{\mathbf{z}}$) was about 17.5 kG m.

2.5.8 Čerenkov Counters

The TPL Spectrometer used two threshold Čerenkov counters, C1 and C2, for particle identification. Table 2.8 give the characteristics of the Čerenkov counters. The first counter, C1, was filled with 100% N₂ and was positioned partially inside of M1 and the second counter, C2, was filled with 80% He and 20% N₂ and was positioned after M2. Both counters were maintained at atmospheric pressure. As the gas mixture of one counter was different from that of the other, they had different refractive indices and hence different threshold momenta for emitting Čerenkov light for each particle type. The Čerenkov light, generated by the particles that traveled with a momentum above the threshold momentum, was detected by the Photo-Multiplier Tubes (PMTs) directed at the reflective mirrors. The photo-electron signal thus generated by PMTs were then digitized and used along with the tracking information to identify¹ the particle. Reference [11] gives a detailed description of the Čerenkov counters of the TPL spectrometer.

2.5.9 Calorimeters

There were two calorimeters in the TPL spectrometer. The segmented liquid ionization calorimeter (SLIC) [12] was employed to measure the energy of electrons

¹Particle identification with Čerenkov light actually sets a probability rather than identifying the particle beyond doubt.

	C1	C2
Length (m)	3.7	6.6
Number of Mirrors	28	32
Gas Mixture	100% N ₂	80% He, 20% N ₂
$\delta = (n - 1)$	290×10^{-6}	86×10^{-6}
π Threshold Momentum (GeV)	5.8	10.6
K Threshold Momentum (GeV)	20.5	37.6
p Threshold Momentum (GeV)	38.9	71.5

Table 2.8: Characteristics of the Čerenkov counters.

and photons; the hadrometer [13] was used to measure the energy of the hadrons. Both calorimeters were employed as part of the E791 trigger to select the events with transverse energy greater than 4.5 GeV. Different particle types have different energy deposition patterns in the calorimeters; therefore, the calorimeters were also used, along with the Čerenkov detectors, in particle identification.

The SLIC consisted of 60 liquid scintillator layers that were each half-inch thick. Each of the three views U, V, and Y had 20 layers. Each layer was divided into channels by a thick aluminum sheet bent into square wave corrugation. The aluminum surface was coated with teflon to accommodate internal reflection of scintillating light. Lead sheets were placed between the scintillator channels to generate electromagnetic showers. The photo-multipliers attached to the channels captured the scintillation light for further processing. Table 2.9 shows the characteristics of the SLIC.

	U view	V view	Y view
number of channels	109	109	116
number of layers	20	20	20
channel width (cm)	3.17, 6.35	3.17, 6.35	3.17, 6.36
channel length (cm)	260	260	244
view ordering	U, V, Y		
upstream z position (cm)	1866		
downstream z position (cm)	1962		
active area (cm ²)	488 × 244		
total radiation length	21.5		
total interaction length	2.07		
energy resolution	$(\frac{\delta E}{E})^2 \approx (\frac{17.4\%}{E})^2 + (11.5\%)^2$		
position resolution (cm)	0.65		

Table 2.9: Characteristics of the SLIC

The hadron calorimeter (hadrometer) was designed to detect both hadrons and muons. It sat just behind the SLIC. The hadrometer consisted of 72 layers —36 layers in either of the views X and Y— of one inch thick steel interleaved with 3/8 inch thick plastic scintillator. The layers were divided into 14.5 cm wide channels. The X view channels spanned the full height of the detector. The Y view channels were divided in the middle. The hadrometer was divided into two modules: front and back. The comparison between the energy deposited in the front and back modules provided some information that helped separate muon and hadrons. Table 2.10 show the characteristics of the hadrometer.

	X view	Y view
number of channels	66	76
number of layers	36	36
channel width (cm)	14.5	14.5
view ordering	X, Y	
absorber thickness	2.54	
total interaction length (cm)	6	
upstream z position (cm)	1973	
downstream z position (cm)	2131	
active area (cm ²)	490 × 270	
energy resolution	$\frac{\delta E}{E} \approx \frac{75\%}{\sqrt{E}}$	

Table 2.10: Characteristics of the hadron calorimeter

2.5.10 Muon Wall

The muon wall was the last detector in the TPL spectrometer. It was a 10 foot tall 18 foot wide wall that consisted of layers of plastic scintillator strips in X and Y views. A 106 cm thick block of steel was placed in between the hadrometer and the muon wall to stop the hadrons that made it through the calorimeters without interaction; thus, only muons with energies greater than 4 GeV could make it through the steel block to the muon wall. The wall in X view, which was 3 m tall, consisted of 12 vertical paddles; the center paddle was 61 cm wide and each of the rest was

40.6 cm wide. The center paddle consisted of three parts; the middle paddle was 60 cm high and the two paddles above and below it were each 120 cm high. The Y view wall had 16 paddles; each 3 m long and 14 cm wide.

2.6 Trigger and Data Acquisition

The identification of true charm events in real time was an extremely challenging task with the available computing resources. Therefore, the goal was to collect as big a data sample as possible with loose trigger selection criteria. The detailed analyses were carried out off-line when the computing efficiency was less of an issue.

The E791 trigger had two levels of decision-making processes. The pretrigger was based on the quality of the beam and the secondary trigger was based on the transverse energy deposited in the calorimeters. The former took about 160 ns while the latter took about 470 ns. Section 2.5.3 describes the interaction counters used in the pretrigger and selecting the events that had at least four charged daughter tracks. The calorimeter trigger was based on the fact that decay products of relatively more massive charm particles are produced with higher transverse energy than those of parent particles with lighter quarks. The energies of the daughter tracks were scaled by $\sin\theta$, where θ is the angle between the beam direction and the line joining the

target and the element of the calorimeter that recorded a hit, and added up. This was called the transverse energy, E_T , of the event and was required to be at least 4.2 GeV. The events with total energy higher than 700 GeV were also rejected to get rid of events with multiple beam particle interactions.

Beam particles interacted with the target about once every 25 μ s. Approximately half of these interactions passed the trigger requirements. The digitization took about 50 μ s; therefore, there was about 50% dead time. The events were accepted at a rate of 9000 per second. Eight large first-in first-out (FIFO) buffers were used to store event segments, which were then compressed and formatted to a typical length of 2.5 kb. These were written to 8 mm tapes using 54 ACP 1 processors and 42 Exabyte tape drives. A 640 Mb memory buffer allowed writing data during the interspill. The DAQ collected and recorded data at a rate of 207K events per second per spill averaging 9.6 Mb/s [14].

Chapter 3

Event Reconstruction and Selection

The original E791 data sample consisted of 20 billion events on about 24,000, 2.2 GB, 8mm tapes, a total of 40-50 TB of data. The first stage of the analysis was to reconstruct and filter data so the charm content of the reduced data sample was enhanced. The process involved reconstructing the tracks, finding primary and secondary vertex candidates, calorimeter and Čerenkov reconstruction, and muon identification. The events were first partially reconstructed. The partially reconstructed events were then filtered (section 3.4.2). The events that survived the filter were then fully reconstructed for further analysis. This step was common to all the analysis

institution	number of events reconstructed (billions)
Centro Brasileiro de Pesquisas Fisicas	1.8
Fermilab	4.7
Ohio/Kansas State University	6.2
University of Mississippi	6.4

Table 3.1: Number of events reconstructed at different computer farms.

done with the E791 data sample and demanded an enormous computer power. The process was carried out at four computer farms [15] (Table 3.1) and took about 10,000 MIPS years over a period of two and half years.

The second stage of a data analysis is selecting the subset of data that is more closely related to the analysis in question. The subsequent steps of the selection stage are known as stripping, substripping, microstripping and so on as it progresses. As the data selection in this stage was done with the focus on a particular analysis, the selection criteria for this stage differed from one analysis to the other.

3.1 Track Reconstruction

The E791 tracking algorithm first reconstructed the beam track upstream of the target and then reconstructed charged daughter tracks downstream of the target. To reconstruct the beam track, the hits in SMDs (along with those in PWCs) upstream

of the target were used. The tracking algorithm started with finding straight line segments in each view: X, Y, and V using a minimum χ^2 fit. Each of the X and Y views were required to have at least four hits while the V view was required to have at least three hits in a line segment. One dimensional tracks from the three views were combined to form three dimensional straight line tracks. The best track was determined by its χ^2 and the number of hits and kept. The beam track reconstruction efficiency was about 95%.

The beam track reconstruction was followed by the reconstruction of the charged tracks from the hits in the 17 downstream SMDs. The tracks were first reconstructed in each view X, Y, and V, using the hits in the SMDs; then these single-view tracks were used to reconstruct the three-view tracks. The tracks thus formed were ordered by their quality, determined by the χ^2 , the number of hits, and the number of unique hits of the track. Starting with the track with the best quality, these tracks were projected into the DC system to find continuations through the spectrometer.

The DC reconstruction algorithm started by constructing what E791 called "triplets". A group of three closely lying DC chambers in X, Y, and V view can be thought of roughly sharing the same plane in Z. A triplet is the space point where the three X, Y, and V wires that record hits seem to intersect. The main component of

the magnetic field was in the Y direction; therefore, the charged particles traversed through the spectrometer with minimal bend in the Y direction. The tracks reconstructed in downstream SMDs were therefore projected in the Y view into the DCs and triplets were searched for within a band of $\pm 2.5\text{cm}$ that allowed for multiple scattering. For each matching triplet, a $\sim 4\text{mm}$ wide “road” was created in other views using the SMD information and single bend point approximation¹. The actual size of the road depended on the momentum of the track. Once the road was defined, the tracking algorithm searched for additional triplets in D3. If at least eight hits were found in D3 then the search for additional hits in the road was continued in D2. If at least eight hits were found in D2 the search was extended to D1 and D4 for more hits. χ^2 minimizations were carried out on the track candidates to determine slopes, intercepts and momenta. Tracks with $\chi^2/\nu < 5$ were kept. Track segments, triplets, and hits used by the good tracks were then marked as unavailable for further tracking usage. The remaining SMD tracks were projected to D2 to look for the tracks that did not make it through the second magnet.

¹In the single bend point approximation, the transverse momentum kick of the magnet is assumed to be concentrated at the center of the magnet. The charged particles traversing through the magnet bends only once at the center of the magnet.

3.1.1 ESTR and SESTR Tracks

Due to SMD inefficiencies, not all real tracks that passed through the SMD system recorded hits. Also, a majority of K_S^0 's and Λ 's decayed downstream of the SMD system. Such tracks were reconstructed starting with the hits in the D3 assembly without reference to SMD hits. The process of track reconstruction of these tracks were otherwise similar to the process that involved SMD hits (section 3.1). These tracks —with only DC hits— are known as ESTR (Exhaustive Search Track Reconstruction) tracks. The tracks that had both DC and SMD hits are known as SESTR (SMD + ESTR) tracks.

3.1.2 Track Category

To identify tracks with hits in different DC groups, a category number was assigned to each track depending on which drift chamber groups the track has made hits in. Had it made hits only in SMDs, then the category would have then been assigned 0. If it had made hits in drift chambers in addition to in SMDs, then the category would be assigned $D_4D_3D_2D_1$, where D_i stands for the Drift Chamber groups and assigned 1 if there is a hit or 0 otherwise. The number $D_4D_3D_2D_1$ is then interpreted in binary and converted into decimal. For example, if the track had made hits in drift chamber groups D_1 and D_2 , in addition to the hits in SMDs, but neither in D_3 nor in D_4 , then $D_4D_3D_2D_1 = 0011$. This number is decimal 3.

DC groups that record hits	$D_4D_3D_2D_1$	category
only SMD hits	0000	0
D1 and SMD hits	0001	1
D2 and D1 (SMD hits possible)	0011	3
D3 and D2	0110	6
D3, D2, and D1 (SMD hits possible)	0111	7
D4, D3, and D2	1110	14
D4, D3, D2, and D1 (SMD hits possible)	1111	15

Table 3.2: Common category values of the tracks that have hits in adjacent DCs. Category 3, 7, and 15 tracks can have hits also in SMDs.

Table 3.2 shows the category assigned to the tracks that have hits in different DCs. Category 3, 7, and 15 tracks can have hits also in SMDs. About a third of the tracks that were labeled as category 3 by the tracking algorithm were found to be ghost² tracks. Later on, an algorithm using a neural net was used to discard most of the ghost tracks from the category 3 track sample.

3.2 Topological Vertex Reconstruction

Vertex reconstruction was carried out, after the track reconstruction, using SESTR tracks. It started with reconstructing the primary vertex. The interactions were supposed to take place only within the target foils; thus the primary vertices were loosely constrained to sit inside the target foils. The algorithm started with

²A ghost track is a false track the tracking algorithm constructs.

looking for the presence of the beam track and an intersection of two SESTR tracks within the target foils. Having found such a candidate, the algorithm continued to add more tracks—if possible—to form a vertex with a good χ^2/ν . The events that did not record a beam track were also vertexed using SESTR tracks, requiring them to intersect—if they did—within the target foils. The reconstruction efficiency for the primary target was about 95%. If a good primary vertex was found, tracks which were not used in the primary vertex were used to find secondary vertex candidates. The secondary vertices were also found by constructing two pronged vertex candidates and adding more tracks if possible. All the independent secondary vertices with acceptable χ^2 were formed, and some sharing of tracks among different secondary vertices was allowed. The algorithm was optimized to reconstruct candidate events with charm decays.

3.3 Particle Identification

From the knowledge of the production rates of electrons, muons, pions, kaons, and protons in the experiments similar to E791 experiments, the *a priori* probabilities for a track to be an electron, a muon, a pion, a kaon, or a proton were estimated. Table 3.3 lists these estimated *a priori* probabilities. At reconstruction, these *a priori* probabilities were changed to reflect particle identification information from the Čerenkov counters, calorimeters, and muon wall. The Čerenkov information was extracted by

particle type	<i>a priori</i> probability
electron	0.02
muon	0.01
pion	0.81
kaon	0.12
proton	0.04

Table 3.3: Estimated *a priori* probabilities for electrons, muons, pions, kaons, and protons.

comparing how much light was collected in each unit to how much each particle type should have generated at the given momentum. The calorimeter information came from the fact that different particle types had different energy deposition patterns in the calorimeter [12] [13]. If no detector information was available for a particular track, then the *a priori* probabilities were left assigned to that track.

3.4 Event Selection

The 20 billion event data sample in E791 was too big for direct use in a typical physics analysis; thus, a reduction of the data sample was necessary before one could carry out real physics analyses. The data reduction was carried out in several steps: filtering, stripping, substripping, microstripping, and so on. Each step involved understanding the behavior of the interesting events (signal events) and background events with the variation of different event parameters that discriminated signal from background.

3.4.1 Event Parameters

The data reduction was carried out in such way that it reduced the background content and enhanced the signal fraction of the data sample. A set of parameters that discriminates signal from background was associated with each event. The selection criteria were chosen by optimizing the point at which a cut³ on a parameter was defined. This section describes the event parameters used in this analysis in optimizing the final event selection criteria.

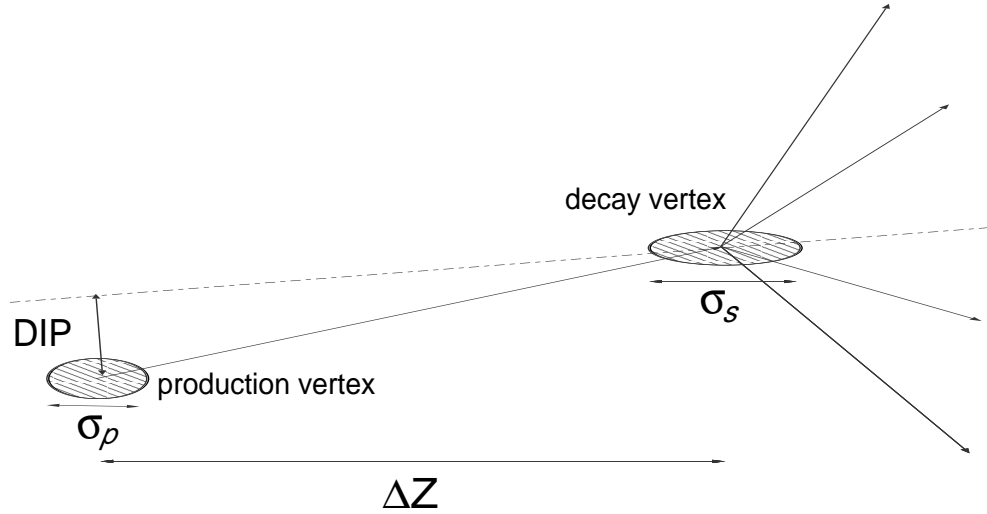


Figure 3.1: The geometry of a decay. The production (primary) vertex and a decay (secondary) vertex have been shown.

³“cut on a parameter at x” is equivalent to saying “accept only the events with the value of that parameter above—or below depending on the parameter—x”.

CHIS (χ^2/DOF of the Secondary Vertex): In principle, the decay products should point back to the secondary vertex, but in practice they do not; therefore, in vertex reconstruction, a potential secondary vertex is selected and the vertex point is assigned in such a way that the χ^2/DOF is minimal. This minimal χ^2 of the secondary vertex is named CHIS. The lower CHIS, the more likely that the decay vertex is real.

CHIP (χ^2/DOF of the Primary Vertex): This is the same as above, but calculated for the primary vertex.

DIP (Distance of Impact Parameter): Again in principle, the sum of momenta of the decay products of a charm particle should point back to the primary vertex, but in practice it does not point back perfectly. DIP is the distance of closest approach between the projection of the total momentum of the decay products and the production vertex (Fig. 3.1). Again, the lower the DIP, the more likely that the decay vertex is real.

SDZ (Scaled Δz): This gives the separation between production and decay vertices, in terms of its standard deviation (Fig. 3.1). Mathematically this reads,

$$SDZ = \Delta z / (\sigma_p^2 + \sigma_s^2)^{1/2}$$

The lifetime of the charm decay is long enough to produce large SDZ (well above 10) values. The large SDZ will therefore discriminate signal events from background.

CVK (Čerenkov Probability of K), PCVK, and CVP: CVK is the Čerenkov probability that the track is a K ⁴. PCVK is the product of three CVKs of the $KKK\pi$ candidate. Getting rid of events with lower CVK increase the likelihood of the event being signal (section 3.3). CVP stands for the Čerenkov probability that the track is a π .

PTBL (p_T Balance) : This is the transverse component of the reconstructed D momentum with respect to the line of flight. This has a correlation with DIP but depends differently on SDZ. As with DIP, events with low PTBL are more likely to be signal.

SDCA (Scaled Distance of Closest Approach): This is the minimum of the separations of decay tracks from the primary vertex, in terms of their errors. Large SDCA assures that primary tracks are not misidentified as decay tracks.

SDZT (Scaled Δz w.r.t. the Target): The method of calculation of SDZT is the same as SDZ, but it is calculated for the absolute distance between the

⁴The same principle applies also to e , μ , p and π , but the Čerenkov identification of those particles, except π , is irrelevant for this analysis.

secondary vertex and the closer surface of the target foil closest to the secondary vertex. Mathematically this reads,

$$SDZT = \frac{(|z_{sec} - z_{targ}| - t_{targ}/2)}{\sigma_s}$$

where z_{sec} and z_{targ} are the z position of the secondary vertex and the center of the closest target foil respectively and t_{targ} is the thickness of that target foil. A cut on SDZT at the appropriate point ensures that the secondary vertex sits outside of the target foils.

SEED: This gives the number of daughter tracks found in the decay vertex by topological vertex reconstruction algorithm (section 3.2). In this particular analysis, in which we are looking at a four body decay, an event is labeled as SEED4 if all four tracks were found in a 4-prong vertex in the vertex list. If three tracks were found in a common vertex in the vertex list, a match from the remaining tracks, to form a four prong vertex is attempted and a refit is made. If that combination passed the substrip cuts, that event is labeled as SEED3 and stored for further analysis.

CAT, MCAT and NCAT3: CAT is the parameter name for the category of the track. A value to this parameter is assigned depending on which drift chamber groups the track has made hits in. Section 3.1.2 describes the track categories

in detail. MCAT is the minimum of the categories of the daughter tracks and NCAT3 is the number of category 3 daughter tracks present in the decay.

TAU: This is the proper life time of the reconstructed D.

PTSQ: PTSQ is defined as the summation of transverse momenta of the daughter tracks with respect to the direction of momentum of the constructed D. The signal events have a well defined range of PTSQ and the background events spread well beyond that range at both ends. This discrepancy in the distributions helps eliminate some of the background events. The fraction of background events that has higher PTSQ is relatively prominent in SEED4 compared to SEED3.

SPTSQ: This is PTSQ scaled by the maximum possible PTSQ for that particular event given the daughter masses and the candidate D^0 reconstructed mass.

ISOL: This is the transverse separation of the tracks that are not labeled as daughters from the secondary vertex. This gives a measure of how well other tracks geometrically isolate from the decay in question.

RAT, MRAT and PRAT: RAT of a daughter track is defined as the ratio of its transverse separation from the secondary vertex to that from the primary. The lower RAT, the higher the chance of that track coming from the secondary

vertex rather than from the primary. MRAT and PRAT are the maximum and product of the four RATs of the decay candidate.

DELZ (Δz): This is the separation between the primary and the secondary vertices in z .

COSSP: The sphericity axis of the daughters is found in the center of momentum (CM) frame (Appendix A). The sphericity angle in this memo is the angle between the sphericity axis and the D^0 momentum calculated in the center of momentum frame. COSSP is the absolute value of the cosine of the sphericity angle. This variable correlates with PTSQ. We found more signal events at lower COSSP and an accumulation of background events at higher COSSP.

FOM (Figure of Merit): FOM (Figure of Merit, Section 4.5) is a variable that is constructed from a set of variables that are not correlated. This is a measure of the Signal/Background ratio in the region of parameter space. It is constructed so that a single cut on FOM addresses all the variables it uses and selects regions of the multidimensional variable space of the selected variables that has higher FOM than the cut, rejecting the rest of the space that has lower FOM. A high end selective cut on FOM increases the likelihood of the selected candidates being signal.

3.4.2 Filtering

Filtering was the first stage of the event selection process and it was done as the events were reconstructed. An event with a primary vertex was accepted by the filtering algorithm if it also had:

- a secondary vertex with good separation from the primary vertex,
- a K_S or a Λ from ESTR tracks,
- or a ϕ from SESTR tracks.

A sufficient vertex separation was ensured by requiring $SDZ > 6$ for two prong vertices and $SDZ > 4$ for vertices with three prongs or more. The presence of K_S , Λ , and ϕ was detected by reconstructing $\pi^+\pi^-$, $p\pi^+$, and K^+K^- mass respectively and requiring that the reconstructed mass was close to the mass of the parent that was being selected. The filtered events were written out, with both raw data and all reconstructed physical parameters, to tapes which E791 called Data Summary Tapes (DSTs). The original data sample that was on 24,000 tapes was stored on 7500 tapes after filtering.

3.4.3 Stripping

After reconstruction and filtering, the data sample was further pushed through another stage of selection process which E791 called stripping. The stripped data were written to two output streams: stream A and stream B. The two streams had different tags⁵ [16]. After stripping, the data samples in each stream could be fit in 2000 DSTs. The analysis described in this thesis used the data from stream A output.

3.4.4 Substripping

The stripped data sample was still too big for physics analysis. The next stage of selection, namely substripping, preferentially selected the events for specific types of physics analyses. The substripping stage wrote events through three output streams: stream A, stream B, and stream C. Each stream wrote out data onto about 330 DSTs. The substrip stream C, which E791 called Kitchen Sink Substrip [17], kept both $KKK\pi$ and $K\pi\pi\pi$ candidates and was selected for the analysis described in this thesis.

⁵The algorithm looked into each event to see if it passed a certain criterion. Each such test involved a set of cuts. Once the event was found to pass the criterion, it was marked to be written to the output. This was known as tagging.

3.4.5 Microstripping

In this stage, the substripped data was fairly tightly constrained to contain only $KKK\pi$ and $K\pi\pi\pi$ (normalization channel) candidates. A vertex driven search was carried out by requiring the event to have at least two vertices before it was analyzed any further. The algorithm first looked at four prong vertices found by the E791 vertex algorithm. If a four prong vertex was found, a set of parameters were calculated for that event and tested. If the event passed a particular set of selection criteria (Table 3.4) the event was checked to see if it was a good candidate either for the decay $D^0 \rightarrow K^- K^- K^+ \pi^+$ or for $D^0 \rightarrow K^- \pi^- \pi^+ \pi^+$. This check was performed by assuming the decay could be either one and trying to reconstruct the D^0 mass. If either reconstructed mass ($KKK\pi$ or $K\pi\pi\pi$) was between 1.7 GeV and 2.0 GeV, that event was written to the output.

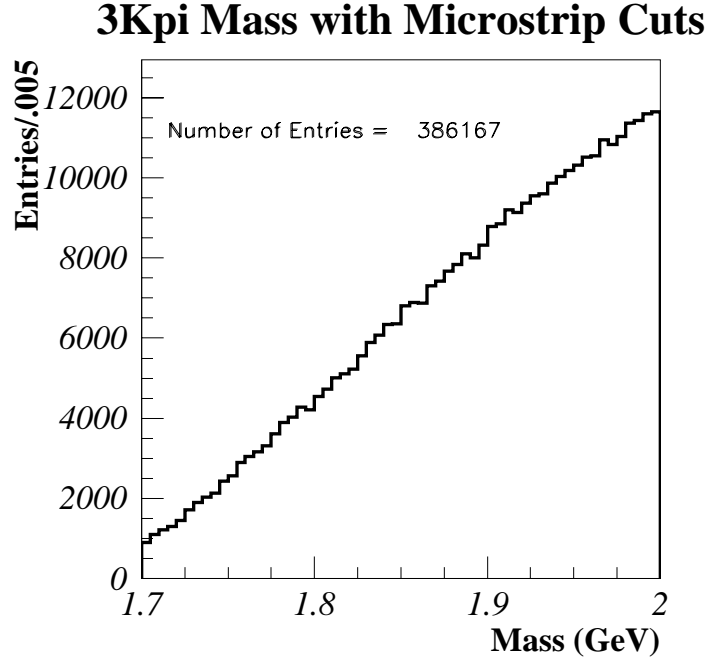
The E791 vertex algorithm was optimized to find vertices with different multiplicities; thus, its efficiency finding four prong vertices was not optimum. For this reason, some actual four prong vertices were partially reconstructed as two or three prong vertices. The microstrip algorithm recovered some of the vertices that were actually four pronged but reconstructed as three pronged, by trying to add a SESTR track to form a four prong vertex. The events thus recovered were labeled as SEED3

Parameter	Microstrip Level Cuts	
	$KKK\pi$	$K\pi\pi\pi$
CHIS	< 15	< 15
$Z_{secVert}$	< -0.35	< -0.35
SDZ	> 8	> 8
DIP	$< 100 \mu m$	$< 100 \mu m$
PTBL	$< .5 \text{ GeV}$	$< .5 \text{ GeV}$
SDZT	> 0	> 0
CVK	0.10	> 0.13
SDCA	no cut	> 4

Table 3.4: Cuts used at Microstrip Level

while the others, in which all four prongs were found by the topological vertexing algorithm, were labeled as SEED4. These two sets of data had—for obvious reasons—very different CHIS distributions and significantly different behavior of other parameters. For this reason, the two data sets were analyzed separately until they were merged at the very final stage.

Table 3.4 shows the cuts that were used for both $D^0 \rightarrow K^-K^-K^+\pi^+$ and $D^0 \rightarrow K^-\pi^-\pi^+\pi^+$ decay modes at microstrip level. The most important difference between the $KKK\pi$ cuts and the $K\pi\pi\pi$ cuts is the difference in the cut on SDCA; for $K\pi\pi\pi$, events with $SDCA < 4$ are almost all background, but for $KKK\pi$ this is far from being true, because the Q value of the $KKK\pi$ decay is much lower and

Figure 3.2: $KKK\pi$ mass with microstrip cuts

hence the opening angle of the daughter tracks of $KKK\pi$ is much smaller than those of $K\pi\pi\pi$ decay. For this reason, the projected daughter tracks of $KKK\pi$ decay get much closer to the primary vertex than those of $K\pi\pi\pi$ decay do, resulting in much lower SDCA.

The microstripped events fit onto four DSTs. Fig. 3.2 shows the $KKK\pi$ mass distribution obtained with the microstrip cuts. The data obtained with microstrip cuts were then processed through another program that calculated several tens of parameters associated with each event. An NTUPLE of these events with the calculated parameters was then made for fine tuning selection criteria and final analysis.

Chapter 4

Optimizing Event Selection

Criteria

At this stage, where the optimization of the $D^0 \rightarrow K^- K^- K^+ \pi^+$ event selection criteria was performed, the data sample obtained in the microstrip level was thoroughly studied to understand the behavior of signal and background events as functions of event parameters (section 3.4.1). To avoid bias, a “blind” analysis (section 4.1) —probably the most significant feature of the adopted method of analysis— was carried out to optimize the sensitivity¹ of the $KKK\pi$ signal with the help of a large Monte Carlo data sample.

¹Though $S/\sqrt{S+B}$ was the most important parameter that was looked at in the course of optimization, it was not the only factor that determined the final selection criteria.

4.1 The Blind Analysis

The principle of the “blind” analysis is to avoid looking at the signal region in the data sample until the “optimal” selection criteria are chosen [18]. This prevents one from tuning the cuts to enhance statistical fluctuations up or down in the signal region. Such approach is crucial when searching for a rare or forbidden decay, or when the data sample is expected to produce a signal of relatively small statistical significance. The analysis described in this thesis falls into the latter category.

In this analysis, the window ($1.845 \text{ GeV} < M_{KKK\pi} < 1.885$) in the $KKK\pi$ mass histogram was closed to avoid looking at the best $KKK\pi$ candidates even by accident. That region was examined only after optimization of selection criteria was completed. A Monte Carlo data sample of 500,000 $KKK\pi$ events was generated to model the behavior of the $KKK\pi$ signal events, and real data were used to study the behavior of background events.

4.2 Monte Carlo Data

Given the size of the E791 data sample, our reconstruction efficiency, and the expected branching ration, one could only expect to observe 10 - 50 $KKK\pi$ signal events in the final $KKK\pi$ mass histogram. The low statistics of the $KKK\pi$ signal

events made a direct analysis of sensitivity using real data inappropriate; hence, making a “blind” analysis favorable. A Monte Carlo data sample of 500,000 $D^0 \rightarrow K^- K^- K^+ \pi^+$ events (250,000 $D^0 \rightarrow K^- K^- K^+ \pi^+$ and 250,000 $\bar{D}^0 \rightarrow K^+ K^+ K^- \pi^-$) were therefore generated to model the behavior of the real $D^0 \rightarrow K^- K^- K^+ \pi^+$ signal events. The statistics of the normalization channel $D^0 \rightarrow K^- \pi^- \pi^+ \pi^+$ was rich, and 500,000 of Monte Carlo $D^0 \rightarrow K^- \pi^- \pi^+ \pi^+$ events (250,000 $D^0 \rightarrow K^- \pi^- \pi^+ \pi^+$ and 250,000 $\bar{D}^0 \rightarrow K^+ \pi^+ \pi^- \pi^-$) were also generated. The goal was to compare the $KKK\pi$ Monte Carlo data, the $K\pi\pi\pi$ Monte Carlo data, and the $K\pi\pi\pi$ real data to understand and validate the Monte Carlo representation of different aspects of the $KKK\pi$ decay. These Monte Carlo data were also used to estimate the detector efficiency for each decay channel.

The Monte Carlo events were generated using the E791 implementation of the LUND Monte Carlo package (JETSET 7.401 and PYTHIA 5.702 [19]). This algorithm simulated particle interactions and decays, propagated the generated particles through the detector with a detailed detector simulation, digitized the output to simulate the actual digitization of the E791 detector, and wrote the output to the tape in the format of the real data so that they could be read and processed the same way as the real data were.

4.3 Optimizing Analysis Cuts

The $KKK\pi$ analysis cut optimization was performed in two stages. In the first, the distribution of each parameter was studied in signal and background samples. These initial studies produced event selection criteria right away, but sometimes they suggested a closer look. In the second stage, a subset of the parameters that were initially studied was chosen to form a combined variable named Figure of Merit (FOM) (section 4.5). A cut on that variable was optimized instead of optimizing the cut on each parameter that constitutes FOM.

4.3.1 Signal and Background Distributions

For each parameter studied, signal and background distributions were generated. The signal region was selected to be from 1.845 GeV to 1.885 GeV. An “equal sideband background subtraction” was carried out on the parameter distributions of the events in the signal region. To do this, events from 1.765 GeV to 1.805 GeV and those from 1.925 GeV to 1.965 GeV were taken and their average parameter distribution was subtracted from that within the signal region. To make the background distributions, all the events outside the signal region (from 1.845 GeV to 1.885 GeV) were used. In the case of $K\pi\pi\pi$, both background and signal were taken from real data. For $KKK\pi$, background was taken from real data, but the signal distributions

were made from the Monte Carlo data. Each distribution was normalized by its total number of entries for comparison.

The top two plots of Fig. 4.1 show typical examples of such distributions. The top left plots show signal and background distribution of DIP for $KKK\pi$ candidates. These plots were made to contrast the behavior of signal and background of those events. The top right plots show similar distributions for $K\pi\pi\pi$ candidates. These plots helped compare $KKK\pi$ distributions with $K\pi\pi\pi$ distributions. On the bottom right are the signal distributions of Monte Carlo $KKK\pi$, Monte Carlo $K\pi\pi\pi$, and real data $K\pi\pi\pi$. The latter two signal distributions were used to see how well Monte Carlo data tracked real data. The former two were used to closely compare and contrast the signal distributions of Monte Carlo $KKK\pi$ and $K\pi\pi\pi$ hoping that would reflect the similarity of those distributions in real data.

4.3.2 Plots of Sensitivity vs. Cut

Using the parameter distributions for background and background subtracted signal, integrated distributions that accumulate from zero or taper off from their maximum value—depending on the cut type—were made. For the distributions whose cuts select the events with a value below the cut, distributions that accumulate from zero were used in calculating the sensitivity $S/\sqrt{S+B}$. The number of $KKK\pi$

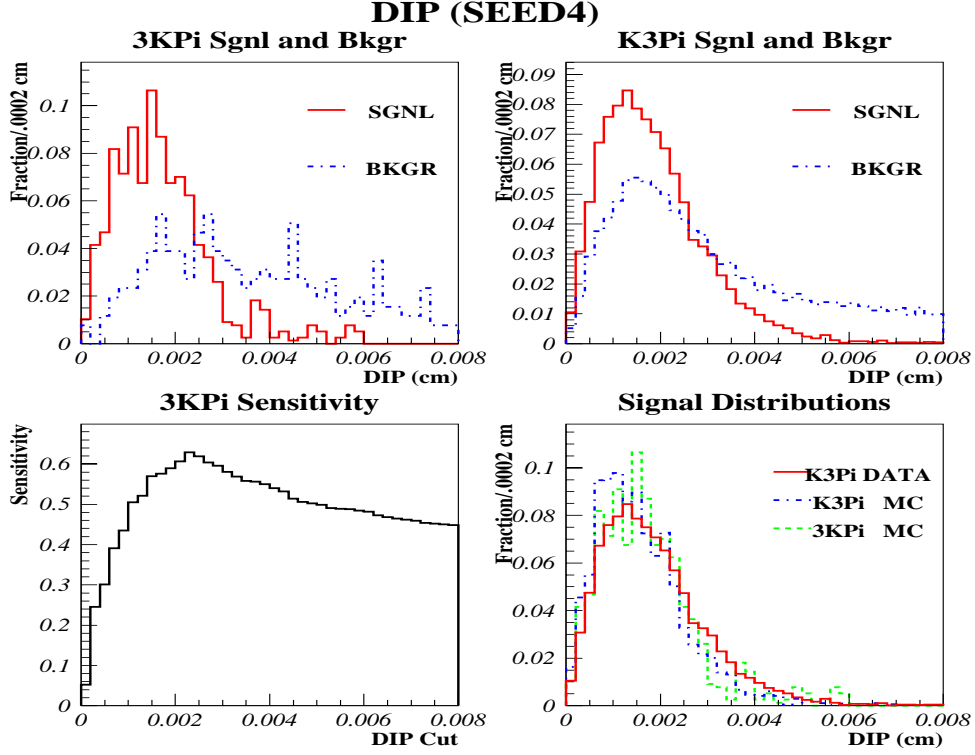


Figure 4.1: DIP distributions of SEED4 $KKK\pi$ and $K\pi\pi\pi$ signal and background events and the variation of $KKK\pi$ sensitivity with the DIP cut.

background event was taken directly from the plots made. That of $KKK\pi$ signal events was taken as the number of $K\pi\pi\pi$ signal events obtained with a similar set of cuts and scaled down by the expected relative branching ratio ($,_{KKK\pi}/,_{K\pi\pi\pi} = 0.0028$ from E687 [7]) and the relative detector efficiency calculated using Monte Carlo ($\epsilon_{rel} = \frac{\text{total number of MC } KKK\pi \text{ signal events}}{\text{total number of MC } K\pi\pi\pi \text{ signal events}}$). Mathematically this reads,

$$\text{sensitivity} = \frac{\epsilon_{rel} \times ,_{rel} \times S_{K\pi\pi\pi} \times \sigma_{KKK\pi}}{\sqrt{\epsilon_{rel} \times ,_{rel} \times S_{K\pi\pi\pi} \times \sigma_{KKK\pi} + B_{KKK\pi} \times \beta_{KKK\pi}}}$$

where S and B are total number of signal and background events and σ and β are fractional values of S and B taken from the accumulating or tapering distributions that have been normalized by the total number of entries. For the cuts that select events with a value greater than the cut, the same procedure, but with distributions that taper off from their maximum values, were used.

On bottom left of Fig. 4.1 is a typical example of a such plot. It was used to decide how to cut on DIP in SEED4 events. The optimal cut suggested by such a plot was sometimes adjusted after comparing the Monte Carlo $KKK\pi$, Monte Carlo $K\pi\pi\pi$, and real data $K\pi\pi\pi$ signal distributions shown at bottom right.

4.3.3 FOM: The Figure of Merit

Using the sensitivity vs. cut plots, a set of variables were selected to make a combined Figure Of Merit (FOM, section 4.5) and apply a cut on it. For this purpose, parameters whose sensitivity peaks with the cut, but changes moderately as the cut varied from the optimal point, were selected. A parameter whose sensitivity plot peaks, but drops rapidly is more likely to dominate and keep the sensitivity down, even in the vicinity of the peak while one with a slowly varying peak is less likely to improve the sensitivity. Further, all the parameters used in FOM should

be uncorrelated. The three CVKs (CVK1, CVK2, and CVK3), ² DIP, COSSP and MRAT (for SEED3 only) were selected to make FOM.

4.4 Cuts before FOM

Much of the help in deciding the optimal cut on a parameter was obtained from the plot that described the variation of sensitivity with the cut on the parameter in question. The cut that is suggested by that plot was adjusted after comparing the Monte Carlo and real data signal and background distributions of $KKK\pi$ and $K\pi\pi\pi$ data. The background was always taken from real data. The real $KKK\pi$ signal region was never examined (“blind”); only Monte Carlo data were used to model the behavior of $KKK\pi$ signal events. With this procedure, the “box”³ cuts before FOM were selected. Parameters to form FOM were also selected.

4.4.1 DIP

Fig. 4.1 shows signal and background DIP distributions and the variation of sensitivity with the DIP cut for SEED4 candidates. Monte Carlo $K\pi\pi\pi$ signal peaks at a lower DIP value and falls off faster than its real data counterpart does. This means that, on average, DIP is lower for Monte Carlo than it is for data. Thus, the

²CVK1, CVK2 and CVK3 correspond to the Čerenkov identification probability of the first, second, and third kaon. The first and second kaons are the ones with equal sign and the third is the one with opposite sign. Among the first two, the first is the one that comes first in the track list.

³A simple cut on a parameter which selects only the events with the parameter value either less than or greater than—but not both—the cut value is said to be a box cut.

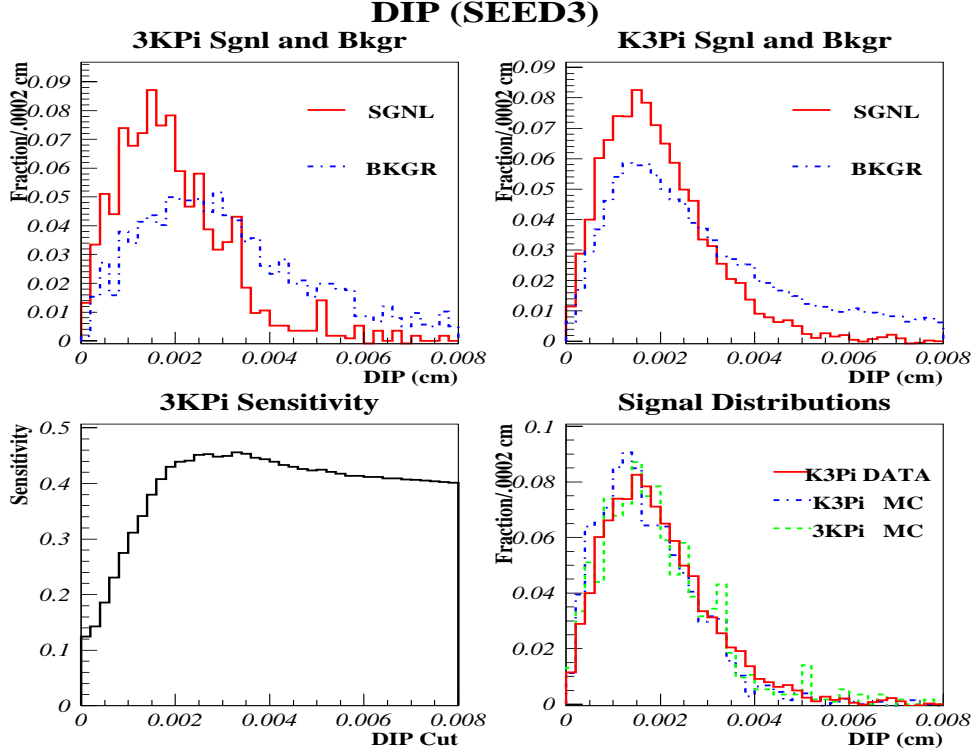


Figure 4.2: DIP distributions of SEED3 $KKK\pi$ and $K\pi\pi\pi$ signal and background events and the variation of $KKK\pi$ sensitivity with the DIP cut.

optimal cut at $DIP < 0.0025$, suggested by the sensitivity plot, that was made using Monte Carlo data, would be a little too tight. Given these facts and being a little conservative, one might choose a cut at $DIP < .0040$, but in this analysis, the DIP was included in FOM (section 4.5) with CVK, MRAT(SEED3 only) and COSSP as DIP was found to be uncorrelated with them. An overall cut at $DIP < .0060$ was made. The similar behavior of DIP in SEED3 events (Fig. 4.2) suggested adopting a similar treatment.

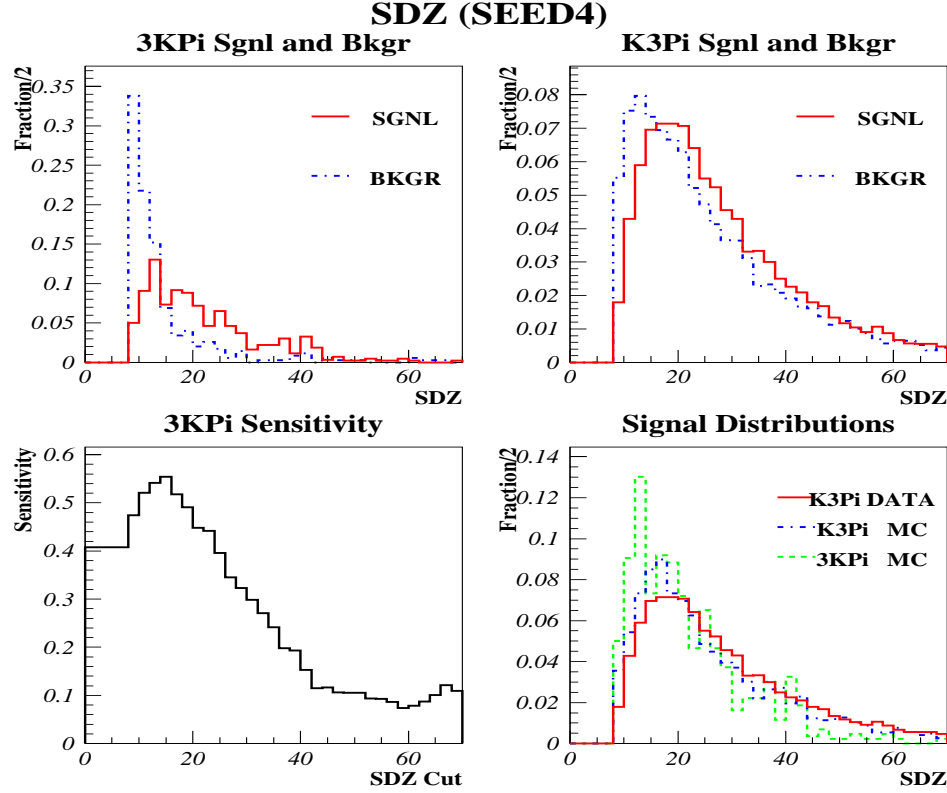


Figure 4.3: SDZ distributions of SEED4 $KKK\pi$ and $K\pi\pi\pi$ signal and background events and the variation of $KKK\pi$ sensitivity with the SDZ cut.

4.4.2 SDZ

Fig. 4.3 shows signal and background SDZ distributions and the variation of sensitivity with the SDZ Cut for SEED4 candidates. The SDZ distribution for $KKK\pi$ Monte Carlo signal events peaks at a lower SDZ than that for $K\pi\pi\pi$ Monte Carlo signal events does, because the standard deviation of the z measurement of the secondary vertex, σ_z , is on average higher for $KKK\pi$ events than for $K\pi\pi\pi$ events

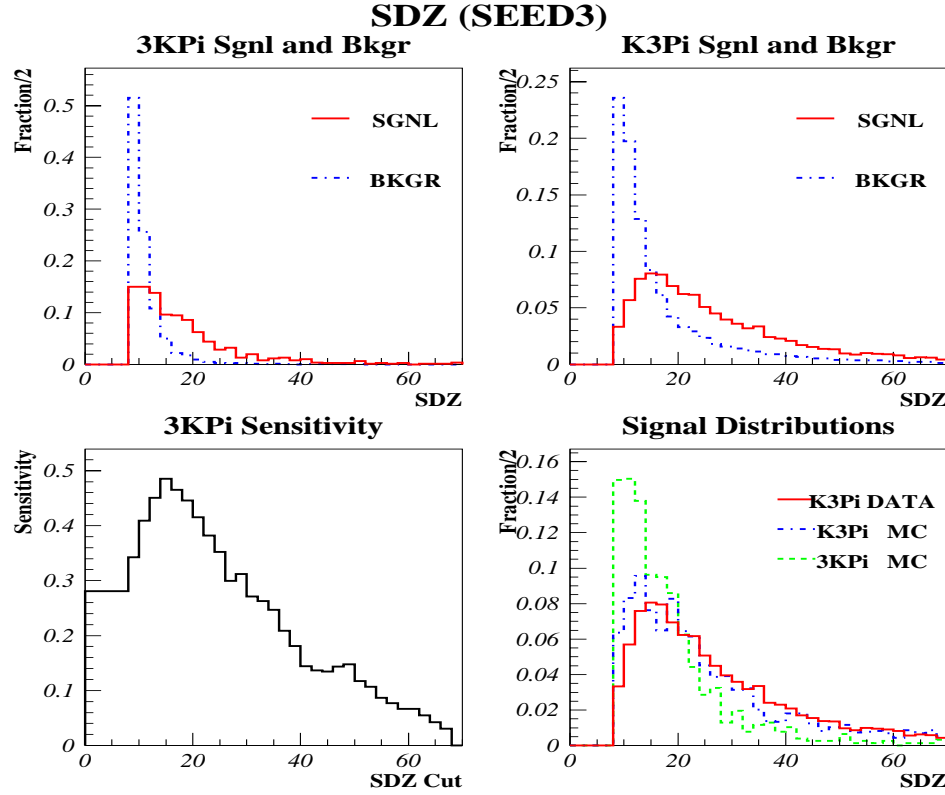


Figure 4.4: SDZ distributions of SEED3 $KKK\pi$ and $K\pi\pi\pi$ signal and background events and the variation of $KKK\pi$ sensitivity with the SDZ cut.

(Fig. 4.5). This may be attributed to the lower Q-value of the $KKK\pi$ decay — compared to the $K\pi\pi\pi$ decay — that gives rise to smaller opening angles of the decay tracks and hence higher uncertainties in vertexing. A cut at $SDZ > 10$ was selected for SEED4, but the sensitivity plot for SEED3 SDZ (Fig. 4.4) peaks at a little higher value than does that for SEED4 SDZ . So the SDZ cut for SEED3 events was set at $SDZ > 12$.

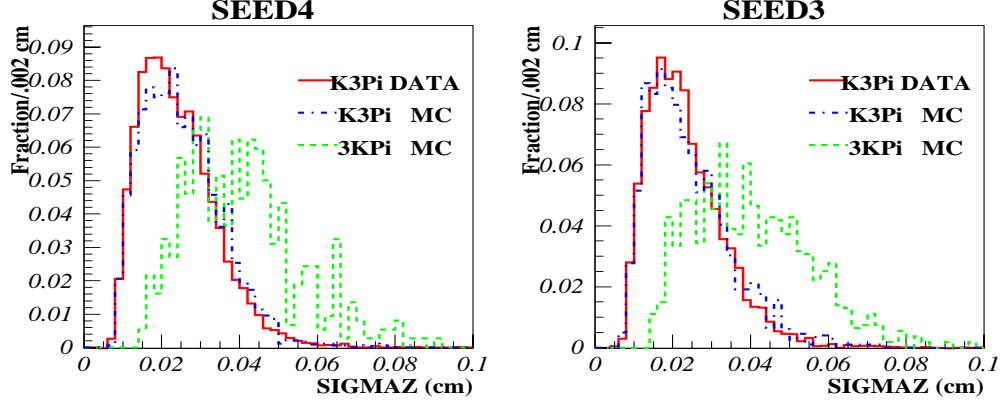


Figure 4.5: SEED4 (left) and SEED3 (right) σ_z distribution of $KKK\pi$ and $K\pi\pi\pi$ signal events.

4.4.3 CVK, PCVK, and CVP

Fig. 4.6 shows the Čerenkov probability distributions of the kaons. The left plots show those for $KKK\pi$ signal and background events, while right plots show those for $KKK\pi$ and $K\pi\pi\pi$ signal events. The top, the middle, and the bottom plots corresponds to CVK1, CVK2, and CVK3 respectively. In this analysis, CVK1 and CVK2 denote the Čerenkov probabilities of the two kaons with the same sign and CVK3 denotes that of the kaon with the opposite sign. Kaon 1 (with CVK1) is the kaon that comes first among the first two kaons in the track list. $K\pi\pi\pi$ CVK distribution corresponds to its only kaon. Fig. 4.7 shows the corresponding plots for SEED3.

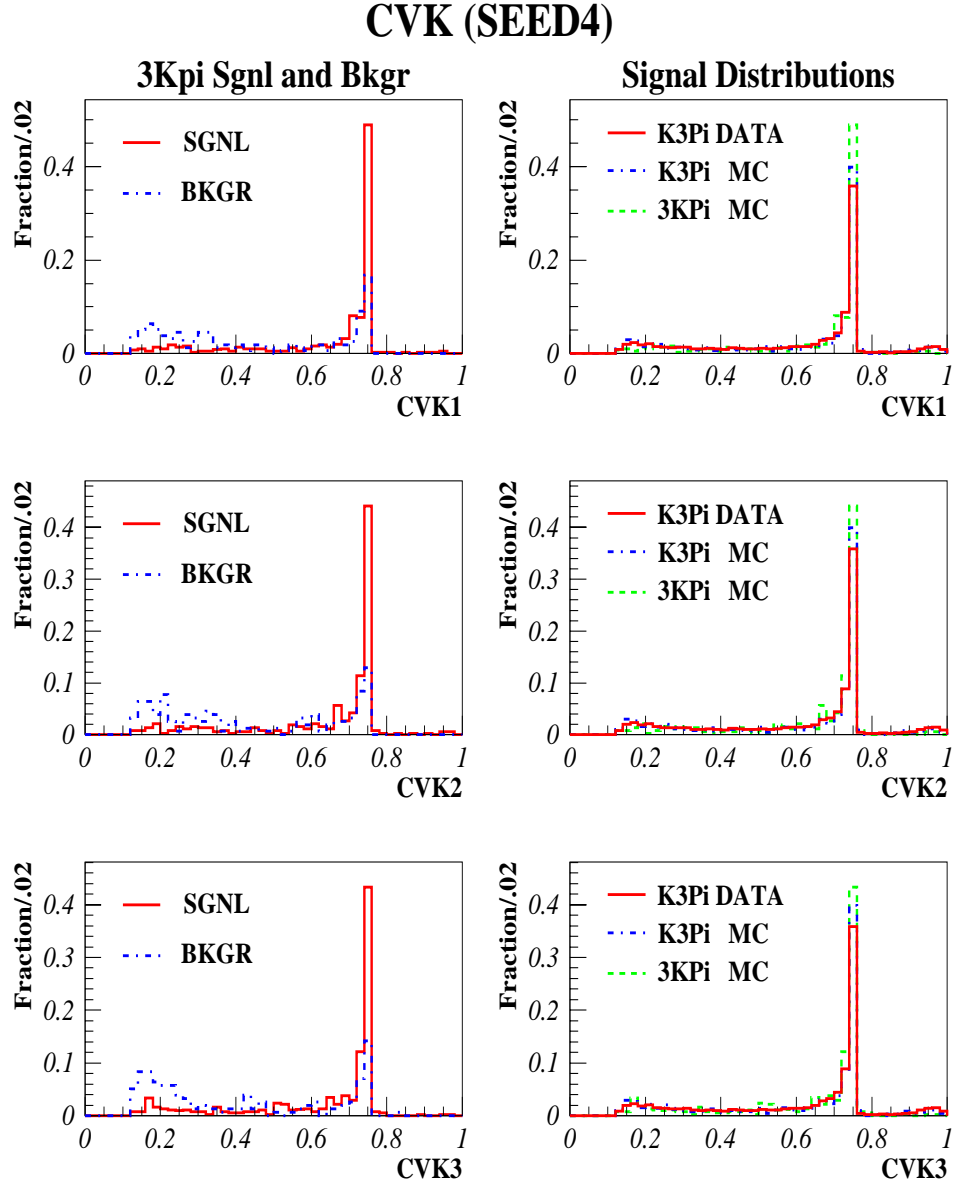


Figure 4.6: CVK distributions of SEED4 $KKK\pi$ signal and background events and $K\pi\pi\pi$ signal events. The top, the middle, and the bottom plots corresponds to CVK1, CVK2, and CVK3 respectively. $K\pi\pi\pi$ CVK distribution corresponds to its only kaon.

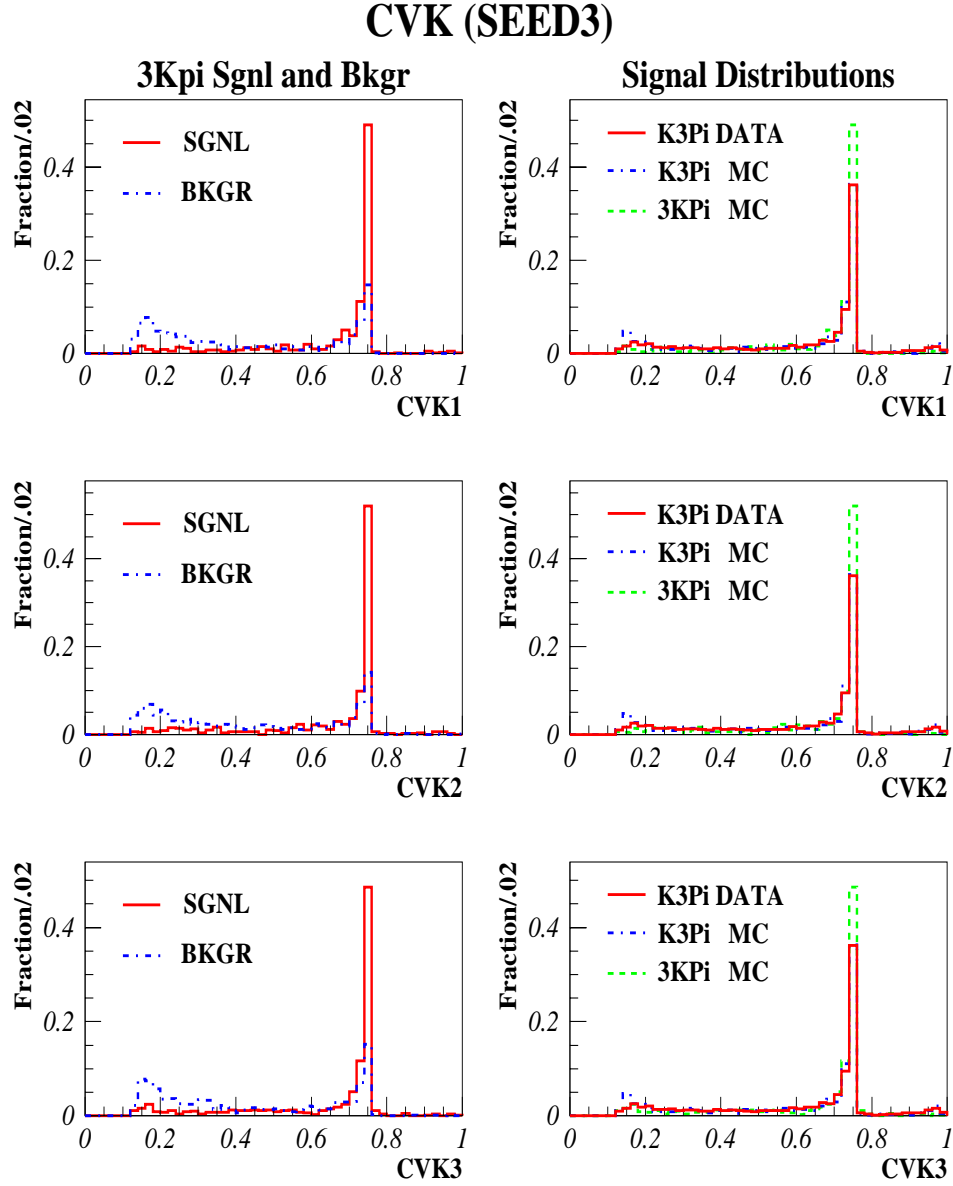


Figure 4.7: CVK distributions of SEED3 $KKK\pi$ signal and background events and $K\pi\pi\pi$ signal events. The top, the middle, and the bottom plots corresponds to CVK1, CVK2, and CVK3 respectively. $K\pi\pi\pi$ CVK distribution corresponds to its only kaon.

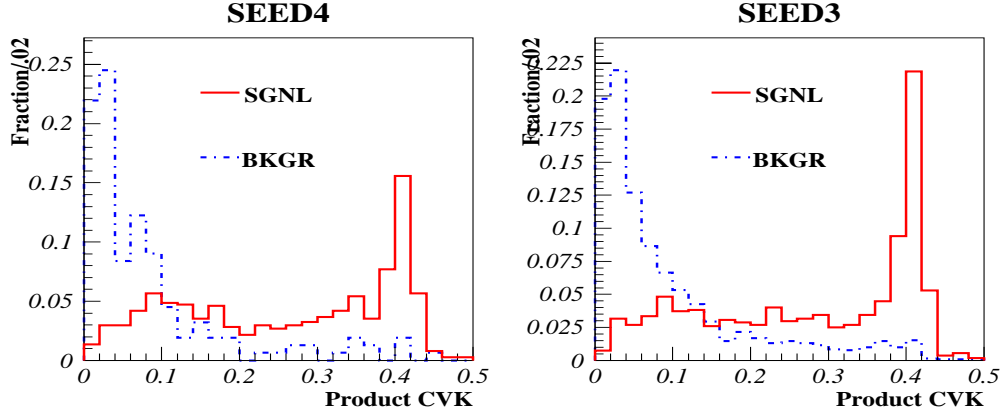


Figure 4.8: SEED4 (left) and SEED3 (right) product CVK (PCVK) distribution of $KKK\pi$ signal and background events. A cut at .13 has been applied on individual CVKs.

The behavior of the product of Čerenkov probabilities of all three kaons was also studied. Fig. 4.8 shows the distribution of the product CVK of all three kaons ($PCVK = CVK1 \times CVK2 \times CVK3$) for SEED4 (left) and SEED3 (right) $KKK\pi$ events. A cut at .13 has been applied for all three kaons of the $KKK\pi$ decay to get rid of the kaons with CVK at or lower than the *a priori* probability of kaons. Similar plots with $CVK > .1$ and $CVK > .4$ were also made in the further study. The cut at .1 kept the kaons with *a priori* probability. The cut at .4 is a near-optimal cut had we decided to use CVK individually.

According to individual and product CVK plots, one can conclude that the sensitivity of the final results could be improved either by cutting on individual CVK or on product CVK, but when looked for parameters to form FOM (section 4.5) the

three CVKs were found to make a good set along with with DIP, MRAT (SEED3 only), and COSSP. FOM was also expected to improve the sensitivity better than cutting on individual parameters does. Each kaon track was required to have $CVK > 0.20$, and then the values of CVK1, CVK2, and CVK3 were used in calculating FOM.

Similar studies of the Čerenkov identification probability of the pion of the $KKK\pi$ decay, CVP, did not seem to help improve the sensitivity. It would make more sense to say that being ignorant of CVP did not seem to reduce the sensitivity. This can be attributed to the pion's high *a priori* probability (0.81) which is 6.75 times higher than that of kaon (0.12). If a track was not identified, it is very much likely to be a pion. No cut on CVP was made.

4.4.4 PTBL

Figs. 4.9 and 4.10 show signal and background PTBL distributions and the variation of sensitivity with the PTBL cut for SEED4 and SEED3 candidates respectively. The distribution of PTBL of Monte Carlo signal event peaks at a lower value and falls faster than does its data counterpart. The $KKK\pi$ PTBL distributions peaks even lower and falls even faster. This would result from the $KKK\pi$ daughters having lower transverse momenta, and hence any imbalance being low. The fact that

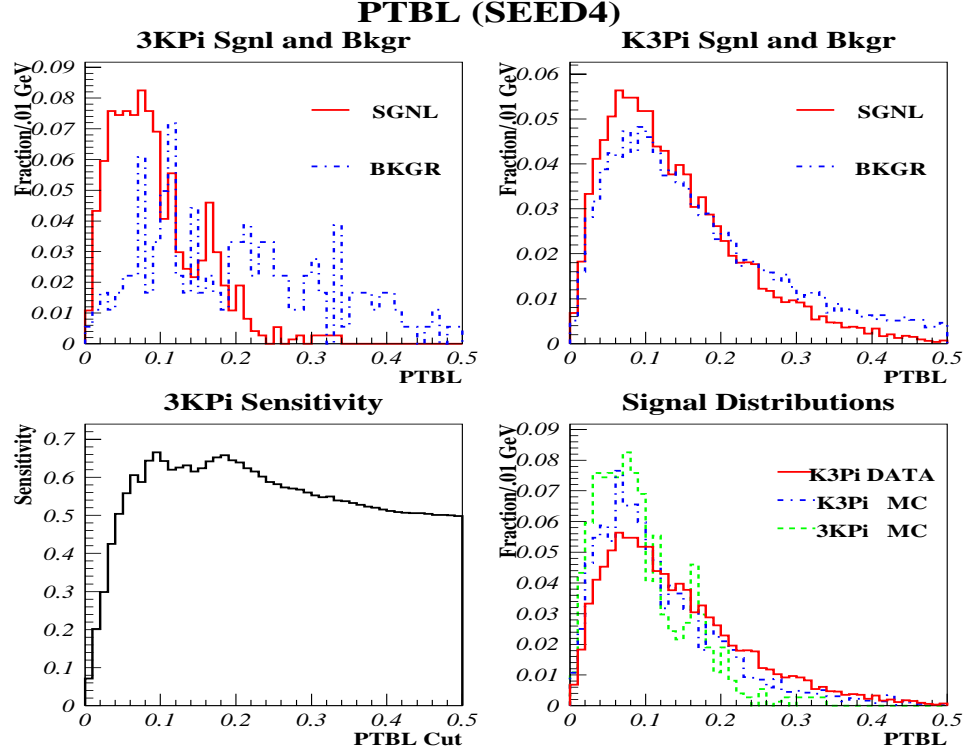


Figure 4.9: PTBL distributions of SEED4 $KKK\pi$ and $K\pi\pi\pi$ signal and background events and the variation of $KKK\pi$ sensitivity with the PTBL cut.

$KKK\pi$ PTBL is low on average compared to $K\pi\pi\pi$ helps us eliminate background while losing much less signal than one would if the same cut was applied to $K\pi\pi\pi$ candidates. The sensitivity vs. PTBL cut plot suggested a cut below 0.2, but that value was increased based on the differences in signal distributions (Figs. 4.9 and 4.10 bottom right) and the past experience of other E791 analyses. A cut at $PTBL < 0.25$ was selected for both SEED4 and SEED3.

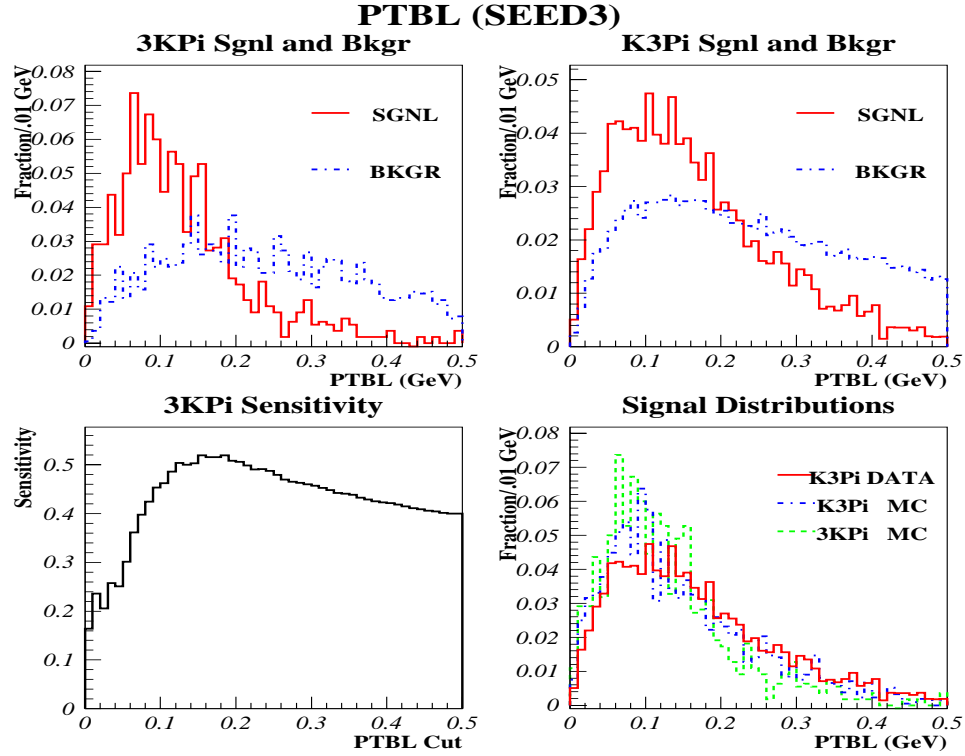


Figure 4.10: PTBL distributions of SEED3 $KKK\pi$ and $K\pi\pi\pi$ signal and background events and the variation of $KKK\pi$ sensitivity with the PTBL cut.

4.4.5 SDCA

Fig. 4.11 shows SDCA distributions of $KKK\pi$ signal and background events (left) and sensitivity vs. SDCA cut (right). On top are the plots for SEED4 events while on bottom are the plots for SEED3 events. The analyses done for decays with relatively high Q-values had a cut on SDCA typically around 4. The $KKK\pi$ decay has a relatively low Q value which results in a smaller opening angle of the

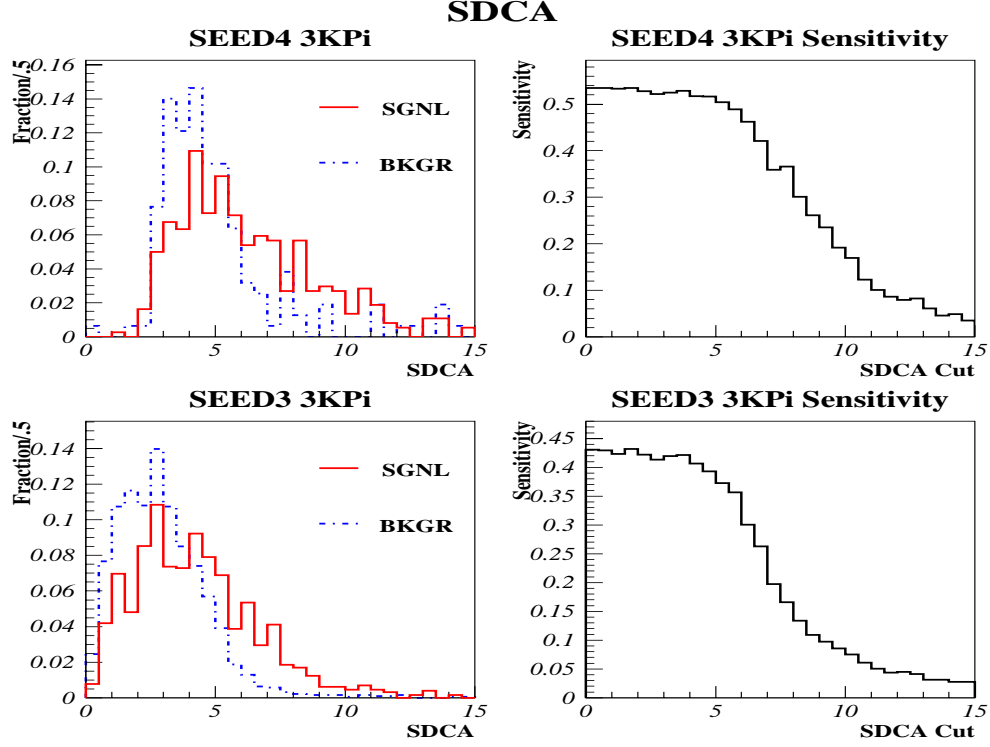


Figure 4.11: SEED4 (Top) and SEED3 (bottom) SDCA distributions of $KKK\pi$ signal and background events and sensitivity vs. SDCA cut.

decay tracks, hence a lower SDCA value. For this reason, cutting on SDCA not only gets rid of the background events, but also gets rid of a significant fraction of signal events. The plots at the left in Fig. 4.11 clarify the disadvantage of cutting on SDCA. According to the plots at the right in Fig. 4.11, no gain in sensitivity may be achieved by loosening the SDCA cut, but the decision was to loosen the cut all the way down to 0 —*i.e.* no cut on SDCA— to keep the signal events and hoping to get rid of the background by other means.

4.4.6 SDZT

Fig. 4.12 shows the plots of SDZT. The top left figure shows SDZT distributions for $KKK\pi$ signal and background events while that on top right shows those for $K\pi\pi\pi$ signal and background events. The accumulation of background events around $\text{SDZT} = 0$ is due to showering in the target foil. This can be clearly seen for $K\pi\pi\pi$ events, but the background accumulation of $KKK\pi$ candidates is slim around $\text{SDZT} = 0$; thus, distributions zoomed into the $\text{SDZT} = 0$ area were also made (middle left) to have a closer look at that region. In the middle, on the right, is the sensitivity vs. SDZT cut plot made for $KKK\pi$ candidates. This was also made zoomed into the $\text{SDZT} = 0$ area to get a better estimate of the optimal cut value. From the middle plots, a cut at $\text{SDZT} > 1$ was selected for SEED4. SEED3 $KKK\pi$ candidates do not show any background accumulation around $\text{SDZT} = 0$ (Fig. 4.12 bottom left); thus, no SDZT cut was applied on SEED3 $KKK\pi$ candidates.

The $K\pi\pi\pi$ SDZT distributions show a bump around 12 and those of $KKK\pi$ show such somewhere around 20 (Fig. 4.12). This behavior was studied by identifying which side of and how far from the target foil, that has the primary vertex, the secondary vertex sits. The bump in both signal and background distributions are due to the events that are closest (within about 7.5 mm) to and in front of the target foil that the primary vertex is in. This is where most of the charm particles decay.

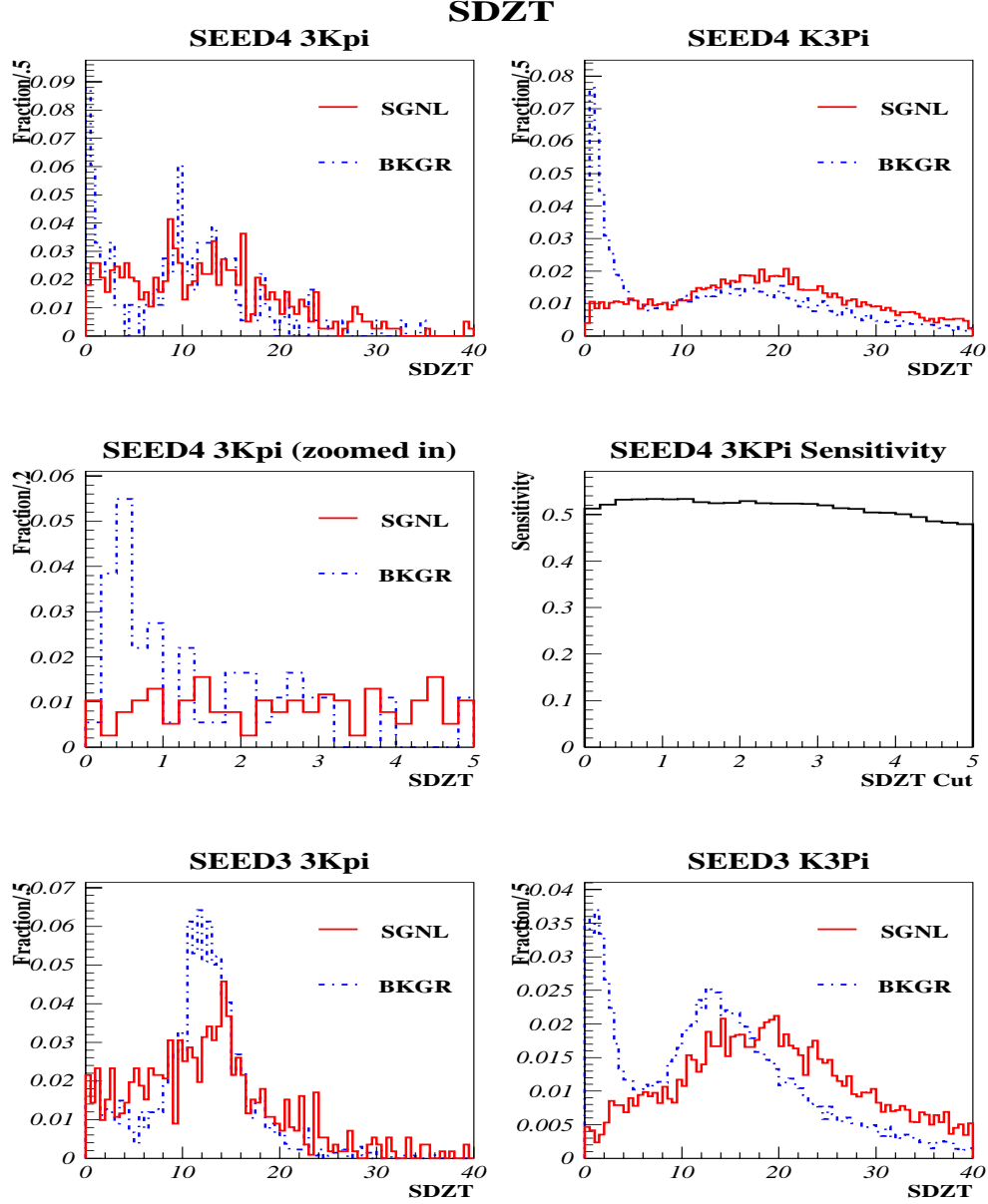


Figure 4.12: SEED4 (Top and middle) and SEED3 (bottom) SDZT distributions of $KKK\pi$ and $K\pi\pi\pi$ signal and background events and SEED4 sensitivity vs. SDCA cut (middle right).

4.4.7 PTSQ and SPTSQ

The top and the middle plots of Fig. 4.13 show the SEED4 PTSQ distributions for $KKK\pi$ and $K\pi\pi\pi$ signal and background events. On the bottom are the PTSQ vs. $KKK\pi$ mass scatter plots. On average, a $KKK\pi$ event would have a much lower PTSQ than a $K\pi\pi\pi$ event would, due to the lower Q-value of $KKK\pi$ decay (Fig. 4.13 middle plot). The PTSQ distribution of the $KKK\pi$ background events spans beyond that of $KKK\pi$ signal events in both directions (Fig. 4.13, middle plot). The scatter plots of PTSQ vs. $KKK\pi$ mass (Fig. 4.13 bottom) show that the background events with PTSQ higher than that of signal events all come from the right wing of the background region of the $KKK\pi$ mass distribution. Any cut on PTSQ that would get rid of the background events with higher PTSQ than the signal event PTSQ will modify the shape of the background with a bias which would affect the understanding of the background shapes and sources. To get around this, SPTSQ, which is PTSQ scaled by the maximum PTSQ for the individual event, was introduced.

Fig. 4.14 shows the SPTSQ distributions and SPTSQ vs. $KKK\pi$ mass plots for SEED4 events. The correlation between SPTSQ and $KKK\pi$ mass was much less than that between PTSQ and $KKK\pi$ mass; hence, the preference was to cut on SPTSQ.

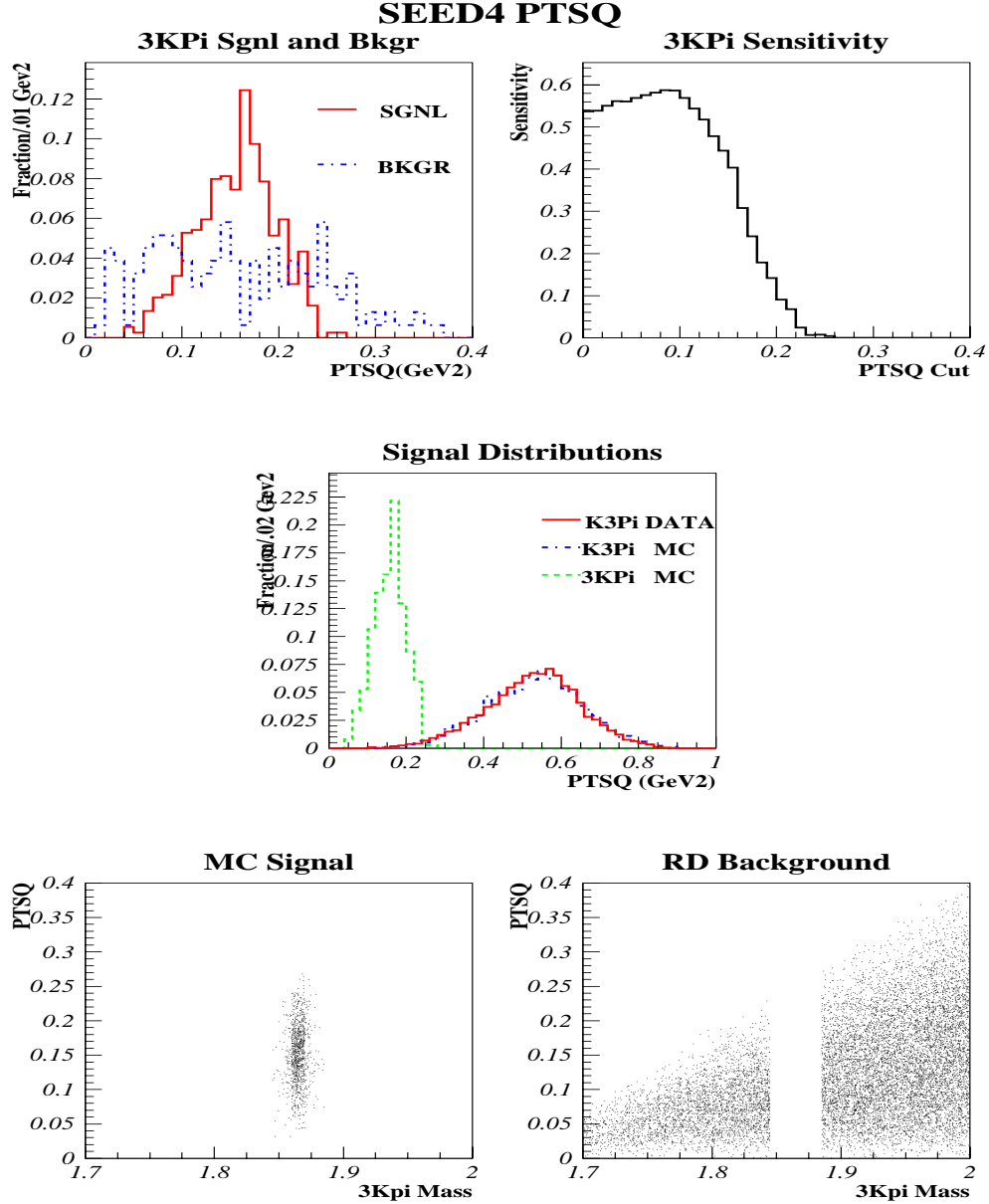


Figure 4.13: PTSQ distributions of SEED4 $KKK\pi$ and $K\pi\pi\pi$ signal and background events and sensitivity vs. PTSQ cut (top). At bottom are PTSQ vs. $KKK\pi$ mass distribution for SEED4 Monte Carlo signal (bottom left) and real data background (bottom right) events.

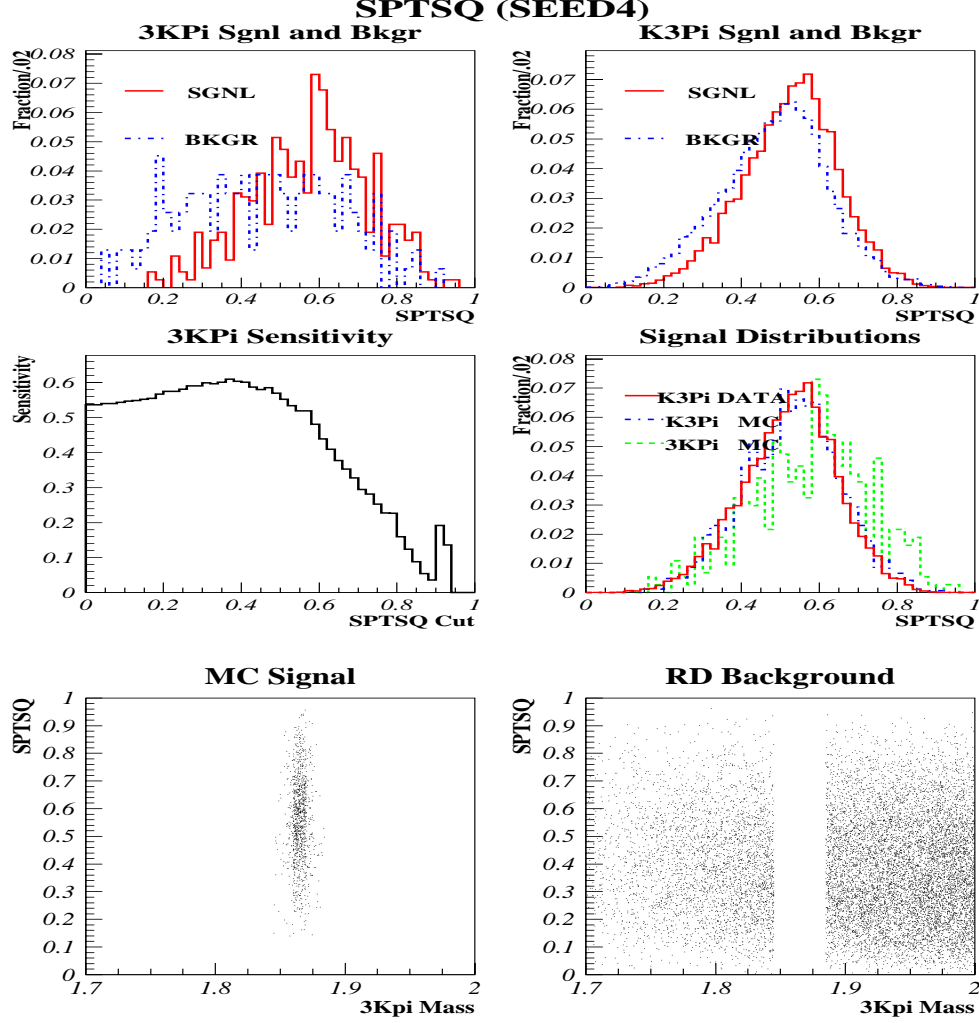


Figure 4.14: SPTSQ distributions of SEED4 $KKK\pi$ and $K\pi\pi\pi$ signal and background events and sensitivity vs. PTSQ cut. At bottom are SPTSQ vs. $KKK\pi$ mass distribution for SEED4 Monte Carlo signal (bottom left) and real data background (bottom right) events.

Figs. 4.15 and 4.16 show similar sets of plots of PTSQ and SPTSQ for SEED3 events respectively. The cuts $\text{SPTSQ} > .2$ and $\text{SPTSQ} > .3$ were selected for SEED4 and SEED3 events respectively.

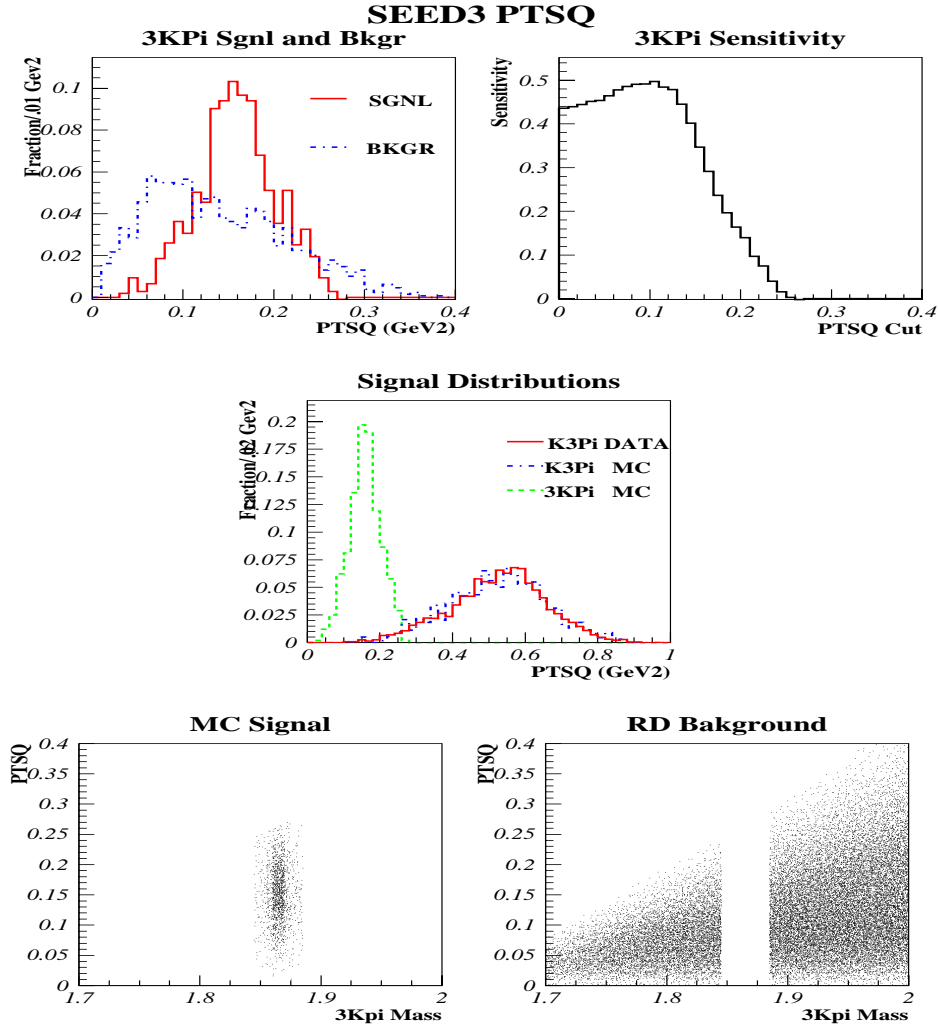


Figure 4.15: PTSQ distributions of SEED3 $KKK\pi$ and $K\pi\pi\pi$ signal and background events and sensitivity vs. PTSQ cut (top). At bottom are PTSQ vs. $KKK\pi$ mass distribution for SEED3 Monte Carlo signal (bottom left) and real data background (bottom right) events.

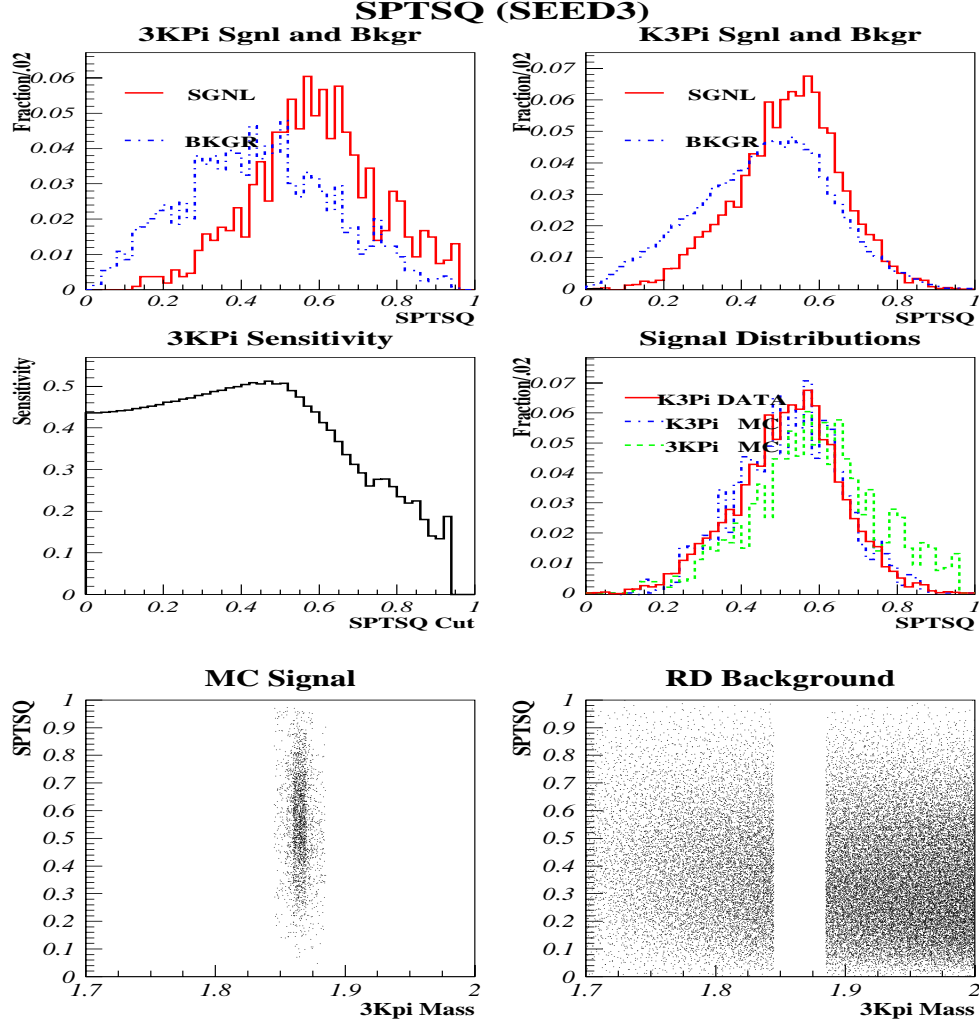


Figure 4.16: SPTSQ distributions of SEED3 $KKK\pi$ and $K\pi\pi\pi$ signal and background events and sensitivity vs. PTSQ cut. At bottom are SPTSQ vs. $KKK\pi$ mass distribution for SEED3 Monte Carlo signal (bottom left) and real data background (bottom right) events.

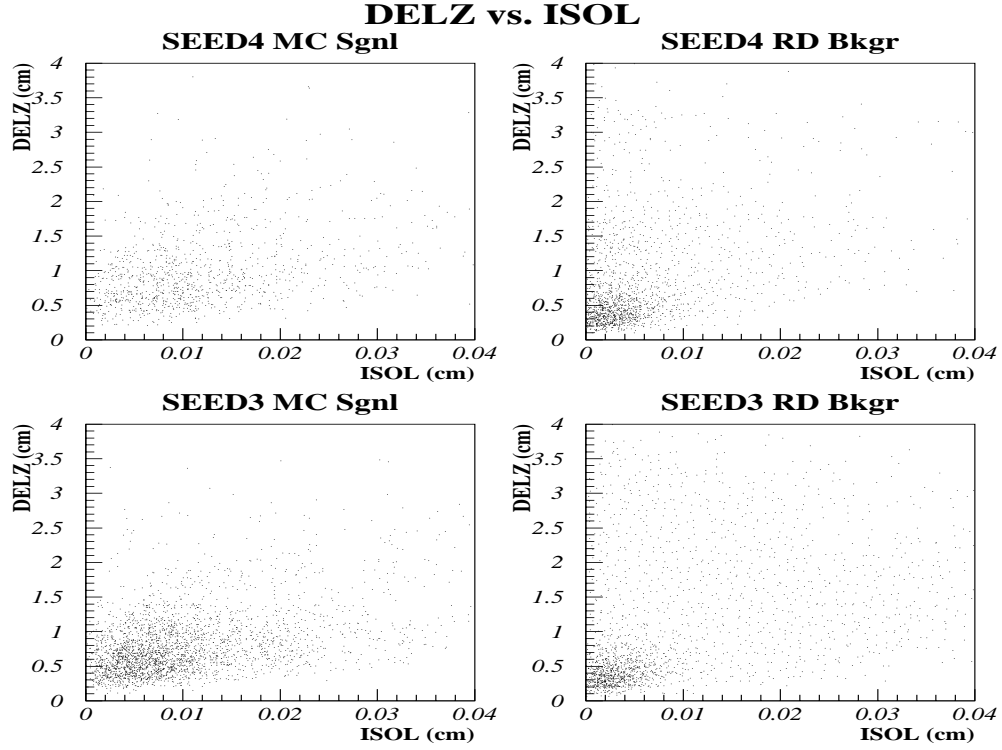


Figure 4.17: SEED4 (Top) and SEED3 (bottom) DELZ vs. ISOL scatter plots of $KKK\pi$ Monte Carlo signal (left) and real data background (right) events. The microstrip cuts (Table 3.4) have been applied.

4.4.8 DELZ and ISOL

Fig. 4.17 shows the scatter plots of DELZ vs. ISOL for both SEED4 (top) and SEED3 (bottom) Monte Carlo signal events (left) and real data background events (right), made with microstrip cuts (Table 3.4). These scatter plots show how strong the correlation between DELZ and ISOL is. For this reason, the cut on DELZ and ISOL was optimized together in a two dimensional parameter space.

Monte Carlo data were inadequate to study the behavior of signal and background with respect to ISOL. Monte Carlo data has far less background than real data does. This cleanliness leads to much higher ISOL in Monte Carlo data than in real data, hence providing a poor representation of the ISOL distribution. DELZ⁴ and ISOL of $KKK\pi$ signal events were therefore represented by those of $K\pi\pi\pi$ signal events. Before doing so, the DELZ vs ISOL distributions of $KKK\pi$ Monte Carlo signal events were compared with those of $K\pi\pi\pi$ Monte Carlo signal events to make sure they were not significantly different (Table 4.1). The assumption was, if $KKK\pi$ Monte Carlo data and $K\pi\pi\pi$ Monte Carlo data have similar DELZ vs. ISOL distributions then $KKK\pi$ real data and $K\pi\pi\pi$ real data should also have similar distributions. Tables 4.2 and 4.3 were prepared for SEED4 and SEED3 events respectively using $K\pi\pi\pi$ signal events and $KKK\pi$ background events⁵. From these tables, the cuts $\text{DELZ} > .5$.OR. $\text{ISOL} > .002$ and $\text{DELZ} > .5$.OR. $\text{ISOL} > .008$ were selected for SEED4 and SEED3 events respectively.

⁴DELZ had to be represented by $K\pi\pi\pi$ real data as DELZ cut was optimized in combination with ISOL cut.

⁵The fractions in the Table 4.1, 4.2, and 4.3 were calculated with a set of tighter cuts on the data sample to get a cleaner signal and hence better accuracy. These cuts were tighter than the microstrip level cuts were, but a little looser than the final analysis cuts turned out to be. They were $\text{DIP} < 40 \mu\text{m}$, $\text{SDZ} > 12$, $\text{PTBL} < .35 \text{ GeV}$, $\text{SDZT} > 1$, $\text{SDCA} > 2$, $\text{CVK} > .13$ and other microstrip level cuts.

DELZ (mm)	ISOL (μm)				
	0 - 20	20 - 40	40 - 80	80 - 120	120 - 200
12 - 20	0.8%	1.2%	5.0%	5.6%	6.9%
	0.5%	1.1%	4.6%	4.1%	6.0%
8 - 12	1.5%	4.6%	11.5%	12.5%	14.2%
	1.7%	3.1%	11.7%	8.5%	8.3%
5 - 8	0.8%	3.6%	8.8%	12.3%	8.8%
	2.6%	7.9%	17.0%	10.2%	5.6%
3 - 5	0.4%	0.0%	0.4%	0.4%	0.8%
	0.7%	1.6%	2.7%	1.4%	0.4%
0 - 3	0.0%	0.0%	0.0%	0.0%	0.0%
	0.0%	0.1%	0.1%	0.0%	0.0%

Table 4.1: SEED4 Monte Carlo $KKK\pi$ (upper value) and $K\pi\pi\pi$ (lower value) signal fractions with DELZ and ISOL.

DELZ (mm)	ISOL (μm)				
	0 - 20	20 - 40	40 - 80	80 - 120	120 - 200
12 - 20	3.1%	2.3%	4.6%	3.2%	3.7%
	2.9%	4.3%	2.2%	7.2%	2.9%
8 - 12	5.8%	6.4%	8.6%	6.1%	5.2%
	3.6%	6.5%	6.5%	3.6%	2.9%
5 - 8	8.8%	10.2%	13.4%	6.6%	4.6%
	11.5%	15.1%	14.4%	3.6%	0.7%
3 - 5	2.3%	2.0%	2.0%	0.7%	0.1%
	6.5%	2.9%	1.4%	1.4%	0.0%
0 - 3	0.1%	0.0%	0.0%	0.0%	0.0%
	0.0%	0.0%	0.0%	0.0%	0.0%

Table 4.2: SEED4 real data $K\pi\pi\pi$ signal fractions (upper value) and $KKK\pi$ background fractions (lower value) with DELZ and ISOL.

DELZ (mm)	ISOL (μm)				
	0 - 20	20 - 40	40 - 80	80 - 120	120 - 200
12 - 20	1.8%	2.7%	3.6%	2.5%	2.4%
	1.2%	2.1%	2.1%	1.1%	0.8%
8 - 12	4.9%	6.2%	9.0%	4.9%	4.4%
	3.7%	4.4%	4.6%	3.2%	2.0%
5 - 8	9.5%	12.2%	15.0%	6.1%	4.0%
	11.3%	17.7%	18.3%	4.7%	1.3%
3 - 5	3.2%	3.6%	3.0%	0.6%	0.3%
	6.7%	7.1%	6.1%	1.3%	0.3%
0 - 3	0.1%	0.0%	0.0%	0.0%	0.0%
	0.0%	0.1%	0.0%	0.0%	0.0%

Table 4.3: SEED3 real data $K\pi\pi\pi$ signal fractions (upper value) and $KKK\pi$ background fractions (lower value) with DELZ and ISOL.

4.4.9 CHIS and CHIP

CHIS is the parameter whose distribution for SEED3 events is most significantly different from that for SEED4 events (Fig. 4.18 top). SEED3 events tend to have much higher CHIS than SEED4 events do due to the selections made in the filter code. Monte Carlo data represents CHIS of the $K\pi\pi\pi$ events very well (Fig. 4.18 bottom right), especially at higher CHIS. For this reason, one may trust Monte Carlo data in deciding the cut on CHIS for the $KKK\pi$ signal. From the latter three plots of the Fig. 4.18, the CHIS cut on SEED3 data sample was chosen to be $\text{CHIS} < 10$.

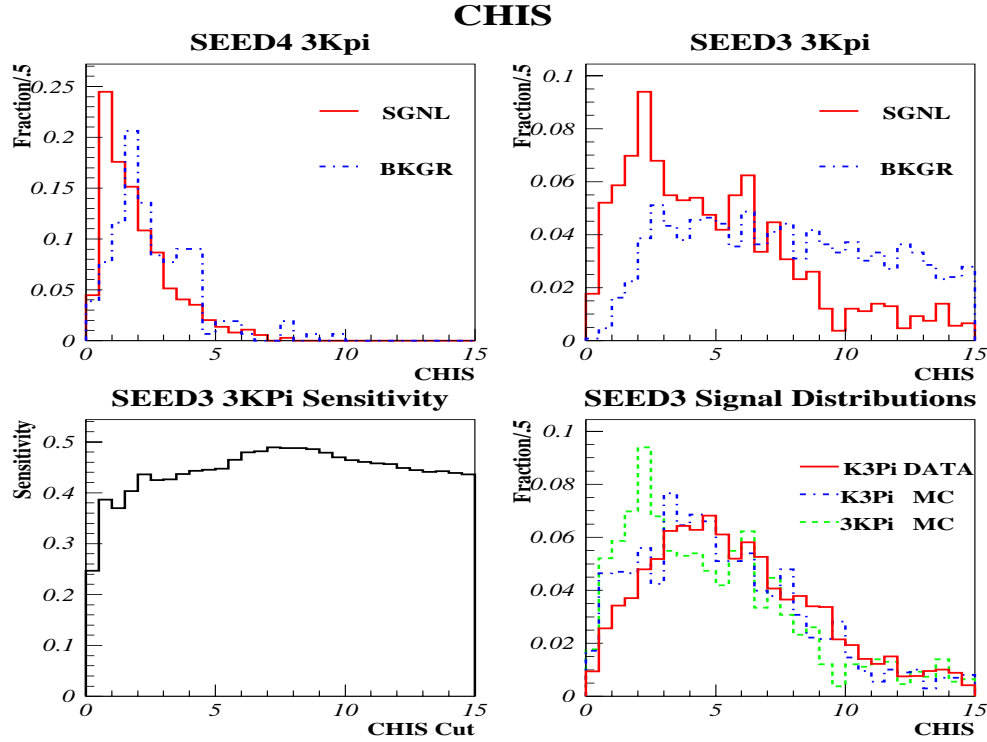


Figure 4.18: SEED4 (upper left) and SEED3 (upper right) CHIS distribution of $KKK\pi$ signal and background events, the plot of sensitivity vs. CHIS cut for SEED3 $KKK\pi$ events (bottom left), and CHIS distributions for SEED3 $KKK\pi$ signal events.

The CHIS distributions of SEED4 $KKK\pi$ signal and background events (top left of Fig. 4.18) do not promise any improvement in the sensitivity by cutting on CHIS, but neither do they warn of any disadvantage of cutting on CHIS at or above 10. A cut at $\text{CHIS} < 10$ has actually been applied to the SEED4 data sample as well as SEED3 data sample only for the convenience of having the same cut on the entire data sample; otherwise, it is trivial.

The CHIP distributions of $KKK\pi$ Monte Carlo signal and real data background seemed to promise some improvement in the sensitivity if cut on CHIP, but the CHIP distributions of real data $K\pi\pi\pi$ signal and background events showed remarkable similarity; hence, no improvement if cut on. The latter was more reliable as it came from real data and there was no reason to believe that CHIP of a $KKK\pi$ event would differ from that of a $K\pi\pi\pi$ event; thus, no cut on CHIP was made.

4.4.10 COSSP

Fig. 4.19 shows the COSSP distributions for $KKK\pi$ signal and background events (top) and sensitivity vs. SDCA cut (bottom). Plots for SEED4 and SEED3 are shown on left and right respectively. There are more signal events at lower COSSP values, and an accumulation of background events around $\text{COSSP} = 1$. One may cut on COSSP around .8, but as COSSP showed no correlation with the other parameters that were used to form FOM (section 4.5), COSSP was used in FOM.

4.4.11 CATs and RATs

This analysis used only category 3, 7, and 15 tracks. Besides that criterion, no cut on CATs (CAT, MCAT, and NCAT3) has been used as studies of the signal and background distributions indicated negligible benefit. The same was true for RAT

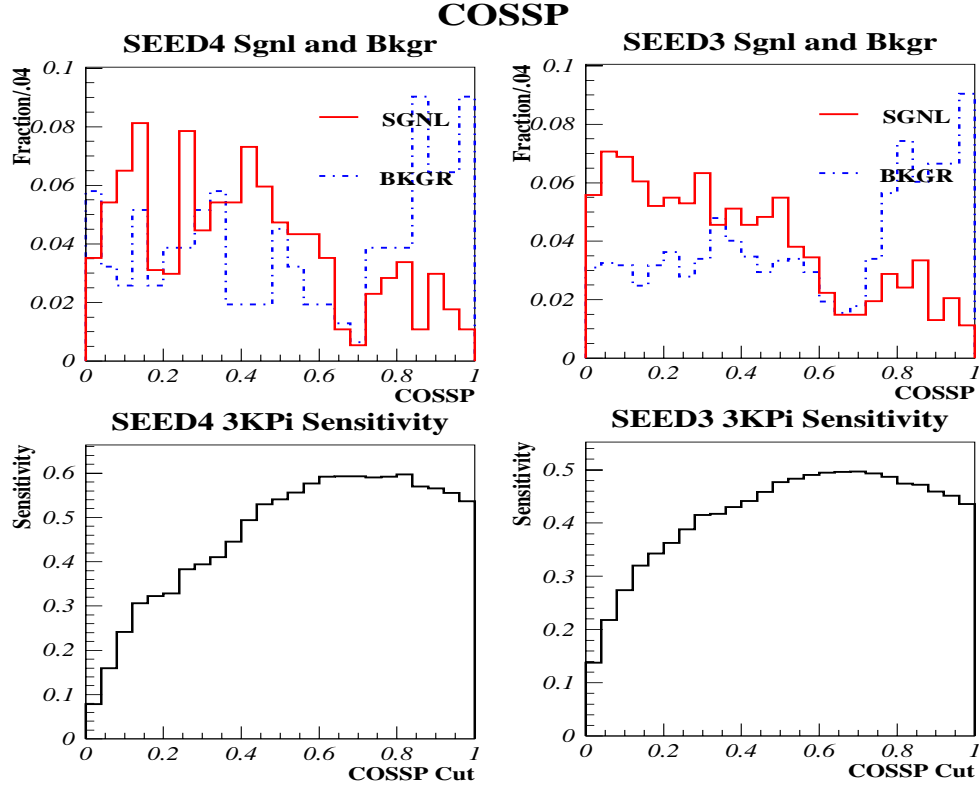


Figure 4.19: SEED4 (left) and SEED3 (right) COSSP distributions of $KKK\pi$ signal and background events (top) and sensitivity vs. SDCA cut (bottom).

and SEED4 MRAT. The SEED3 $KKK\pi$ MRAT distribution suggested that MRAT would be a good candidate for FOM. SEED3 MRAT was therefore used to make FOM after a hard cut at $\text{MRAT} < 1$, but SEED4 MRAT was not. A cut of $\text{PRAT} < .005$ has been applied on both SEED4 and SEED3 data samples to get rid of a very few background events.

4.4.12 TAU

There were no SEED4 signal events beyond $\text{TAU} = 3.5$ ps; only background events were there. A cut of $\text{TAU} < 3.5$ ps was applied on SEED4 data sample. SEED3 data sample had both signal and background events at high TAU and a cut did not seem to help improve the sensitivity; thus, no cut was made on SEED3 TAU.

4.5 FOM: Figure of Merit

FOM is a variable that is derived from other event parameters. It gives a measure of relative likelihood that an event comes from the signal sample or background. In the course of defining the FOM, we use a set of parameters that discriminate between signal and background. There should not be considerable correlations between parameters. Let's take a look at a 1-D example (SEED4 DIP). See Table 4.4.

- Take an event parameter (*e.g.* **DIP**) that discriminates between signal and background.
- Divide the data into several (*e.g.* 5) exclusive ranges.
- Calculate the signal and background fractions in each range after a reasonable set of preliminary cuts.
- Define signal to background ratio in each range as it's FOM.

DIP (μm)	<10	10-15	15-20	20-30	30-60
SGNL	0.239	0.239	0.195	0.238	0.089
BKGR	0.116	0.130	0.101	0.232	0.420
FOM	2.061	1.832	1.922	1.024	0.213

Table 4.4: FOM with one parameter (SEED4 DIP)

These fractions add up to one, and they comprise a set of conditional probabilities [20]. For this reason, we call these signal and background fractions SPROBs and BPROBs respectively.

Extension of this idea to two or more parameters is simple as long as the parameters do not show significant correlations. In such a case, the SPROB, BPROB, and FOM of a multi-dimensional cell of the parameter space will be the product of the corresponding values in corresponding ranges of each parameter we pick for defining FOM. The importance of FOM lies in the fact that it makes it possible to identify the best regions in the parameter space using only one variable.

4.5.1 Optimizing Sensitivity

The introduction of FOM provides a new way of optimizing the sensitivity of searches for decay modes with a relatively powerful technique with considerable

ease. Determining systematic uncertainty due to differences between Monte Carlo simulations and real data can be relatively straight forward.

Predicting Signal and Background Fractions and Dividing Parametric Space into FOM Ranges.

Let us consider a 2-D example with SEED4 DIP and CVK1⁶ (Table 4.5).

- Calculate the signal and background fractions and FOM for each cell in parametric space by taking the corresponding products. Signal and background fractions thus obtained are the *predicted signal and background* in that cell.
- Pick all the cells, the FOM of which falls within the range of interest.
- Add signal and background fractions in each selected cell separately to get the total signal and background fractions in the FOM range. For instance the signal fraction corresponding to the range $1.5 < FOM < 2.0 = 0.029 + 0.029 + 0.023 + 0.162 + 0.004 + 0.003 = 0.250$ [cells (3,1), (3,2), (3,3), (4,4), (5,2) and (5,3) in Table 4.5].

Note that an exclusive set of cells with relatively high signal-to-background ratio is selected with a single cut on FOM, as opposed to a single cell with a set of cuts, in conventional approach.

⁶K1 and K2 are the K's with equal sign and K3 is the one with opposite sign. K1 is the kaon that comes first in the track list before K2.

		DIP (μm)				
		< 10	10 - 15	15 - 20	20 - 30	30 - 60
CVK1	SGNL	0.239	0.239	0.195	0.238	0.089
	BKGR	0.116	0.130	0.101	0.232	0.420
	FOM	2.061	1.832	1.922	1.024	0.213
0.2 - 0.4	0.095	0.023	0.023	0.019	0.023	0.009
	0.314	0.036	0.041	0.032	0.073	0.132
	0.303	0.625	0.556	0.583	0.311	0.065
0.4 - 0.6	0.087	0.021	0.021	0.017	0.021	0.008
	0.129	0.015	0.017	0.013	0.030	0.054
	0.673	1.387	1.233	1.293	0.689	0.143
0.6 - 0.7	0.120	0.029	0.029	0.023	0.029	0.011
	0.129	0.015	0.017	0.013	0.030	0.054
	0.935	1.928	1.714	1.798	0.958	0.199
0.7 - 0.8	0.683	0.163	0.163	0.133	0.162	0.061
	0.414	0.048	0.054	0.042	0.096	0.174
	1.649	3.400	3.022	3.170	1.690	0.351
0.8 - 1.0	0.015	0.004	0.004	0.003	0.003	0.001
	0.014	0.002	0.002	0.001	0.003	0.006
	1.026	2.116	1.881	1.973	1.051	0.218

Table 4.5: SPROBs, BPROBs, and FOM for DIP (row 3 - 5), CVK1 (column 2), and DIP and CVK1 space (from row 6 and column 3).

Optimal FOM Cut that gives the Best Sensitivity

When doing a blind analysis (section 4.1), it is necessary to optimize the cuts before looking at the data in the signal region to keep oneself from being biased. Since FOM is a derived variable that includes signal-background discriminatory information of a set of event parameters, optimizing the cut on FOM will in turn optimize the cuts on the set of parameters we use to define FOM.

To find the FOM cut that maximizes the sensitivity, one predicts signal (S) and background (B) for a series of FOM cuts and plots (or makes tables of) sensitivity: $S/\sqrt{S+B}$ (or S/\sqrt{B} depending on the circumstances.) vs. FOM and finds the maximum, and hence the optimal FOM cut.

4.5.2 Event Parameters Selected

After studying the signal and background distributions of the event parameters, a set of parameters was selected to form the FOM. The event parameters selected for FOM showed a moderate variation of sensitivity with the cut. They did not show any correlations among each other. For SEED4, CVK1, CVK2, CVK3, DIP and COSSP were selected. For SEED3, MRAT was included along with this set. The parameters that were not selected for FOM either did not show moderate variation of sensitivity with the cut or did show correlations with the other parameters in the FOM.

Correlations between these parameters were studied carefully. Each pair of parameters was considered. The average value of one parameter was calculated for a set of ranges of the other for background subtracted signal. Only parameters that did not show any systematic variation (only those which fluctuated within statistical errors) were selected to form the FOM⁷.

In constructing FOM, background fractions were always calculated with $KKK\pi$ real data. Signal fractions of COSSP and MRAT (SEED3 only) were calculated with $KKK\pi$ Monte Carlo data. Comparison of Monte Carlo and real data signal distributions of $K\pi\pi\pi$ indicates slight systematic differences between the two CVK and DIP distributions. For this reason, CVK and DIP signal fractions that were used in the FOM were not calculated solely from $KKK\pi$ Monte Carlo data. For these variables: CVK1, CVK2, CVK3, and DIP the signal fractions were separately calculated from $KKK\pi$ Monte Carlo data and $K\pi\pi\pi$ real data. The average of the two set was then used in constructing the FOM.

Table 4.6 - 4.10 show the ranges, SPROBs, BPROBs and FOM — taking only that particular parameter into consideration — of the SEED4 FOM constituent parameters: CVK1, CVK2, CVK3, DIP, and COSSP.

⁷When selecting the parameters for FOM, care was taken to intuitively choose parameters that would not be correlated. *e.g.* PTBL was thought to correlate with DIP and thus it was not chosen. None of the parameters thus selected correlated with any other.

CVK1 Range	.2-.4	.4-.6	.6-.7	.7-.8	.8-1.
MC $3K\pi$ SGNL	0.095	0.087	0.120	0.683	0.015
RD $K3\pi$ SGNL	0.143	0.121	0.121	0.538	0.077
Average SGNL	0.119	0.104	0.120	0.611	0.046
RD $3K\pi$ BKGR	0.314	0.129	0.129	0.414	0.014
FOM (with MC S)	0.303	0.673	0.935	1.649	1.026
FOM (with RD S)	0.456	0.944	0.938	1.299	5.361
FOM (with AV S)	0.380	0.809	0.937	1.474	3.194

Table 4.6: SEED4 FOM from CVK1 alone along with the CVK1 ranges and CVK1 SPROBs and BPROBs used in SEED4 FOM. Signal fractions have been calculated using both $KKK\pi$ Monte Carlo data and $K\pi\pi\pi$ real data. The average signal fractions have been used in constructing the FOM.

CVK2 Range	.2-.4	.4-.6	.6-.7	.7-.8	.8-1.
MC $3K\pi$ SGNL	0.095	0.094	0.147	0.652	0.012
RD $K3\pi$ SGNL	0.143	0.121	0.121	0.538	0.077
Average SGNL	0.119	0.108	0.134	0.595	0.044
RD $3K\pi$ BKGR	0.400	0.157	0.129	0.300	0.014
FOM (with MC S)	0.238	0.597	1.140	2.175	0.821
FOM (with RD S)	0.358	0.772	0.938	1.794	5.361
FOM (with AV S)	0.298	0.685	1.039	1.984	3.091

Table 4.7: SEED4 FOM from CVK2 alone along with the CVK2 ranges and CVK2 SPROBs and BPROBs used in SEED4 FOM. Signal fractions have been calculated using both $KKK\pi$ Monte Carlo data and $K\pi\pi\pi$ real data. The average signal fractions have been used in constructing the FOM.

CVK3 Range	.2-.4	.4-.6	.6-.7	.7-.8	.8-1.
MC $3K\pi$ SGNL	0.101	0.125	0.117	0.651	0.006
RD $K3\pi$ SGNL	0.143	0.121	0.121	0.538	0.077
Average SGNL	0.122	0.123	0.119	0.595	0.041
RD $3K\pi$ BKGR	0.300	0.157	0.129	0.400	0.014
FOM (with MC S)	0.337	0.793	0.912	1.628	0.411
FOM (with RD S)	0.477	0.772	0.938	1.345	5.361
FOM (with AV S)	0.407	0.783	0.925	1.487	2.886

Table 4.8: SEED4 FOM from CVK3 alone along with the CVK3 ranges and CVK3 SPROBs and BPROBs used in SEED4 FOM. Signal fractions have been calculated using both $KKK\pi$ Monte Carlo data and $K\pi\pi\pi$ real data. The average signal fractions have been used in constructing the FOM.

DIP Range (μm)	< 10	10-15	15-20	20-30	30-60
MC $3K\pi$ SGNL	0.239	0.239	0.195	0.238	0.089
RD $K3\pi$ SGNL	0.259	0.224	0.193	0.226	0.098
Average SGNL	0.249	0.232	0.194	0.232	0.094
RD $3K\pi$ BKGR	0.116	0.130	0.101	0.232	0.420
FOM (with MC S)	2.061	1.832	1.922	1.024	0.213
FOM (with RD S)	2.233	1.721	1.904	0.974	0.232
FOM (with AV S)	2.147	1.777	1.913	0.999	0.223

Table 4.9: SEED4 FOM from DIP alone along with the DIP ranges and DIP SPROBs and BPROBs used in SEED4 FOM. Signal fractions have been calculated using both $KKK\pi$ Monte Carlo data and $K\pi\pi\pi$ real data. The average signal fractions have been used in constructing the FOM.

COSSP Range	.0-.2	.2-.4	.4-.6	.6-.8	.8-1.
MC $3K\pi$ SGNL	0.273	0.284	0.254	0.114	0.075
RD $3K\pi$ BKGR	0.203	0.145	0.217	0.188	0.246
FOM (with MC S)	1.344	1.963	1.167	0.607	0.304

Table 4.10: SEED4 FOM from COSSP alone along with the COSSP ranges and COSSP SPROBs and BPROBs used in SEED4 FOM.

Table 4.11 - 4.16 show the ranges, SPROBs, BPROBs and FOM — taking only that particular parameter into consideration — of the SEED3 FOM constituent parameters: CVK1, CVK2, CVK3, DIP, MRAT and COSSP.

CVK1 Range	.2-.4	.4-.6	.6-.7	.7-.8	.8-1.
MC $3K\pi$ SGNL	0.072	0.103	0.117	0.692	0.016
RD $K3\pi$ SGNL	0.139	0.117	0.113	0.558	0.073
Average SGNL	0.105	0.110	0.115	0.625	0.045
RD $3K\pi$ BKGR	0.328	0.216	0.104	0.344	0.008
FOM (with MC S)	0.220	0.478	1.124	2.010	2.038
FOM (with RD S)	0.422	0.543	1.090	1.621	9.163
FOM (with AV S)	0.321	0.511	1.107	1.816	5.600

Table 4.11: SEED3 FOM from CVK1 alone along with the CVK1 ranges and CVK1 SPROBs and BPROBs used in SEED3 FOM. Signal fractions have been calculated using both $KKK\pi$ Monte Carlo data and $K\pi\pi\pi$ real data. The average signal fractions have been used in constructing the FOM.

CVK2 Range	.2-.4	.4-.6	.6-.7	.7-.8	.8-1.
MC $3K\pi$ SGNL	0.109	0.095	0.096	0.675	0.024
RD $K3\pi$ SGNL	0.139	0.117	0.113	0.558	0.073
Average SGNL	0.124	0.106	0.105	0.616	0.049
RD $3K\pi$ BKGR	0.344	0.184	0.128	0.336	0.008
FOM (with MC S)	0.316	0.517	0.754	2.010	3.057
FOM (with RD S)	0.403	0.638	0.885	1.659	9.163
FOM (with AV S)	0.359	0.577	0.819	1.835	6.110

Table 4.12: SEED3 FOM from CVK2 alone along with the CVK2 ranges and CVK2 SPROBs and BPROBs used in SEED3 FOM. Signal fractions have been calculated using both $KKK\pi$ Monte Carlo data and $K\pi\pi\pi$ real data. The average signal fractions have been used in constructing the FOM.

CVK3 Range	.2-.4	.4-.6	.6-.7	.7-.8	.8-1.
MC $3K\pi$ SGNL	0.080	0.106	0.101	0.700	0.014
RD $K3\pi$ SGNL	0.139	0.117	0.113	0.558	0.073
Average SGNL	0.109	0.112	0.107	0.629	0.043
RD $3K\pi$ BKGR	0.331	0.129	0.153	0.371	0.016
FOM (with MC S)	0.242	0.821	0.656	1.886	0.842
FOM (with RD S)	0.419	0.909	0.740	1.503	4.545
FOM (with AV S)	0.331	0.865	0.698	1.695	2.694

Table 4.13: SEED3 FOM from CVK3 alone along with the CVK3 ranges and CVK3 SPROBs and BPROBs used in SEED3 FOM. Signal fractions have been calculated using both $KKK\pi$ Monte Carlo data and $K\pi\pi\pi$ real data. The average signal fractions have been used in constructing the FOM.

DIP Range (μm)	< 10	10-15	15-20	20-30	30-60
MC $3K\pi$ SGNL	0.260	0.178	0.209	0.235	0.118
RD $K3\pi$ SGNL	0.226	0.199	0.201	0.250	0.125
Average SGNL	0.243	0.188	0.205	0.242	0.122
RD $3K\pi$ BKGR	0.065	0.097	0.113	0.234	0.492
FOM (with MC S)	4.022	1.839	1.853	1.005	0.240
FOM (with RD S)	3.504	2.052	1.780	1.067	0.254
FOM (with AV S)	3.763	1.946	1.817	1.036	0.247

Table 4.14: SEED3 FOM from DIP alone along with the DIP ranges and DIP SPROBs and BPROBs used in SEED3 FOM. Signal fractions have been calculated using both $KKK\pi$ Monte Carlo data and $K\pi\pi\pi$ real data. The average signal fractions have been used in constructing the FOM.

MRAT Range	.0-.2	.2-.4	.4-.6	.6-.8	.8-1.
MC $3K\pi$ SGNL	0.120	0.351	0.295	0.159	0.076
RD $3K\pi$ BKGR	0.161	0.194	0.226	0.290	0.129
FOM (with MC S)	0.741	1.811	1.306	0.548	0.590

Table 4.15: SEED3 FOM from COSSP alone along with the COSSP ranges and COSSP SPROBs and BPROBs used in SEED4 FOM.

COSSP Range	.0-.2	.2-.4	.4-.6	.6-.8	.8-1.
MC $3K\pi$ SGNL	0.327	0.273	0.220	0.109	0.071
RD $3K\pi$ BKGR	0.258	0.298	0.194	0.129	0.121
FOM (with MC S)	1.269	0.915	1.137	0.842	0.584

Table 4.16: SEED3 FOM from COSSP alone along with the COSSP ranges and COSSP SPROBs and BPROBs used in SEED4 FOM.

4.5.3 Signal and Background Discrimination

Figs. 4.20 and 4.21 show the distributions of the parameter CVK1, CVK2, CVK3, DIP, and COSSP that were used in constructing FOM, for SEED4 $KKK\pi$ Monte Carlo signal and real data background events. The tuned cuts before FOM (section 4.4) have been applied to the data sample. The plots on the left show the distributions of the events that passed an FOM cut at .5, and those on right show the distributions of those that failed. The distribution of a particular variable that represents the events that passed the cut has been normalized to unity along with its counterpart that represents the failed events (i.e. the sum of areas under the “passed” and “failed” distributions amounts to unity.). Note that the vertical scales of the adjacent plots are not the same. These plots illustrate how FOM eliminates background events without losing many signal events; only a small fraction of the signal events is lost. Figs. 4.22 and 4.23 show similar plots that were made for SEED3 events with an FOM cut at 1. These plots include the distributions of MRAT which were not there in SEED4.

Fig. 4.24 shows FOM distributions for SEED4 (left) and SEED3 (right) $KKK\pi$ Monte Carlo signal and real data background events. Though they have the same name, SEED3 FOM is different from SEED4 FOM; the former has MRAT in its

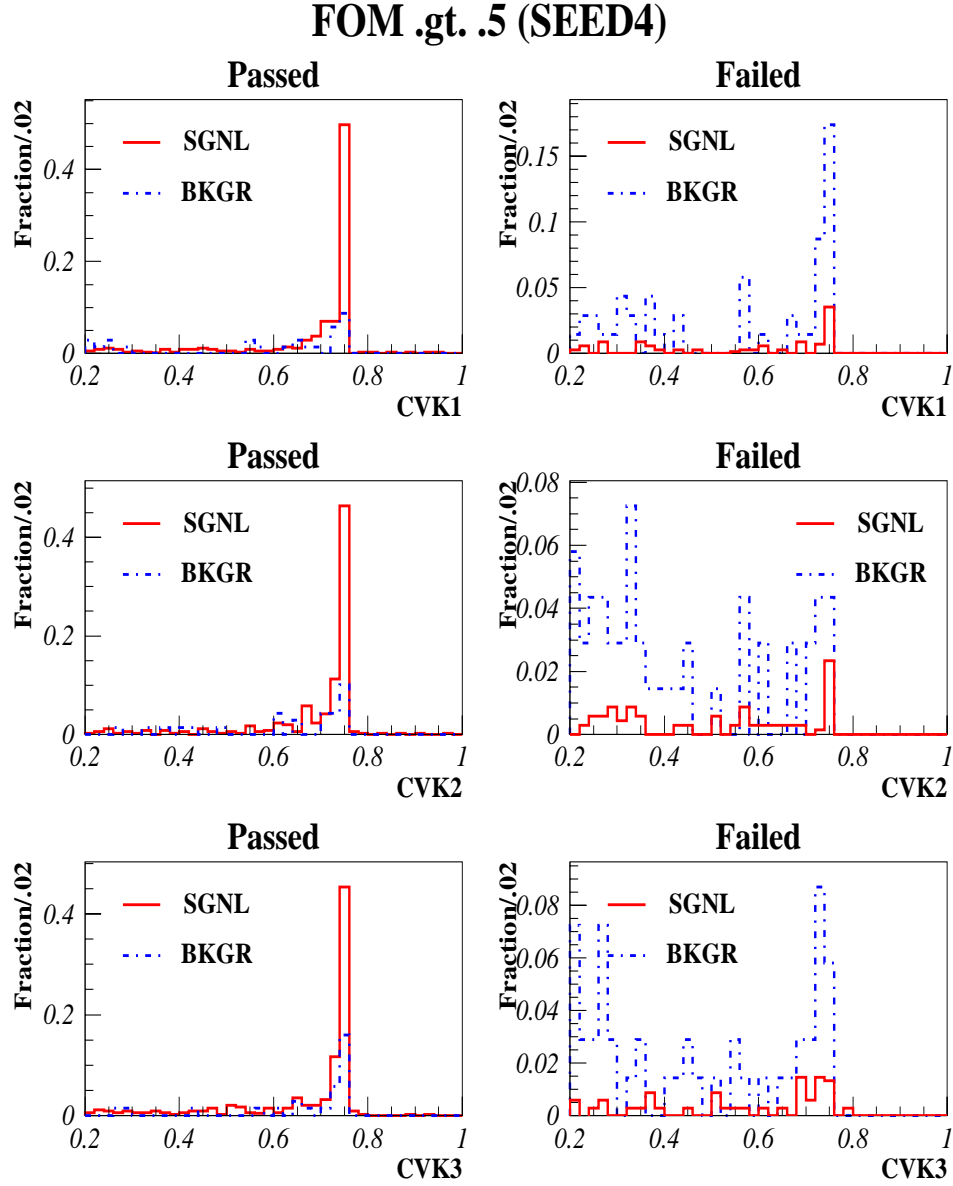


Figure 4.20: SEED4 $KKK\pi$ CVK Monte Carlo signal and real data background distributions of the events that pass (left) and fail (right) an FOM cut at .5.

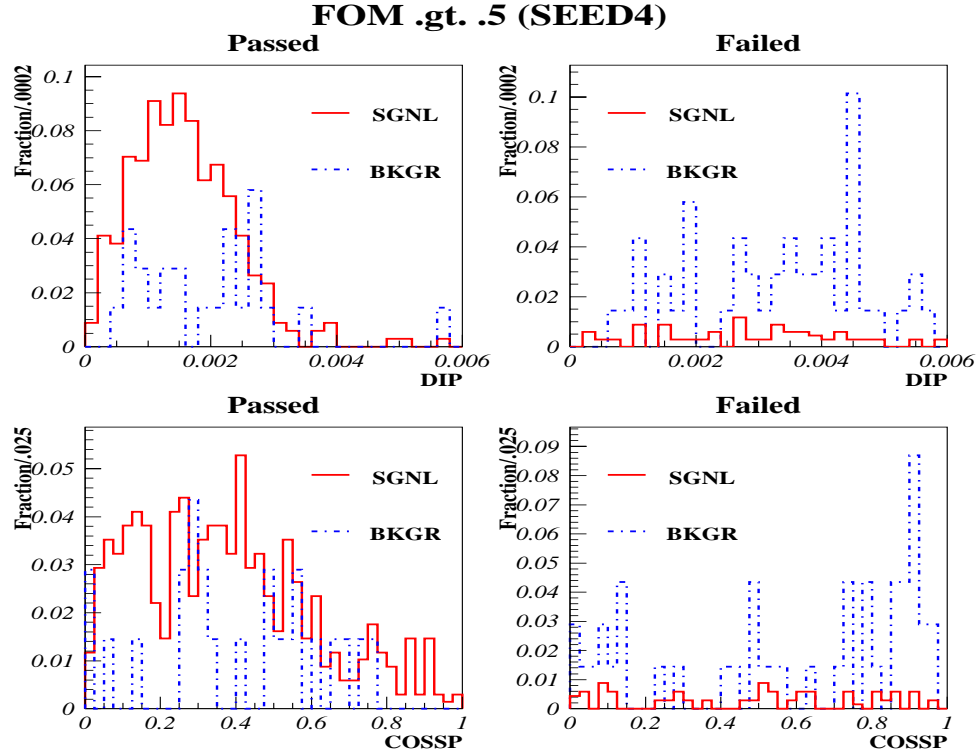


Figure 4.21: SEED4 $KKK\pi$ DIP (upper) and COSSP (lower) Monte Carlo signal and real data background distributions of the events that pass (left) and fail (right) an FOM cut at .5.

construction, but the latter does not. Most importantly, the signal and background distributions for SEED4 and SEED3 differ considerably. There are events beyond $\text{FOM} = 4$; only the region where the FOM cut is most probable has been shown. The cuts described in Table 4.26 (except the FOM cut) have already been applied. Each distribution has been normalized to unity and plotted on a semilog scale. The plots in Fig. 4.24 and the Tables 4.19 - 4.25 in section 4.6 were used to determine the FOM cuts for the SEED4 and SEED3 data samples.

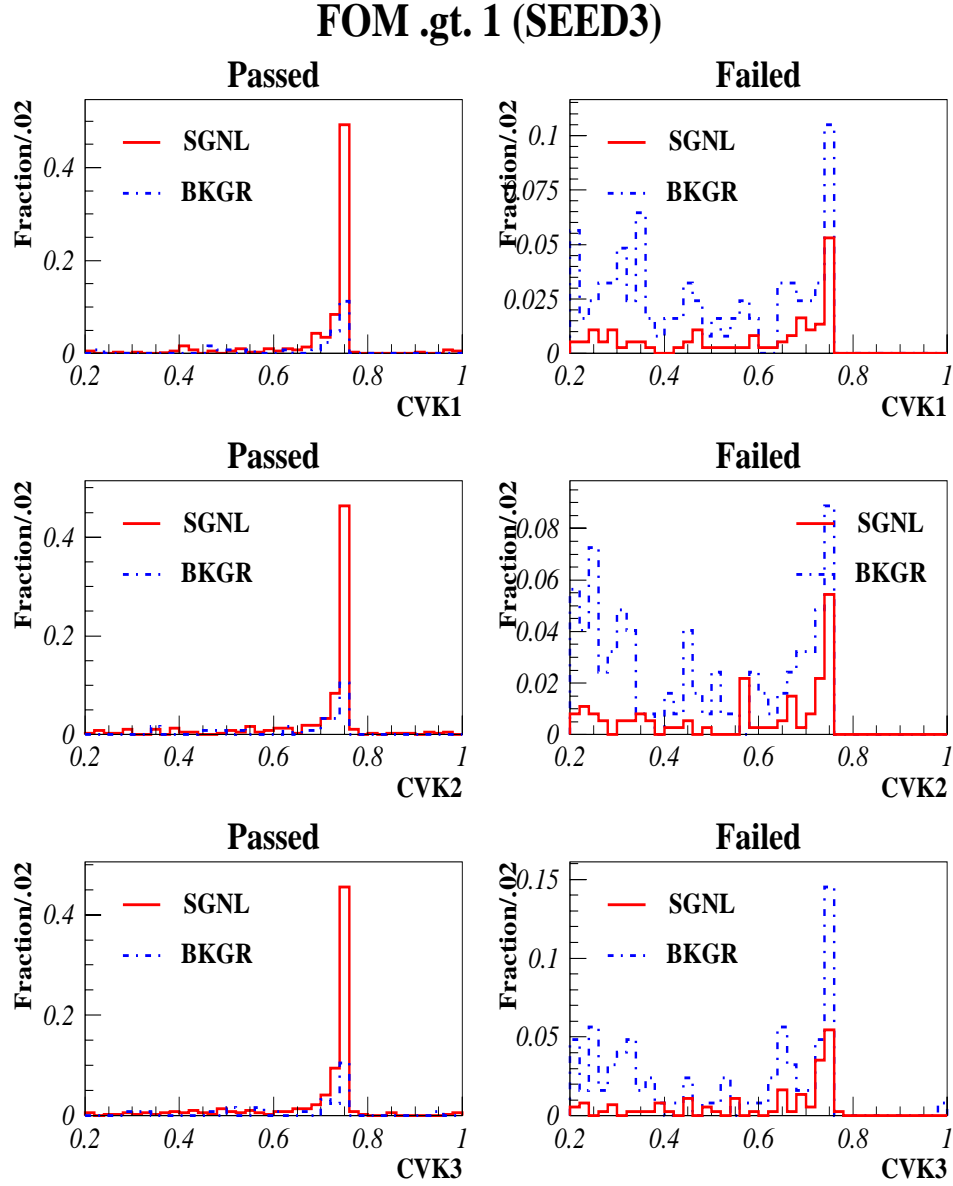


Figure 4.22: SEED3 $KKK\pi$ CVK Monte Carlo signal and real data background distributions of the events that pass (left) and fail (right) an FOM cut at 1.

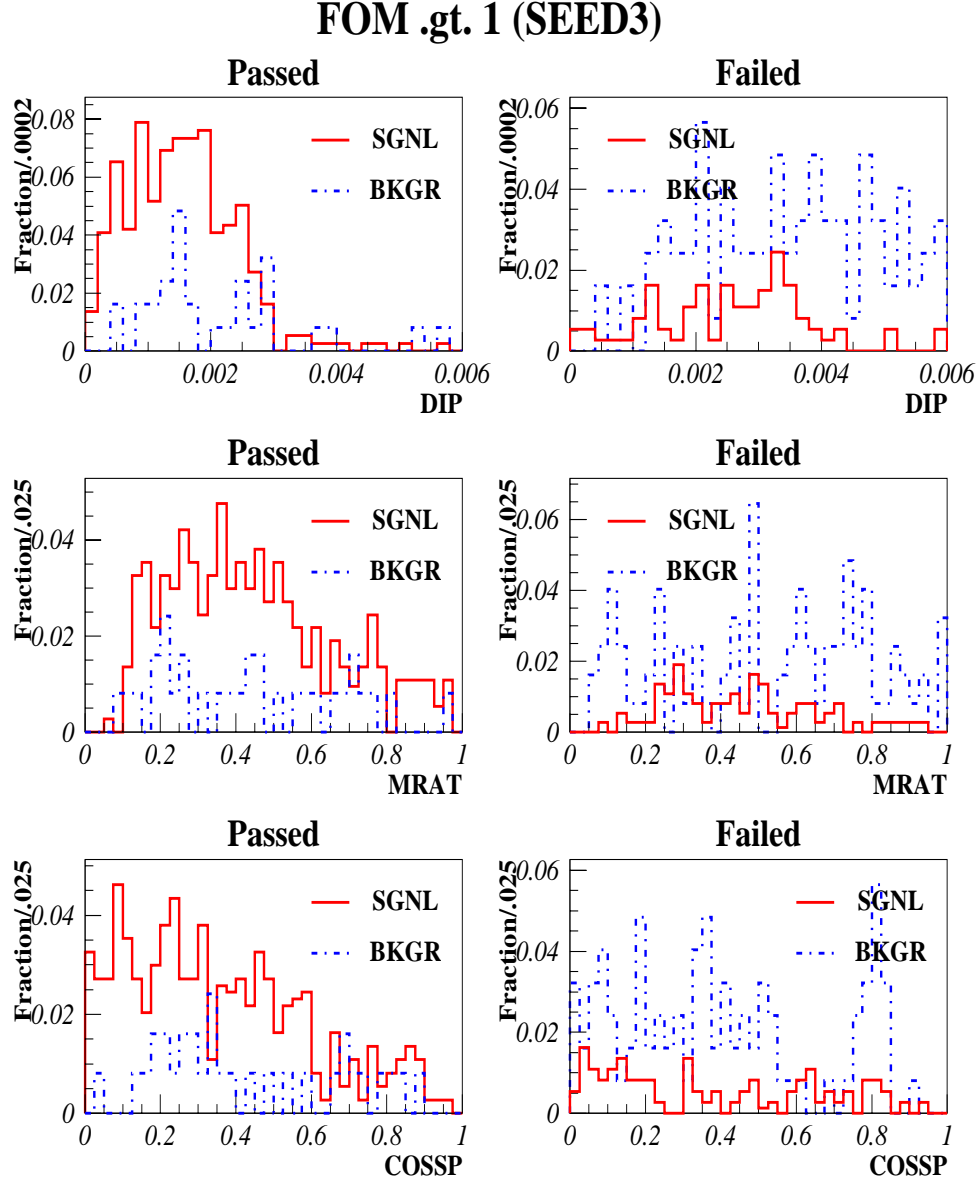


Figure 4.23: SEED3 $KKK\pi$ DIP (upper), MRAT (middle), and COSSP (lower) Monte Carlo signal and real data background distributions of the events that pass (left) and fail (right) an FOM cut at 1.

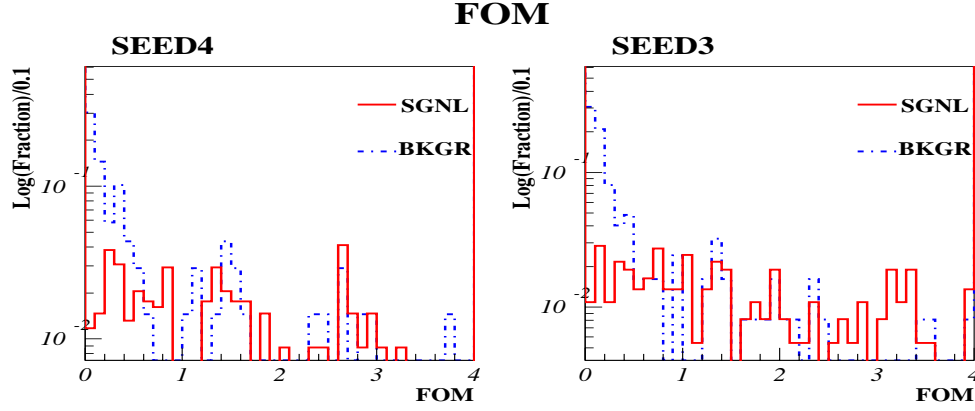


Figure 4.24: SEED4 (left) and SEED3 (right) $KKK\pi$ FOM Monte Carlo signal and real data background distributions on semilog plots. The overall cuts applied to SEED4 and SEED3 data samples are the tuned SEED4 and SEED3 cuts before FOM respectively. There are events beyond FOM = 4; only the region where the FOM cut is most probable has been shown.

4.5.4 Systematic Uncertainty due to Correlations

The systematic uncertainty due to possible correlation in the parameters in FOM was determined by estimating the number of Monte Carlo signal events that survive the FOM cut in two ways and comparing the results. In one case, the calculation was done in the multidimensional parameter space (5-D for SEED4 and 6-D for SEED3) which will be referred to as the FOM space. Each dimension corresponds to one parameter used in FOM. The division of these parameters into exclusive ranges defines a multidimensional grid in this FOM space. Picking one range from each parameter defines a FOM cell in the FOM grid. The number of cells in this grid is given by the product of number of ranges that each parameter has been divided into.

The procedure for estimating the number of signal and background events that survive the FOM cut, “S(cell)” and “B(cell)” respectively, in this way is as follows.

- Take the first cell that corresponds to the first range of all the parameters and calculate SPROB, BPROB and FOM of that cell by multiplying SPROB, BPROB and FOM of the corresponding ranges of each parameter.
- Repeat this calculation all through the grid for all the cells.
- For each FOM cut pick up and add all the SPROBs in all the cells that have FOM greater than the FOM cut. This is what is labeled as “S(cell)”.
- Do the same for BPROBs. This is what is labeled as “B(cell)”.

In the second method, the signal fraction is calculated by making the Monte Carlo $KKK\pi$ mass histograms with the same set of FOM cuts, as was used in calculating “S(cell)”, and fitting the histograms. The signal fraction thus obtained is labeled as “S(plot)”. Similarly, the background fraction is obtained from real data $KKK\pi$ background histograms with the same set of FOM cuts. This is labeled as “B(plot)”. Systematic uncertainties in signal estimates, due to correlations between the parameters in FOM, have been estimated as half the difference in “S(cell)” and “S(plot)”. The same procedure was adopted for calculating the systematic uncertainty of background estimates. The systematic errors for background estimates were

FOM Cut	S (cell)	S (plot)	ΔS_{sys}	B (cell)	B (plot)	ΔB_{sys}
0.0	100%	100%	0.0%	100%	100%	0.0%
0.1	99%	99%	0.0%	74%	70%	2.0%
0.2	97%	97%	0.0%	58%	55%	1.5%
0.3	95%	93%	1.0%	50%	49%	0.5%
0.5	90%	88%	1.0%	38%	35%	1.5%
1.0	80%	80%	0.0%	24%	30%	3.0%
1.5	71%	72%	0.5%	17%	20%	1.5%
2.0	63%	66%	1.5%	13%	16%	1.5%

Table 4.17: SEED4 signal and background fractions calculated directly from the FOM grid, “S (cell)” and “B (cell)” respectively, signal fractions from $KKK\pi$ Monte Carlo plots, “S (plot)”, background fractions from $KKK\pi$ real data histograms, “B (plot)” and the estimated systematic uncertainty associated with signal and background estimates due to parameter correlations in FOM, ΔS_{sys} and ΔB_{sys} respectively.

calculated only to study the correlations. Tables 4.17 and 4.18 shows these results obtained for SEED4 and SEED3 respectively.

4.6 Optimizing the FOM Cut

To optimize the FOM cut, the expected number of $KKK\pi$ signal and background events were estimated for a series of FOM cuts. Different cut combinations — one FOM cut on SEED4 data and another on SEED3 data — were tried. The expected number of $KKK\pi$ signal events was estimated from $KKK\pi$ Monte Carlo data and that of $KKK\pi$ background events came directly from the $KKK\pi$ real data.

FOM Cut	S (cell)	S (plot)	ΔS_{sys}	B (cell)	B (plot)	ΔB_{sys}
0.0	100%	100%	0.0%	100%	100%	0.0%
0.2	96%	96%	0.0%	54%	48%	3.0%
0.4	92%	93%	0.5%	39%	36%	1.5%
0.5	90%	91%	0.5%	34%	31%	1.5%
0.6	88%	90%	1.0%	30%	30%	0.0%
0.8	84%	85%	0.5%	25%	27%	1.0%
1.0	80%	82%	1.0%	21%	24%	1.5%
1.2	78%	80%	1.0%	18%	24%	3.0%
1.5	73%	74%	0.5%	15%	18%	1.5%
1.7	71%	73%	1.0%	14%	17%	1.5%
2.0	67%	69%	1.0%	12%	14%	1.0%

Table 4.18: SEED3 signal and background fractions calculated directly from the FOM grid, “S (cell)” and “B (cell)” respectively, signal fractions from $KKK\pi$ Monte Carlo plots, “S (plot)”, background fractions from $KKK\pi$ real data histograms, “B (plot)” and the estimated systematic uncertainty associated with signal and background estimates due to parameter correlations in FOM, ΔS_{sys} and ΔB_{sys} respectively.

4.6.1 Estimating the Expected Number of Signal Events

The expected number of $KKK\pi$ signal events was estimated using the equation:

$$[S_{RD_{KKK\pi}}]_{EX} = \left[\frac{\Gamma_{KKK\pi}}{\Gamma_{K\pi\pi\pi}} \right]_{E687} \times S_{RD_{K\pi\pi\pi}} \times \frac{S_{MC_{KKK\pi}}}{S_{MC_{K\pi\pi\pi}}}$$

where $\left[\frac{\Gamma_{KKK\pi}}{\Gamma_{K\pi\pi\pi}} \right]_{E687}$ is the $KKK\pi$ branching fraction relative to the $K\pi\pi\pi$ normalization channel from Fermilab experiment E687 [7] and $S_{MC_{KKK\pi}}$ is the number of Monte

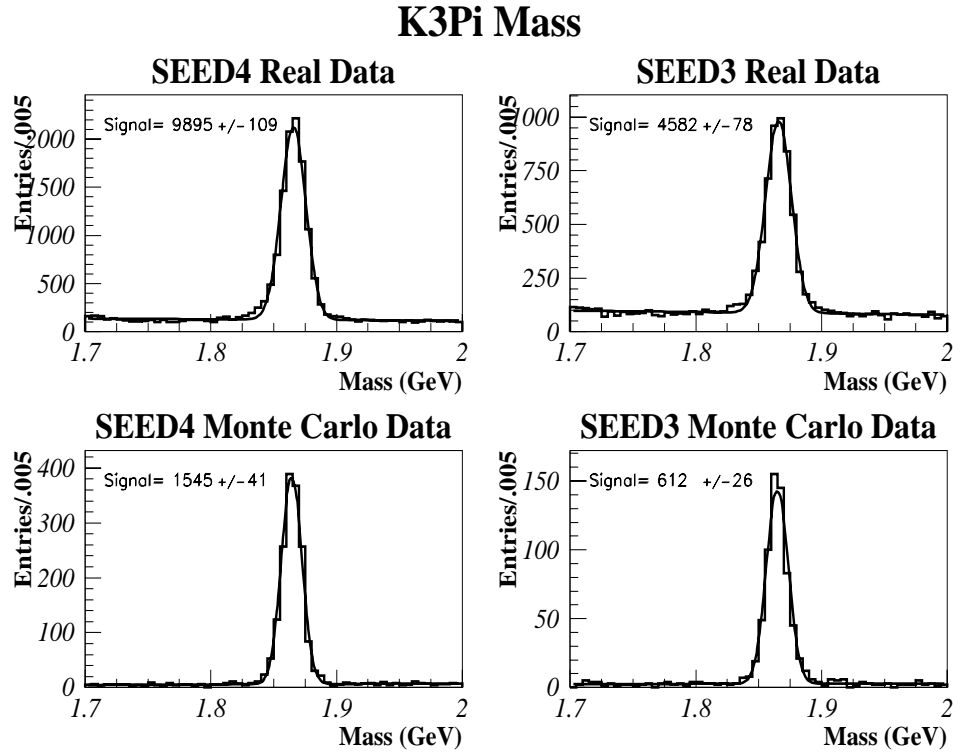


Figure 4.25: Mass histograms for $K\pi\pi\pi$ real (top) and Monte Carlo (bottom) data. At left are SEED4 and at right are SEED3 plots. Besides the cuts $SDZT > 2$ and $SDCA > 4$, the cuts are the same as $KKK\pi$ tuned cuts before FOM.

Carlo $KKK\pi$ signal events, obtained from a $KKK\pi$ mass fit, with the tuned cuts before FOM, and the particular FOM cut we are looking at. $S_{MC_{K\pi\pi\pi}}$ and $S_{RD_{K\pi\pi\pi}}$ are the number of Monte Carlo and real data $K\pi\pi\pi$ signal events obtained from $K\pi\pi\pi$ mass fits made with a set of cuts similar to the $KKK\pi$ cuts before FOM (Fig. 4.25). These cuts on $K\pi\pi\pi$ differ from those on $KKK\pi$ only in $SDZT$ and $SDCA$. A cut of $SDZT > 2$ has been applied on the $K\pi\pi\pi$ data sample whereas the cut on SEED4 $KKK\pi$ events is at $SDCA > 1$, and no $SDZT$ cut at all on $KKK\pi$ SEED3 events.

The SDCA cut on $K\pi\pi\pi$ data sample is at $\text{SDCA} > 4$, but no SDCA cut has been applied on $KKK\pi$ events.

The first two terms of this formula, $[\frac{\Gamma_{KKK\pi}}{\Gamma_{K\pi\pi\pi}}]_{E687} \times S_{RD_{K\pi\pi\pi}}$, give the expected number of $KKK\pi$ signal events before correcting for the detector and the reconstruction efficiencies. $KKK\pi$ and $K\pi\pi\pi$ decays have different detector and reconstruction efficiencies. The third term $\frac{S_{MC_{KKK\pi}}}{S_{MC_{K\pi\pi\pi}}}$ corrects for this difference in efficiencies. With this recipe and the number of Monte Carlo and real data $K\pi\pi\pi$ signal events, 1545 ± 41 and 9895 ± 109 respectively, the formula to convert the number of SEED4 $KKK\pi$ Monte Carlo signal events to the expected number of SEED4 $KKK\pi$ real data signal events takes the form:

$$\begin{aligned} [S_{RD_{KKK\pi}}]_{EX} &= 0.0028 \times 9895 \times \frac{S_{MC_{KKK\pi}}}{1545} \\ &= 0.0179 \times S_{MC_{KKK\pi}} \end{aligned}$$

and similarly for SEED3, with $S_{MC_{K\pi\pi\pi}} = 612 \pm 26$ and $S_{RD_{K\pi\pi\pi}} = 4582 \pm 78$, the formula reads

$$\begin{aligned} [S_{RD_{KKK\pi}}]_{EX} &= 0.0028 \times 4582 \times \frac{S_{MC_{KKK\pi}}}{612} \\ &= 0.0210 \times S_{MC_{KKK\pi}} \quad . \end{aligned}$$

These two formulae have been used to estimate the expected number of $KKK\pi$ signal events given in Tables 4.19 - 4.25.

4.6.2 Estimating the Expected Number of Background Events

The background under the signal was estimated assuming a linear background and a signal that spans 15 MeV (3 bin). The width of each bin in the mass histograms is 5 MeV, the total number of bins in the histogram is 60 and the width of the blind window is ± 20 MeV; thus, three times the average number of background events per bin was taken as the number of background events under the signal. These numbers come down to a scaling factor of $3/(60 - 2 \times 4) = 0.0577$ in calculating the number of background events under the signal from the number of background events outside the blind window. This scaling factor has been used to estimate the expected number of $KKK\pi$ background events given in the Tables 4.19 - 4.25. This background estimate was used only for optimizing sensitivity; a more sophisticated technique was used to estimate the background under the signal when the $KKK\pi$ mass window was opened.

4.6.3 The Three Types of FOM

When optimizing the FOM cut, three types of FOMs were tried. The first FOM had all SPROBs and BPROBs calculated solely from $KKK\pi$ Monte Carlo data. But, DIP and CVK distributions of $K\pi\pi\pi$ Monte Carlo data showed some systematic deviation from the $K\pi\pi\pi$ real data. Based on this, one may expect to see a similar discrepancy also in $KKK\pi$ Monte Carlo and real data. To make a correction

to this, DIP and CVK distributions of $K\pi\pi\pi$ data were directly used to define DIP and CVK SPROBs and BPROBs. The MRAT (SEED3 only) and COSSP SPROBs and BPROBs were still taken from $KKK\pi$ Monte Carlo data. This was the second type of FOM that was tried. In the third type, the average SPROBs and BPROBs of the first two types were used to define FOM.

One may consider the first two types as two extremes: in one case the decay mode is the same, but data are simulated; in the other case the data are all real, but the decay mode is not $KKK\pi$. The third type, which used the average SPROBs and BPROBs of the first two, may be seen as a good compromise between the first two extremes and the third FOM type was used in the analysis. However, the systematic variation in the expected number of $KKK\pi$ signal events due to these differences is less than 1%. Section 4.5.2 lists the SPROBs and BPROBs of all three types of FOM.

4.6.4 Selecting the Optimal FOM Cut

Tables 4.19 and 4.20 show the estimated expected number of signal events and background events for a set of FOM cuts, for SEED4 and SEED3 data samples respectively. The tables also show S/B , S/\sqrt{B} , and $S/\sqrt{S+B}$ for each FOM cut. Tables 4.21 - 4.25 show these estimates for a series of SEED4 and SEED3 FOM cut combinations. These tables were used to find the optimal FOM cuts for SEED4 and SEED3 data samples. In doing so, a few points were kept in mind;

FOM	Signal		Background (Data)		$\frac{S}{B}$	$\frac{S}{\sqrt{B}}$	$\frac{S}{\sqrt{S+B}}$
	Monte Carlo	Estimated S	Outside the Signal	Under the Sgnl (Est. B)			
0.0	339	6.1	69	4.0	1.5	3.0	1.9
0.1	334	6.0	48	2.8	2.2	3.6	2.0
0.2	328	5.9	38	2.2	2.7	4.0	2.1
0.3	316	5.7	34	2.0	2.9	4.0	2.0
0.5	299	5.4	24	1.4	3.9	4.6	2.1
1.0	270	4.8	21	1.2	4.0	4.4	2.0
1.5	245	4.4	14	0.8	5.4	4.9	1.9
2.0	224	4.0	11	0.6	6.3	5.0	1.9

Table 4.19: Expected number of SEED4 $KKK\pi$ signal and background events for various SEED4 FOM cuts. The background estimates assume linear background and 15 MeV signal region.

- $S/\sqrt{S+B}$ should be high and it should be given the highest priority unless other factors are significantly affected. This gives a high statistical significance to the final result.
- When there is more than one set of SEED4 and SEED3 FOM cuts with the same $S/\sqrt{S+B}$, S/\sqrt{B} should be used as a tie breaker.
- S/B should not be too low. This ensures that we get a clean signal.

FOM	Signal		Background (Data)		$\frac{S}{B}$	$\frac{S}{\sqrt{B}}$	$\frac{S}{\sqrt{S+B}}$
	Monte Carlo	Estimated S	Outside the Signal	Under the Sgnl (Est. B)			
0.0	357	7.5	124	7.2	1.0	2.8	2.0
0.2	343	7.2	60	3.5	2.1	3.9	2.2
0.4	331	6.9	45	2.6	2.7	4.3	2.2
0.5	325	6.8	39	2.2	3.0	4.5	2.3
0.6	320	6.7	37	2.1	3.1	4.6	2.3
0.8	304	6.4	33	1.9	3.4	4.6	2.2
1.0	295	6.2	30	1.7	3.6	4.7	2.2
1.2	284	6.0	30	1.7	3.4	4.5	2.1
1.5	264	5.5	22	1.3	4.4	4.9	2.1
1.7	261	5.5	21	1.2	4.5	5.0	2.1
2.0	248	5.2	17	1.0	5.3	5.2	2.1

Table 4.20: Expected number of SEED3 $KKK\pi$ signal and background events for various SEED3 FOM cuts. The background estimates assume linear background and 15 MeV signal region.

- SEED4 and SEED3 data sample should have roughly the same S/B . This ensures that the less clean data sample does not deteriorate the cleanliness of the cleaner data sample.
- The FOM cut should not be so tight that it loses too many signal events. This restriction maintains good statistics in the final sample, reducing statistical fluctuations.

FOM		Signal		Background (Data)		$\frac{S}{B}$	$\frac{S}{\sqrt{B}}$	$\frac{S}{\sqrt{S+B}}$
SEED4	SEED3	Monte Carlo	Est. S	In the Wings	Sgnl. Rgn. Est. B			
0.0	0.0	339/357	13.6	193	11.1	1.2	4.1	2.7
0.1	0.2	334/343	13.2	108	6.2	2.1	5.3	3.0
0.1	0.5	334/325	12.8	87	5.0	2.6	5.7	3.0
0.1	0.8	334/304	12.4	81	4.7	2.6	5.7	3.0
0.1	1.0	334/295	12.2	78	4.5	2.7	5.7	3.0
0.1	1.2	334/284	11.9	78	4.5	2.7	5.6	2.9
0.1	1.5	334/264	11.5	70	4.0	2.9	5.7	2.9
0.1	1.7	334/261	11.4	69	4.0	2.9	5.7	2.9
0.1	2.0	334/248	11.2	65	3.8	3.0	5.8	2.9

Table 4.21: Expected number of total (SEED4 and SEED3 combined) $KKK\pi$ signal events and background events for various SEED3 FOM cuts. SEED4 FOM cut has been fixed at FOM > 0.1 . The top row shows the results with no FOM cut at all.

Based on $S/\sqrt{S+B}$, one would choose either SEED4 FOM > 0.2 and SEED3 FOM > 0.5 (Table 4.22) where $S/\sqrt{S+B} = 3.1$ or SEED4 FOM > 0.5 and SEED3 FOM > 0.5 (Table 4.23) where $S/\sqrt{S+B} = 3.1$ again, but the former set of cuts promise only $S/B = 2.9$ (Table 4.22) and the latter set of cuts gives significantly different S/B for SEED4 ($S/B = 3.9$, Table 4.19) and for SEED3 ($S/B = 3.0$, Table 4.20). The decision was to compromise $S/\sqrt{S+B}$ to a lower value which is 3.0.

FOM		Signal		Background (Data)		$\frac{S}{B}$	$\frac{S}{\sqrt{B}}$	$\frac{S}{\sqrt{S+B}}$
SEED4	SEED3	Monte Carlo	Est. S	In the Wings	Sgnl. Rgn. Est. B			
0.2	0.2	328/343	13.1	98	5.7	2.3	5.5	3.0
0.2	0.5	328/325	12.7	77	4.4	2.9	6.0	3.1
0.2	0.8	328/304	12.3	71	4.1	3.0	6.1	3.0
0.2	1.0	328/295	12.1	68	3.9	3.1	6.1	3.0
0.2	1.2	328/284	11.8	68	3.9	3.0	6.0	3.0
0.2	1.5	328/264	11.4	60	3.5	3.3	6.1	3.0
0.2	1.7	328/261	11.4	59	3.4	3.3	6.2	3.0
0.2	2.0	328/248	11.1	55	3.2	3.5	6.2	2.9

Table 4.22: Expected number of total (SEED4 and SEED3 combined) $KKK\pi$ signal events and background events for various SEED3 FOM cuts. SEED4 FOM cut has been fixed at FOM > 0.2.

FOM		Signal		Background (Data)		$\frac{S}{B}$	$\frac{S}{\sqrt{B}}$	$\frac{S}{\sqrt{S+B}}$
SEED4	SEED3	Monte Carlo	Est. S	In the Wings	Sgnl. Rgn. Est. B			
0.5	0.2	299/343	12.6	84	4.8	2.6	5.7	3.0
0.5	0.5	299/325	12.2	63	3.6	3.4	6.4	3.1
0.5	0.8	299/304	11.7	57	3.3	3.6	6.5	3.0
0.5	1.0	299/295	11.5	54	3.1	3.7	6.5	3.0
0.5	1.2	299/284	11.3	54	3.1	3.6	6.4	3.0
0.5	1.5	299/264	10.9	46	2.7	4.1	6.7	3.0
0.5	1.7	299/261	10.8	45	2.6	4.2	6.7	3.0
0.5	2.0	299/248	10.6	41	2.4	4.5	6.9	2.9

Table 4.23: Expected number of total (SEED4 and SEED3 combined) $KKK\pi$ signal events and background events for various SEED3 FOM cuts. SEED4 FOM cut has been fixed at FOM > 0.5.

FOM		Signal		Background (Data)		$\frac{S}{B}$	$\frac{S}{\sqrt{B}}$	$\frac{S}{\sqrt{S+B}}$
SEED4	SEED3	Monte Carlo	Est. S	In the Wings	Sgnl. Rgn. Est. B			
1.0	0.2	270/343	12.0	81	4.7	2.6	5.6	2.9
1.0	0.5	270/325	11.7	60	3.5	3.4	6.3	3.0
1.0	0.8	270/304	11.2	54	3.1	3.6	6.4	3.0
1.0	1.0	270/295	11.0	51	2.9	3.7	6.4	2.9
1.0	1.2	270/284	10.8	51	2.9	3.7	6.3	2.9
1.0	1.5	270/264	10.4	43	2.5	4.2	6.6	2.9
1.0	1.7	270/261	10.3	42	2.4	4.3	6.6	2.9
1.0	2.0	270/248	10.0	38	2.2	4.6	6.8	2.9

Table 4.24: Expected number of total (SEED4 and SEED3 combined) $KKK\pi$ signal events and background events for various SEED3 FOM cuts. SEED4 FOM cut has been fixed at FOM > 1.0.

FOM		Signal		Background (Data)		$\frac{S}{B}$	$\frac{S}{\sqrt{B}}$	$\frac{S}{\sqrt{S+B}}$
SEED4	SEED3	Monte Carlo	Est. S	In the Wings	Sgnl. Rgn. Est. B			
1.5	0.2	245/343	11.6	74	4.3	2.7	5.6	2.9
1.5	0.5	245/325	11.2	53	3.1	3.7	6.4	3.0
1.5	0.8	245/304	10.8	47	2.7	4.0	6.5	2.9
1.5	1.0	245/295	10.6	44	2.5	4.2	6.6	2.9
1.5	1.2	245/284	10.3	44	2.5	4.1	6.5	2.9
1.5	1.5	245/264	9.9	36	2.1	4.8	6.9	2.9
1.5	1.7	245/261	9.9	35	2.0	4.9	6.9	2.9
1.5	2.0	245/248	9.6	31	1.8	5.4	7.2	2.8

Table 4.25: Expected number of total (SEED4 and SEED3 combined) $KKK\pi$ signal events and background events for various SEED3 FOM cuts. SEED4 FOM cut has been fixed at FOM > 1.5.

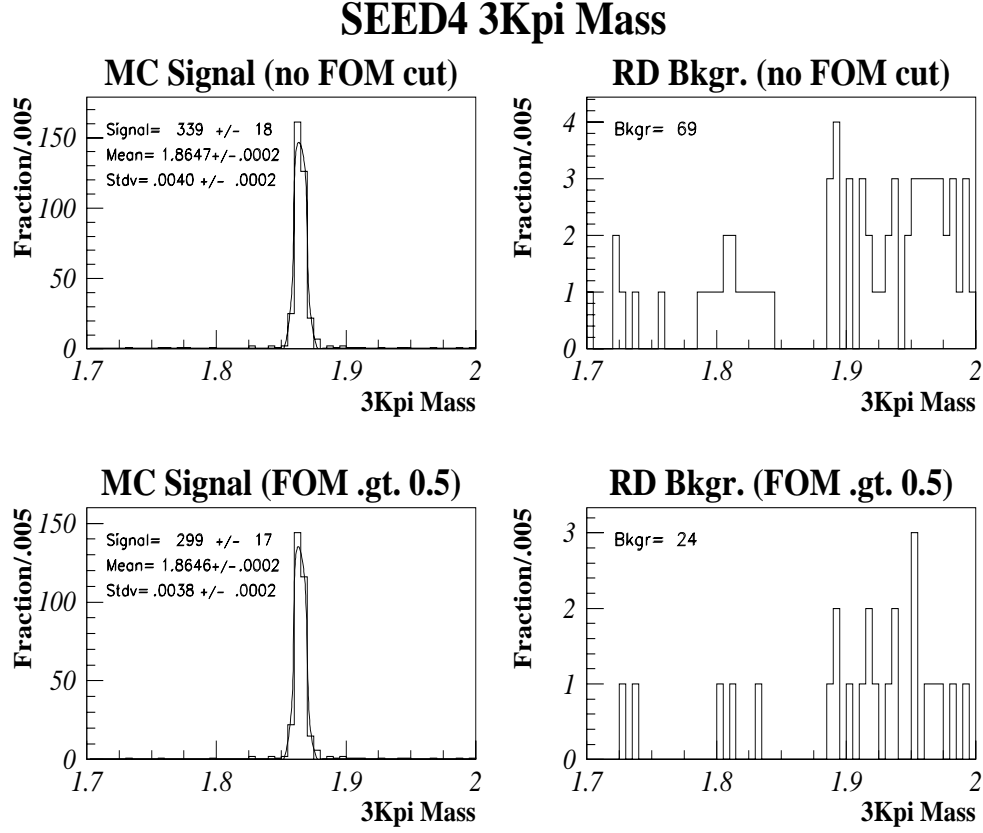


Figure 4.26: SEED4 $KKK\pi$ Monte Carlo signal (left) and real data (right) background distributions before (top) and after (bottom) the optimized FOM cut $\text{FOM} > 0.5$.

There are many SEED4 and SEED3 FOM cut combinations that has $S/\sqrt{S+B} = 3.0$, but if we break the tie using S/\sqrt{B} , the SEED4 FOM cut is fixed at $\text{FOM} > 0.5$ (Table 4.23). If we then select the SEED3 FOM cut so that SEED3 S/B (Table 4.20) gets as close as possible to SEED4 S/B (Table 4.19) at SEED4 $\text{FOM} > 0.5$, that singles out the SEED3 FOM cut at $\text{FOM} > 1.0$ (Table 4.23). Thus, the choice was SEED4 $\text{FOM} > 0.5$ and SEED3 $\text{FOM} > 1.0$. Figs. 4.26 and 4.27 show the $KKK\pi$

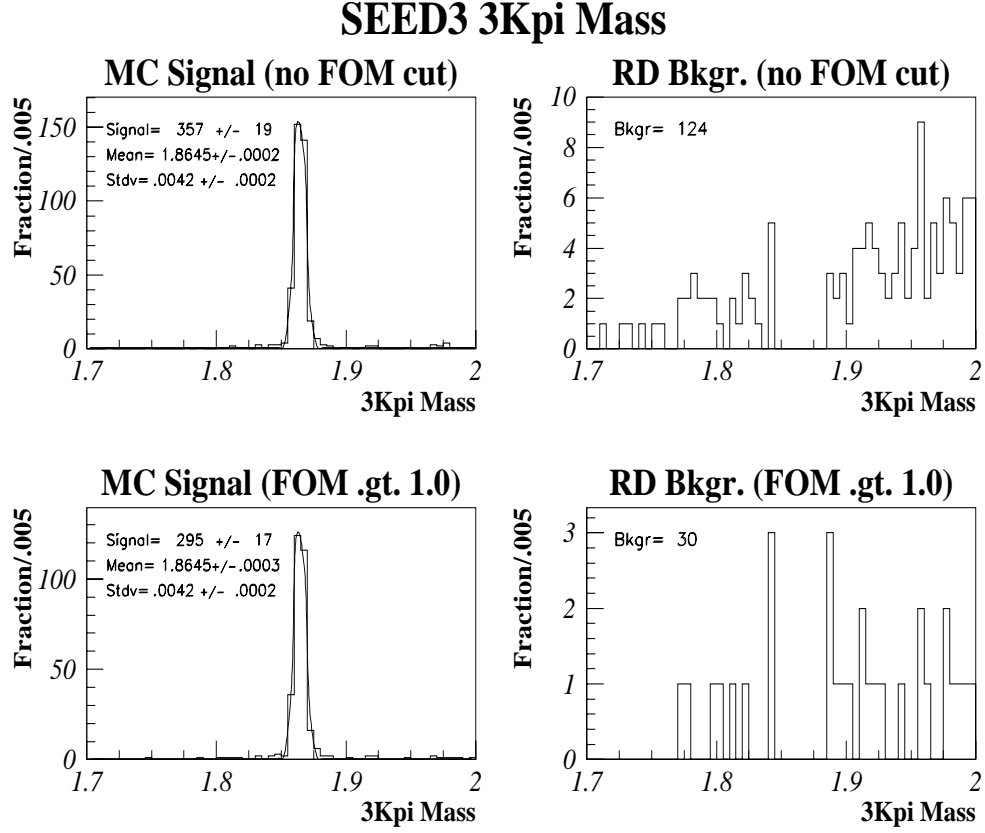


Figure 4.27: SEED3 $KKK\pi$ Monte Carlo signal (left) and real data (right) background distributions before (top) and after (bottom) the optimized FOM cut FOM > 1.0 .

mass histograms before (top) and after (bottom) the optimized FOM cut for SEED4 and SEED3 respectively. On the left are $KKK\pi$ Monte Carlo signal and on the right are the real data background distributions.

4.7 The Optimized Cuts for $D^0 \rightarrow K^- K^- K^+ \pi^+$

Table 4.26 summarizes the optimized cuts selected for the $D^0 \rightarrow K^- K^- K^+ \pi^+$ data sample. The parameters that were considered but not used are not shown in the table. They are MCAT, NCAT3, CHIP, CVP, PCVK, PTSQ, and SDCA⁸. The set of optimal cuts given in Table 4.26 were used as the center⁹ of the selection criteria, for the $D^0 \rightarrow K^- K^- K^+ \pi^+$ decay, for further analysis.

⁸In E791 terminology, CAT was calculated using NEWCATSG. A BAFFLE cut of $\frac{dy}{dz} < -0.002$.or. $\frac{dy}{dz} > 0.0005$ has also been applied. The NEWCATSG and the BAFFLE cut, which are specific to the E791 experiment, do improve the sensitivity of the final results, but they are not directly related to the optimization process.

⁹The optimal cuts — only one most of the time — were slightly varied at times when making other estimates such as systematic errors.

Parameter	SEED4	SEED3
CAT	3, 7, 15	3, 7, 15
CHIS	< 10	< 10
CVK	In FOM($> .2$)	In FOM($> .2$)
DIP	In FOM($< 60 \mu m$)	In FOM($< 60 \mu m$)
PTBL	$< .25 \text{ GeV}$	$< .25 \text{ GeV}$
SPTSQ	$> .2$	$> .3$
MRAT	No Cut	In FOM(< 1)
PRAT	$< .005$	$< .005$
SDZ	> 10	> 12
SDZT	> 1	No Cut
COSSP	In FOM	In FOM
TAU	$< 3.5 \text{ ps}$	No Cut
DELZ & ISOL	DELZ $> .5 \text{ cm}$.OR. ISOL $> .002 \text{ cm}$	DELZ $> .5 \text{ cm}$.OR. ISOL $> .008 \text{ cm}$
FOM	$> .5$	> 1

Table 4.26: The optimized cuts for $D^0 \rightarrow K^- K^- K^+ \pi^+$.

Chapter 5

Branching Ratio and Resonance

Structure

With the optimized cuts given in Table 4.26 applied to the data sample, the $KKK\pi$ “blind” mass window was opened. The full data sample with optimally selected $KKK\pi$ events as well as a large number of $K\pi\pi\pi$ events then became available for further study. This data sample, which is not “blind” any more, was used to make the measurements of branching ratio of $KKK\pi$ decay and the systematic uncertainty associated with it. The K^-K^+ resonant structure of $D^0 \rightarrow K^-K^-K^+\pi^+$ was also studied.

5.1 Branching Ratio of $D^0 \rightarrow K^- K^- K^+ \pi^+$

The branching ratio of the $D^0 \rightarrow K^- K^- K^+ \pi^+$ decay was measured relative to the normalization channel $D^0 \rightarrow K^- \pi^- \pi^+ \pi^+$. The relative branching ratio of $D^0 \rightarrow K^- K^- K^+ \pi^+$ is the ratio between the number of $KKK\pi$ signal events and that of $K\pi\pi\pi$ signal events corrected for detector and reconstruction efficiencies. To make these corrections, the generated Monte Carlo data sample (section 4.2) was used. If the rates of efficiencies estimated using the Monte Carlo simulations is correct, the ratio between the $D^0 \rightarrow K^- K^- K^+ \pi^+$ and $D^0 \rightarrow K^- \pi^- \pi^+ \pi^+$ decay rates (the relative branching ratio) is given by,

$$\frac{N_{KKK\pi}}{N_{K\pi\pi\pi}} = \frac{S_{KKK\pi RD} / \epsilon_{KKK\pi}}{S_{K\pi\pi\pi RD} / \epsilon_{K\pi\pi\pi}} \quad (5.1)$$

$$= \frac{S_{KKK\pi RD}}{S_{K\pi\pi\pi RD}} \times \frac{S_{K\pi\pi\pi MC}}{S_{KKK\pi MC}} \quad (5.2)$$

where S stands for the number of signal events and the subscripts indicate whether the events are $KKK\pi$ or $K\pi\pi\pi$ and the data sample is real data (RD) or Monte Carlo data (MC). $\epsilon_{KKK\pi}$ and $\epsilon_{K\pi\pi\pi}$ denote the overall acceptance for $KKK\pi$ and $K\pi\pi\pi$ events respectively¹. In this section, the relative branching ratio (relative BR) is calculated assuming the Monte Carlo simulation correctly models the ratio

¹500,000 events have been generated in each decay channel. They have not been shown in the Eqn. 5.2 as they cancel out.

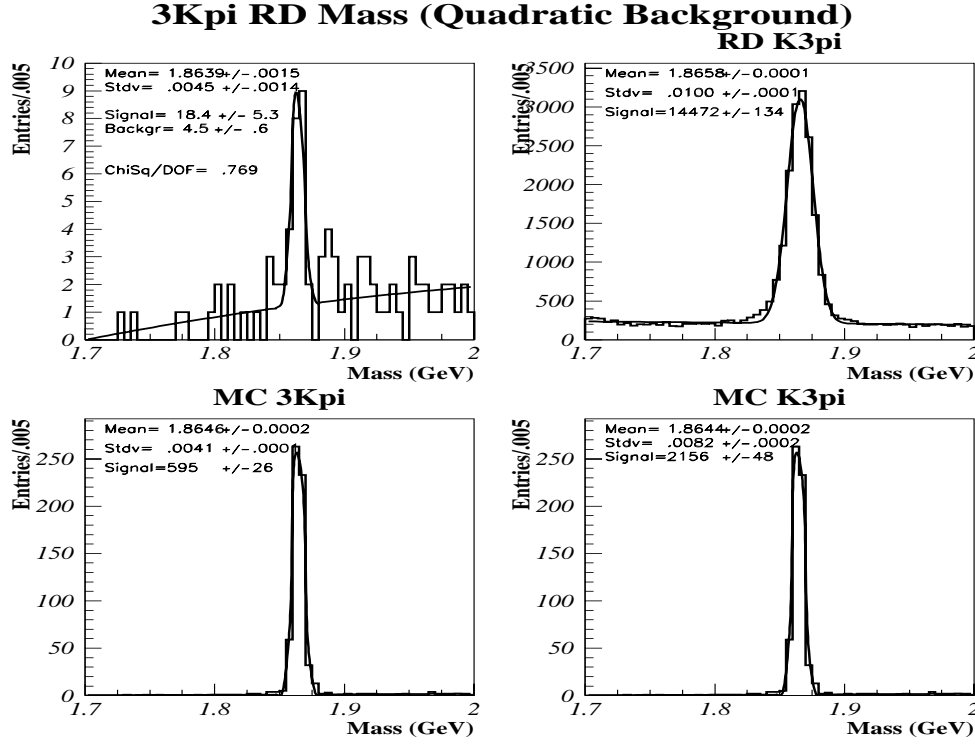


Figure 5.1: Mass distributions of real data $KKK\pi$ events (upper left), real data $K\pi\pi\pi$ events (upper right), Monte Carlo $KKK\pi$ events (bottom left), and Monte Carlo $K\pi\pi\pi$ events (bottom right) with optimized cuts applied (Table 4.26). The number of background events in the top left figure is that within 2σ .

of $KKK\pi$ and $K\pi\pi\pi$ detector efficiencies. Correction factors to the relative detector efficiency and the systematic uncertainties associated with the Monte Carlo modeling will be estimated in section 5.2

To evaluate the right hand side of Eqn. 5.2, mass histograms of all four data samples: $KKK\pi$ real data, $K\pi\pi\pi$ real data, $KKK\pi$ Monte Carlo data, and $K\pi\pi\pi$ Monte Carlo data were made (Fig. 5.1). The $KKK\pi$ data samples had all the

		Signal	Mass	Width
real data	3K π	18.4 ± 5.3	1.8639 ± 0.0015	0.0045 ± 0.0014
	K3 π	14472 ± 134	1.8658 ± 0.0001	0.0100 ± 0.0001
Monte Carlo	3K π	595 ± 26	1.8646 ± 0.0002	0.0041 ± 0.0001
	K3 π	2156 ± 48	1.8644 ± 0.0002	0.0082 ± 0.0002

Table 5.1: Real data and Monte Carlo data 3K π and K3 π mass histogram fit results. All the tuned cuts have been applied.

optimized cuts applied to them. The set of cuts that was applied to $K\pi\pi\pi$ data samples was different only in FOM, SDCA, and SDZT cuts; no FOM variable has been defined for $K\pi\pi\pi$ and the SDCA cut and the SDZT for $K\pi\pi\pi$ were $\text{SDCA} > 4$ and $\text{SDZT} > 2$.

An unbinned maximum likelihood fit was made for the real data $KKK\pi$ mass histogram. The signal was fitted with a Gaussian shape and the background was fitted with a quadratic shape. All the parameters: number of signal events, the mass (mean), the width (standard deviation) and the three parameters of the quadratic background were allowed to vary. Binned fits were made for the other three histograms: real data $K\pi\pi\pi$, Monte Carlo $KKK\pi$, and Monte Carlo $K\pi\pi\pi$ with a Gaussian signal and a linear background. Table 5.1 summarize the fit parameters of all four histograms. With these values in Eqn. 5.2, the ratio of the branching ratio between $D^0 \rightarrow K^- K^- K^+ \pi^+$ and $D^0 \rightarrow K^- \pi^- \pi^+ \pi^+$ is given by,

$$\frac{\epsilon_{K K K \pi}}{\epsilon_{K \pi \pi \pi}} = \frac{18.4 \pm 5.3}{14472 \pm 134} \times \frac{2156 \pm 48}{595 \pm 26} \quad (5.3)$$

$$= 0.0046 \pm 0.0013 \quad (5.4)$$

where the uncertainty represent only that due to statistical fluctuations.

5.2 Efficiency Corrections and Systematic Errors

In this analysis, Monte Carlo simulations were primarily used to optimize the $K K K \pi$ cuts and to estimate the acceptance of the detector for both $K K K \pi$ and $K \pi \pi \pi$ decay modes. Though Monte Carlo data describe the behavior of real data well enough to guide us through this process, they do not perfectly represent real data. A significant part of the systematic errors associated with the final result can be attributed to discrepancies between the real data and the Monte Carlo data that arise due to both systematic variations and statistical fluctuations in Monte Carlo data. Another part of systematic errors comes from representing the signal and the background using specified predetermined shapes –even though there are floating parameters. The difference in reconstruction efficiencies for $K K K \pi$ decays with different resonant substructure also contribute to the systematic uncertainty.

The FOM used in this analysis depends on both $KKK\pi$ Monte Carlo and $K\pi\pi\pi$ real data; neither of them perfectly represent $KKK\pi$ real data. Further, it is assumed that the parameters used to construct FOM were uncorrelated, which is only nearly true. Taking all these in to consideration, the most significant sources of systematic errors can be summarized as,

- statistical fluctuations in Monte Carlo data,
- systematic differences between Monte Carlo and real data:
 - SEED4 and SEED3 fractions,
 - \tilde{C} erenkov efficiency, and
 - SDZ, PTBL, and other cuts before FOM,
 - tracking and vertexing efficiencies,
- FOM predictions,
- signal and background shape, and
- ignoring resonant structures.

The systematic errors associated with the estimated detector efficiencies –mainly those come from the difference in Monte Carlo and real data– look more significant

	MC $KKK\pi$	MC $K\pi\pi\pi$	RD $K\pi\pi\pi$
SEED4	299 ± 18	1545 ± 41	9895 ± 109
SEED3	295 ± 18	612 ± 26	4582 ± 78

Table 5.2: Monte Carlo and real data $KKK\pi$ signal with tuned cuts and real data $K\pi\pi\pi$ signal with $K\pi\pi\pi$ box cuts. The corresponding plots are shown in Fig. 4.25 and the bottom left of Figs. 4.26 and 4.27.

than they actually are if they are separately estimated for $KKK\pi$ and $K\pi\pi\pi$ decay modes, but most such effects cancel out once the relative detector efficiency (the ratio between $KKK\pi$ and $K\pi\pi\pi$ efficiencies) is taken as a whole. This approach is appropriate as the relative efficiency is what we use in our calculations.

5.2.1 Statistical Fluctuations in Monte Carlo Data

Since Monte Carlo event generation is a statistical process, it inevitably involves some statistical fluctuations. This statistical fluctuations in the Monte Carlo data sample create a systematic uncertainty in the final results of the analysis. Table 5.2 shows the number of Monte Carlo and the real data $KKK\pi$ signal events obtained with the $KKK\pi$ tuned cuts and the number of real data $K\pi\pi\pi$ signal events obtained with $K\pi\pi\pi$ box cuts² (corresponding plots are shown in Fig. ?? and the bottom left of Figs. 4.26 and ??). The acceptance of the detector is calculated by counting the

²In this thesis, the tuned $KKK\pi$ cuts without the FOM cut and with $SDCA > 4$ and $SDZT > 2$ applied to the $K\pi\pi\pi$ data sample, are referred to as " $K\pi\pi\pi$ box cuts". The $KKK\pi$ tuned cuts and the $K\pi\pi\pi$ box cuts are collectively referred to as the final cuts or standard cuts.

number of Monte Carlo events that survive the final cuts and scaling it by the number of Monte Carlo events generated, which is 500,000 in each mode. The SEED4 and SEED3 $KKK\pi$ detector efficiencies, calculated with the $KKK\pi$ tuned cuts, are thus given by (Table 5.2),

$$\epsilon_{KKK\pi_4} = \frac{299 \pm 18}{500,000} = .060 \pm .004\% \quad (5.5)$$

$$\epsilon_{KKK\pi_3} = \frac{295 \pm 18}{500,000} = .059 \pm .004\% \quad (5.6)$$

where $\epsilon_{KKK\pi_4}$ and $\epsilon_{KKK\pi_3}$ stand for the detector efficiencies for SEED4 $KKK\pi$ and SEED3 $KKK\pi$ respectively. Similarly, the SEED4 and SEED3 $K\pi\pi\pi$ efficiencies, calculated in the same way with the $K\pi\pi\pi$ box cuts, are given by (Table 5.2),

$$\epsilon_{K\pi\pi\pi_4} = \frac{1545 \pm 41}{500,000} = .309 \pm .008\% \quad (5.7)$$

$$\epsilon_{K\pi\pi\pi_3} = \frac{612 \pm 26}{500,000} = .122 \pm .005\% \quad (5.8)$$

where $\epsilon_{K\pi\pi\pi_4}$ and $\epsilon_{K\pi\pi\pi_3}$ stand for the detector efficiencies for SEED4 $K\pi\pi\pi$ and SEED3 $K\pi\pi\pi$ respectively. The total $KKK\pi$ efficiency of the detector relative to $K\pi\pi\pi$ efficiency is thus given by (Eqns. 5.5 - 5.8),

$$\epsilon_{KKK\pi_{rel}} = \frac{\epsilon_{KKK\pi_4} + \epsilon_{KKK\pi_3}}{\epsilon_{K\pi\pi\pi_4} + \epsilon_{K\pi\pi\pi_3}} = .275 \pm .013 \quad (5.9)$$

which has a 4.7% uncertainty.

5.2.2 Difference in Monte Carlo and Real Data

Several calculation have been done to estimate the systematic errors associated with the final results due to the systematic differences in Monte Carlo and real data. Only the most significant contributions are presented —given the level of statistical error— fine details do not matter. They are the contributions from the difference in SEED4 and SEED3 fractions, Čerenkov efficiencies, SDZ distribution, and PTBL distributions.

SEED4 and SEED3 fractions

If the Monte Carlo data perfectly represent real data, and hence correctly give the SEED4 and SEED3 fractions, it should be true that,

$$\frac{S_{MC4}}{S_{MC3}} = \frac{S_{RD4}}{S_{RD3}} \quad (5.10)$$

so that,

$$\frac{S_{MC4}}{S_{MC3}} \times \frac{S_{RD3}}{S_{RD4}} = 1 \quad (5.11)$$

where S_{MC4} , S_{MC3} , S_{RD4} , and S_{RD3} are the number of signal events in SEED4 Monte Carlo data, SEED3 Monte Carlo data, SEED4 real data, and SEED3 real data respectively. We do not observe this. Instead, for $K\pi\pi\pi$ (Eqn. 5.11 and Table 5.2),

$$\frac{S_{MC4K\pi\pi\pi}}{S_{MC3K\pi\pi\pi}} \times \frac{S_{RD3K\pi\pi\pi}}{S_{RD4K\pi\pi\pi}} = r_4 = 1.169 = 1 + \delta_4 \quad (5.12)$$

and,

$$\frac{S_{MC3K\pi\pi\pi}}{S_{MC4K\pi\pi\pi}} \times \frac{S_{RD4K\pi\pi\pi}}{S_{RD3K\pi\pi\pi}} = r_3 = 0.855 = 1 + \delta_3 = \frac{1}{r_4} \quad (5.13)$$

In one extreme case, one can assume that Monte Carlo data perfectly represents SEED3 $K\pi\pi\pi$ real data, but overestimates SEED4 $K\pi\pi\pi$ by a fraction of δ_4 ; with this assumption, we can estimate the actual SEED4 $K\pi\pi\pi$ efficiency with (Eqns. 5.7 and 5.12),

$$\epsilon_{K\pi\pi\pi_4} \rightarrow \epsilon'_{K\pi\pi\pi_4} = \frac{\epsilon_{K\pi\pi\pi_4}}{r_4} = 0.264\% \quad (5.14)$$

If we further assume that this fraction of overestimation is true also for $KKK\pi$ data, we can make the same correction to the SEED4 $KKK\pi$ efficiency to get (Eqns. 5.5 and 5.12),

$$\epsilon_{KKK\pi_4} \rightarrow \epsilon'_{KKK\pi_4} = \frac{\epsilon_{KKK\pi_4}}{r_4} = .051\% \quad (5.15)$$

In this method, the total $KKK\pi$ efficiency of the detector relative to $K\pi\pi\pi$ efficiency is given by (Eqns. 5.6, 5.8, 5.14, and 5.15),

$$\epsilon'_{KKK\pi_{rel}} = \frac{\epsilon'_{KKK\pi_4} + \epsilon_{KKK\pi_3}}{\epsilon'_{K\pi\pi\pi_4} + \epsilon_{K\pi\pi\pi_3}} = 0.285 \quad . \quad (5.16)$$

Similarly, in the other extreme case, we can assume Monte Carlo data perfectly represents SEED4 $K\pi\pi\pi$ real data, but underestimates SEED3 $K\pi\pi\pi$ by a fraction of δ_3 ; with this assumption, we can estimate the actual SEED3 $K\pi\pi\pi$ efficiency, and SEED3 $KKK\pi$ efficiency the same way we did for SEED4, with (Eqns. 5.6, 5.8, and 5.13),

$$\epsilon_{K\pi\pi\pi_3} \rightarrow \epsilon'_{K\pi\pi\pi_3} = \frac{\epsilon_{K\pi\pi\pi_3}}{r_3} = 0.143\% \quad (5.17)$$

and,

$$\epsilon_{KKK\pi_3} \rightarrow \epsilon'_{KKK\pi_3} = \frac{\epsilon_{KKK\pi_3}}{r_3} = 0.069\% \quad (5.18)$$

In this method, the total $KKK\pi$ efficiency of the detector relative to $K\pi\pi\pi$ efficiency is given by (Eqns. 5.5, 5.7, 5.17, and 5.18),

$$\epsilon''_{KKK\pi_{rel}} = \frac{\epsilon_{KKK\pi_4} + \epsilon'_{KKK\pi_3}}{\epsilon_{K\pi\pi\pi_4} + \epsilon'_{K\pi\pi\pi_3}} = 0.285 \quad (5.19)$$

If we calculate the relative efficiency without any corrections we get (Eqns. 5.5, 5.6, 5.7, and 5.8),

$$\epsilon_{KKK\pi_{rel}} = \frac{\epsilon_{KKK\pi_4} + \epsilon_{KKK\pi_3}}{\epsilon_{K\pi\pi\pi_4} + \epsilon_{K\pi\pi\pi_3}} = 0.275 \quad (5.20)$$

If we take the average of the three relative efficiencies: $\epsilon_{KKK\pi_{rel}}$, $\epsilon'_{KKK\pi_{rel}}$, and $\epsilon''_{KKK\pi_{rel}}$ as the best estimate, and half the difference between the two extreme values as the systematic error, we get,

$$\epsilon_{KKK\pi_{rel}} = 0.282 \pm 0.005 \quad (5.21)$$

which is 2.5% greater than the relative efficiency we obtained from Monte Carlo. The systematic uncertainty is thus 1.8%.

Kaon Čerenkov Efficiency

It has been established previously that the Monte Carlo simulation of Čerenkov efficiencies is not as good as the simulation of tracking, vertexing, etc.. The efficiency for identifying individual kaons using $CVK > .2$ cut (Appendix B) has been measured as a function of p and p_T using $D^0 \rightarrow K^- \pi^+$ and $D^0 \rightarrow K^- \pi^- \pi^+ \pi^+$ real data and found to be independent of the decay mode [22] [23]. We use the Monte Carlo simulations of $D^0 \rightarrow K^- K^- K^+ \pi^+$ and of $D^0 \rightarrow K^- \pi^- \pi^+ \pi^+$ and the Čerenkov efficiencies measured using real data to determine a correction factor and an associated systematic uncertainty. The analysis has the three CVK cuts: $CVK1 > .2$, $CVK2 > .2$, and $CVK3 > .2$ applied to the data sample before FOM. FOM uses the distributions of all CVK1, CVK2, and CVK3 after these hard cuts. The systematic uncertainty and the correction factor only associated with the hard cuts are estimated in this section. The systematic uncertainty that is caused by CVK FOM will be estimated in section 5.2.3 as part of the systematic uncertainty associated with FOM.

Čerenkov identification efficiency depends on both the momentum p and the transverse momentum p_T of the track. The momentum dependence comes from the production characteristics of Čerenkov light which depends on the speed of the par-

ticle. The Čerenkov angle is given by $\cos \theta = 1/\beta n$ and the energy carried off by the Čerenkov light is proportional to $\int \omega d\omega (1 - 1/\beta^2 n^2)$ where the integration is only over frequencies for which $\beta n(\omega) > 1$ [21]. The p_T dependence results from the track density which becomes lower as we go away from the center of the detector [23]. These efficiencies, that have been estimated using real data of the decays with good statistics [23], were used to estimate a correction factor and the systematic uncertainty due to the $\text{CVK} > .2$ cuts. The estimations have been made with the cuts before the FOM, because the FOM requires a hard CVK cut at $\text{CVK1} > .2$, $\text{CVK2} > .2$, and $\text{CVK3} > .2$ which is not there in part of the calculation.

To make this estimation, Čerenkov efficiency was calculated in two ways. The observed Čerenkov efficiency was calculated by simply applying and removing the CVK cuts to the data sample and measuring the number of signal events in each case. An estimate of Čerenkov efficiency was also made using Čerenkov efficiency of individual events $\epsilon(p, p_T)$ where p and p_T are the momentum and the transverse momentum of the track. The values for $\epsilon(p, p_T)$ have been derived from $D^0 \rightarrow K^- \pi^+$ and $K \pi \pi \pi$ real data [23]. The Čerenkov efficiencies of K1, K2, and K3 of a particular candidate were assumed to be uncorrelated, and the Čerenkov efficiency of that event was represented by the product of the Čerenkov efficiencies of K1, K2, and K3. To do this calculation, following procedure was adopted.

- To make the first estimate of the relative Čerenkov efficiency, a mass histogram of Monte Carlo $KKK\pi$ data was made with all the Čerenkov cuts: $CVK1 > .2$, $CVK2 > .2$, and $CVK3 > .2$ (along with the other optimized cuts before FOM) applied. A mass histogram of Monte Carlo $K\pi\pi\pi$ was also made with its $CVK > .2$ applied.
- Fits for these histograms were made. Let these numbers, which are the observed number of Monte Carlo $KKK\pi$ and $K\pi\pi\pi$ signal events, respectively, after the $CVK > .2$ cut, be represented by $(S_{obs})_{CVK>.2}$
- The mass histograms for Monte Carlo $KKK\pi$ and $K\pi\pi\pi$ data were also made without any $CVK > .2$ cut applied.
- Fits for these histograms were also made. Let these numbers, which are the observed number of Monte Carlo $KKK\pi$ and $K\pi\pi\pi$ signal events, respectively, before the $CVK > .2$ cut, be represented by $(S_{obs})_{CVK>0}$
- Using $(S_{obs})_{CVK>.2}$ and $(S_{obs})_{CVK>0}$ the observed CVK efficiency ϵ_{obs} for both $KKK\pi$ and $K\pi\pi\pi$ was calculated.
- The first estimate of the relative Čerenkov efficiency was derived from these Čerenkov efficiencies for $KKK\pi$ and $K\pi\pi\pi$. Let this value be ϵ_{rel} .

- To make the second estimate of the relative efficiency a mass histogram of Monte Carlo $KKK\pi$ data was made with all the CVK cuts: $CVK1 > .2$, $CVK2 > .2$, and $CVK3 > .2$ applied weighting each event by $1/[\epsilon_1(p, p_T) \times \epsilon_2(p, p_T) \times \epsilon_3(p, p_T)]$ where ϵ_1 , ϵ_2 , and ϵ_3 correspond to K1, K2, and K3 respectively. This number gives the number of Monte Carlo $KKK\pi$ events there should have been before the CVK cuts according to real data Čerenkov efficiencies.
- Similarly, a mass histogram of Monte Carlo $K\pi\pi\pi$ data was made with its CVK $> .2$ cut applied weighting each event by $1/\epsilon(p, p_T)$.
- Fits for these histograms were made. Let these numbers, which are the estimated number of Monte Carlo $KKK\pi$ and $K\pi\pi\pi$ signal events, respectively, before the $CVK > .2$ cut, be represented by $(S_{est})_{CVK>0}$.
- Using $(S_{obs})_{CVK>.2}$ and $(S_{est})_{CVK>0}$ the estimate CVK efficiency ϵ_{est} for both $KKK\pi$ and $K\pi\pi\pi$ was calculated.
- The second estimate of the relative Čerenkov efficiency was derived from these Čerenkov efficiencies for $KKK\pi$ and $K\pi\pi\pi$. Let this value be ϵ'_{rel} .
- ϵ'_{rel} thus calculated was taken as the best estimate of the $KKK\pi$ relative detector efficiency. The average was not taken as the best estimate as we believe Čerenkov efficiencies from real data are much better than those from

Monte Carlo data. Half the difference between the two estimates of relative Čerenkov efficiencies was taken as the systematic uncertainty associated with the Čerenkov cuts at $CVK > .2$.

Table 5.3 shows the numbers calculated using the procedure described above. The best estimate of the $KKK\pi$ relative detector efficiency is 0.523, which is 18% lower than the $KKK\pi$ relative detector efficiency when no CVK cut has been applied (0.640). The fractional systematic uncertainty associated with the Čerenkov cuts at $CVK > .2$ is 10%.

	$KKK\pi$	$K\pi\pi\pi$
$(S_{obs})_{CVK>.2}$	694 ± 29	2156 ± 47
$(S_{obs})_{CVK>0}$	1670 ± 42	3321 ± 62
ϵ_{obs}	.416	.649
ϵ_{rel}	.640	
$(S_{est})_{CVK>0}$	1945 ± 44	3160 ± 59
ϵ_{est}	.357	.682
ϵ'_{rel}	.523	

Table 5.3: Observed and estimated number of Monte Carlo $KKK\pi$ and $K\pi\pi\pi$ signal events with and without $CVK > .2$ cuts along with the Čerenkov efficiencies. The estimation has been done using Čerenkov efficiencies of real data.

SDZ Cut

Like many other cuts, SDZ cut was also determined using Monte Carlo data as a guide. Nevertheless, $K\pi\pi\pi$ SDZ distributions show less than perfect Monte Carlo representation of SDZ variation. On average, SDZ of $K\pi\pi\pi$ Monte Carlo is a little lower than $K\pi\pi\pi$ real data (Figs. 4.3 and 4.4). This assures a higher SDZ cut efficiency for real data than for Monte Carlo data at the same cut level, hence leading to a systematic error. This systematic error was estimated by loosening the SDZ cut on Monte Carlo data, by an amount determined as described below, so as to try to match the efficiency there might have been in real data at the former cut level.

	MC $K\pi\pi\pi$	RD $K\pi\pi\pi$	$\Delta(SDZ_{av})$	Modified Cut
SEED4	28.5 ± 0.4	31.6 ± 0.2	3.1 ± 0.4	$SDZ > 6.9$
SEED3	31.1 ± 0.7	33.1 ± 0.2	2.0 ± 0.7	$SDZ > 10.0$

Table 5.4: First and second columns show $K\pi\pi\pi$ Monte Carlo and real data SDZ averages obtained with final cuts. In third column is their differences. The fourth column shows the modified $K\pi\pi\pi$ SDZ cut.

Table 5.2 shows the number of $K\pi\pi\pi$ Monte Carlo and real data signal events obtained with final cuts and the first two columns of Table 5.4 shows the SDZ averages of these two data samples. To estimate the systematic errors, Monte Carlo $K\pi\pi\pi$ mass plots were remade with an SDZ cut which is looser than the tuned SDZ cuts, $SDZ > 10$ for SEED4 $SDZ > 12$ for SEED3, by an amount equal to the difference

	MC $KKK\pi$	MC $K\pi\pi\pi$	Ratio	ΔSDZ_{av}	Modified Cut
SEED4	$.0402 \pm .0008$	$.0250 \pm .0003$	$.622 \pm .014$	$1.9 \pm .3$	$SDZ > 8.1$
SEED3	$.0426 \pm .0008$	$.0240 \pm .0004$	$.563 \pm .014$	$1.1 \pm .4$	$SDZ > 10.9$

Table 5.5: Average SIGMA of $KKK\pi$ and $K\pi\pi\pi$ Monte Carlo data with final cuts, ratio of the latter to the former, estimated difference between Monte Carlo and real data $KKK\pi$ SDZ averages, and the modified $KKK\pi$ SDZ cut.

between average SDZ of real data $K\pi\pi\pi$ and that of Monte Carlo $K\pi\pi\pi$. The last two columns of Table 5.4 show the difference between $K\pi\pi\pi$ Monte Carlo and real data SDZ averages and the modified SDZ cut.

For $KKK\pi$, similar mass plots were made, but this time the SDZ difference was determined by scaling the $K\pi\pi\pi$ SDZ difference (the third column of Table 5.4) by the ratio of Monte Carlo $K\pi\pi\pi$ and $KKK\pi$ average SIGMA (the third column of Table 5.5). The last two columns of Table 5.5 show the ΔSDZ_{ave} and the modified SDZ cut thus estimated for $KKK\pi$. Table 5.6 shows the number of Monte Carlo $KKK\pi$ and $K\pi\pi\pi$ signal events obtained with those modified SDZ cuts.

In the final step of the calculation, the detector efficiency of $KKK\pi$ relative to that of $K\pi\pi\pi$ was estimated in two ways: once with the optimized SDZ cuts ($\epsilon_{KKK\pi_{rel}}$) and then with the modified SDZ cuts ($\epsilon_{KKK\pi_{rel}}^{\prime}$). They are,

$$\epsilon_{KKK\pi_{rel}} = \frac{299 + 295}{1545 + 612} = 0.275 \quad (5.22)$$

	MC $KKK\pi$	MC $K\pi\pi\pi$
SEED4	309 ± 18	1594 ± 41
SEED3	322 ± 18	649 ± 26

Table 5.6: Number of Monte Carlo $KKK\pi$ and $K\pi\pi\pi$ signal events obtained with the modified SDZ cuts (Tables 5.4 and 5.5) and the other final cuts.

and,

$$\epsilon'_{KKK\pi_{rel}} = \frac{309 + 322}{1594 + 649} = 0.281 \quad (5.23)$$

The average of these two numbers were taken as the best estimate and half the difference was taken as the systematic error. These values turned out to be,

$$\epsilon_{KKK\pi_{rel}} = 0.278 \pm 0.003 \quad (5.24)$$

which is 1.1% higher than the relative efficiency calculated with Monte Carlo data.

The systematic uncertainty is 1.1%.

PTBL Cut

PTBL is another parameter whose $K\pi\pi\pi$ Monte Carlo distribution is somewhat different from the $K\pi\pi\pi$ real data distribution signaling a similar discrepancy in $KKK\pi$ Monte Carlo and real data too (Figs. 4.9 and 4.10). The average of $K\pi\pi\pi$ Monte Carlo PTBL distribution is slightly lower than that of its real data counterpart. As a result, the efficiency of the PTBL cut for Monte Carlo data tends to be a little higher than that for real data is. The systematic error that comes from this

	MC $K\pi\pi\pi$	RD $K\pi\pi\pi$	$\Delta(PTBL_{av})$	Modified Cut
SEED4	$.1041 \pm .0015$	$.1154 \pm .0006$	$.0113 \pm .0016$	$PTBL < .2387$
SEED3	$.1111 \pm .0025$	$.1212 \pm .0009$	$.0101 \pm .0027$	$PTBL < .2399$

Table 5.7: The $K\pi\pi\pi$ PTBL averages of Monte Carlo and real data with final cuts, their difference, and modified $K\pi\pi\pi$ PTBL cuts.

discrepancy was estimated by tightening the PTBL cut on Monte Carlo data, by an amount determined as described below, and recalculating the relative efficiency.

Table 5.7 show the Monte Carlo (first column) and real data (second column) $K\pi\pi\pi$ PTBL averages and their differences (third column) obtained with final cuts. To recalculate the relative efficiency, Monte Carlo $K\pi\pi\pi$ mass plots were remade with a PTBL cut which is tighter than the tuned PTBL cut by an amount equal to the difference between average PTBL of $K\pi\pi\pi$ real data and that of $K\pi\pi\pi$ Monte Carlo data. For $KKK\pi$, similar mass plots were made, but this time the difference in PTBL averages was determined by scaling the difference in $K\pi\pi\pi$ PTBL averages by the ratio of average PTBL of $KKK\pi$ Monte Carlo data and that of $K\pi\pi\pi$ Monte Carlo data (Tables 5.7 and 5.8). Table 5.9 shows the number of Monte Carlo $KKK\pi$ and $K\pi\pi\pi$ signal events thus obtained.

With the number of Monte Carlo signal events given in Table 5.2, obtained with final cuts, the efficiency is given by,

	MC $K\pi\pi\pi$	MC $KKK\pi$	$\Delta(PTBL_{av})$	Modified Cut
SEED4	$.1041 \pm .0015$	$.0966 \pm .0030$	$.0105 \pm .0015$	$PTBL < .2395$
SEED3	$.1111 \pm .0025$	$.1052 \pm .0031$	$.0096 \pm .0026$	$PTBL < .2304$

Table 5.8: The average PTBL of $K\pi\pi\pi$ and $KKK\pi$ Monte Carlo data, estimated difference between average PTBL of $KKK\pi$ real and Monte Carlo data, and the modified $KKK\pi$ PTBL cuts.

$$\epsilon_{KKK\pi_{rel}} = \frac{299 + 295}{1545 + 612} = 0.275 \quad . \quad (5.25)$$

With the modified PTBL cuts we get,

$$\epsilon'_{KKK\pi_{rel}} = \frac{299 + 293}{1528 + 602} = 0.278 \quad . \quad (5.26)$$

If we take the average of these two numbers (0.275 and 0.278) as the best estimate and half the difference as the systematic error, we get

$$\epsilon_{KKK\pi_{rel}} = 0.2765 \pm 0.0015 \quad (5.27)$$

This gives a 0.5% higher relative efficiency and a 0.5% systematic uncertainty.

	MC $KKK\pi$	MC $K\pi\pi\pi$
SEED4	299 ± 17	1528 ± 41
SEED3	293 ± 18	602 ± 26

Table 5.9: Number of Monte Carlo $KKK\pi$ and $K\pi\pi\pi$ signal events with modified PTBL cut and other final cuts.

Tracking and Vertexing Efficiencies

The systematic differences in tracking and vertexing efficiencies of Monte Carlo data and real data is another factor that contributes to the systematic uncertainty of the final result. These systematic variations have been studied previously [24]. According to those results, the systematic uncertainty associated with tracking and vertexing finding of D^0 is 4.6%. Based on that result, we have set a systematic uncertainty of 5% for this analysis.

5.2.3 FOM Predictions

The systematic errors in FOM predictions come about partly due to the correlations —though they are not strong— between the parameters that were used to construct FOM and partly due to the discrepancy in Monte Carlo and real data.

The systematic error associated with these predictions, due to correlations of the parameters in FOM, have already been calculated in section 4.5.4 as we were looking to see how strong the correlations were. According to this calculation (Tables 4.17 and 4.18), the systematic error for both SEED4 at $\text{FOM} > .5$ and SEED3 at $\text{FOM} > 1$ is 1%.

FOM		Signal		Background (Data)		$\frac{S}{B}$	$\frac{S}{\sqrt{B}}$	$\frac{S}{\sqrt{S+B}}$
SEED4	SEED3	Monte Carlo	Est. S	In the Wings	Sgnl. Rgn. Est. B			
0.5	1.0	292/294	11.4	53	3.1	3.7	6.5	3.0
		300/291	11.5	59	3.4	3.4	6.2	3.0
		299/295	11.5	54	3.1	3.7	6.5	3.0

Table 5.10: $KKK\pi$ predicted signal and background with the optimized cuts and the three types of Monte Carlo. The top, middle and bottom lines respectively correspond to the FOM whose SPROBs were based solely on $KKK\pi$ Monte Carlo data, that whose CVK and DIP SPROBs came from $K\pi\pi\pi$ real data, and that whose CVK and DIP SPROBs were the average of the above two sets of SPROBs.

The systematic errors in FOM predictions due to the difference in Monte Carlo and real data can be estimated by looking at the number of signal events we predict using the two sets of FOMs: FOM that solely come from $KKK\pi$ Monte Carlo data and that whose CVK and DIP fractions come from $K\pi\pi\pi$ real data and other fractions come from Monte Carlo $KKK\pi$ data. In the former case we predict 11.4 signal events whereas in the latter we predict 11.5 (Table 5.10). From the recipe we have been adopting so far, this numbers indicates a systematic uncertainty of 0.4%.

If we add all three effects: 1% systematic error from SEED4 correlations, another 1% from SEED3 correlations, and 0.4% due to the difference in Monte Carlo and real data, in quadrature, this turns out to be an effect of 1.5%

5.2.4 Signal and Background Shape

Fitting the signal and the background to a particular shape is another factor that contributes to the systematic uncertainty in the final result. In this analysis the number of signal and background events have been estimated by fitting the final data sample to a Gaussian signal and a quadratic background shape with all the fit parameters floating (Fig. 5.1 and the fifth row of Table 5.11). The systematic uncertainty associated with the number of $KKK\pi$ signal events has been estimated by refitting the final data sample to eight different signal/background shapes.

In all eight fits, the signal was fitted with a Gaussian shape. One set of four fits were made with a linear background shape and another set of four fits were made with quadratic background. In each set, one fit was made leaving both the mean and the standard deviation of the Gaussian signal (the mass and the width) to vary. Two other fits were made, one with the mass fixed at 1.8646 GeV, which is the D^0 mass given in Particle Data Group's data book (PDG value), and the other with the width fixed at 0.0040 GeV which is the value that $KKK\pi$ Monte Carlo fit suggests. The fourth fit had both mass and width fixed at the above values.

Table 5.11 shows the results of the eight final fits made for $3K\pi$ real data sample. The first column reads the shape of the fit; G+P1 means that the signal has been

Shape	Fixed	Sgnl	Bkgr	Mass	Width	χ^2/DOF
G+P1	none	18.8 ± 5.2	$4.5 \pm .6$	$1.8638 \pm .0016$	$.0047 \pm .0015$.811
G+P1	mass	18.3 ± 5.0	$4.3 \pm .5$	1.8646 (fixed)	$.0044 \pm .0012$.806
G+P1	width	17.9 ± 4.8	$3.9 \pm .5$	$1.8641 \pm .0012$.0040 (fixed)	.803
G+P1	both	17.8 ± 4.8	$3.9 \pm .5$	1.8646 (fixed)	.0040 (fixed)	.804
G+P2	none	18.4 ± 5.3	$4.5 \pm .6$	$1.8639 \pm .0015$	$.0045 \pm .0014$.769
G+P2	mass	18.0 ± 4.8	$4.4 \pm .5$	1.8646 (fixed)	$.0043 \pm .0012$.763
G+P2	width	17.7 ± 4.7	$4.1 \pm .5$	$1.8641 \pm .0013$.0040 (fixed)	.759
G+P2	both	17.6 ± 4.7	$4.1 \pm .5$	1.8646 (fixed)	.0040 (fixed)	.759

Table 5.11: $KKK\pi$ real data fit results for eight fit types (G, P1, and P2 indicate a Gaussian signal, linear background, and a quadratic background respectively). The second column shows what fit parameters were fixed in the fit. The number of background events is that under the signal within $\pm 2\sigma$.

fit to a Gaussian shape while the background has assumed a linear shape (first order polynomial). Similarly, G+P2 means a Gaussian signal and a quadratic background. The second column shows what fit parameters have been fixed in the fit. The first and fifth rows correspond to the fits in which all the fit parameters were allowed to float. The second and the sixth correspond to fixed mass fits while the third and the seventh rows correspond to fixed width fits. The fourth and eighth rows correspond to the fits where both mass and the width were kept fixed. The last column of the table gives the χ^2/DOF of the fit.

The χ^2/DOF of all the plots are good. The variation of the number of signal is very small. We use 18.4 as the best estimate of the number of signal events. This number was obtained from the fit whose both mass and the width floated during the fit. The best estimate make the biggest difference with 17.6 (last row). We use the percentage difference between the best estimate 18.4 and the extreme value 17.6 as the systematic uncertainty. This is 4.3%.

5.2.5 $D^0 \rightarrow \phi K^- \pi^+$

In this analysis, the relative efficiency of the detector ($\epsilon_{KKK\pi}/\epsilon_{K\pi\pi\pi}$) was estimated by generating 500,000 $D^0 \rightarrow K^- K^- K^+ \pi^+$ (non resonant) and $D^0 \rightarrow K^- \pi^- \pi^+ \pi^+$ Monte Carlo events and pushing the generated events through analysis algorithm; the effect of $D^0 \rightarrow \phi K^- \pi^+; \phi \rightarrow K^- K^+$ on the estimation of the relative efficiency was not taken in to consideration. Had there been a significant fraction of $D^0 \rightarrow \phi K^- \pi^+; \phi \rightarrow K^- K^+$ events in the real data sample and the relative efficiency of the detector for that decay been significantly different from that for the non resonant decay there could have been a systematic error due to the ignorance of the resonant decay in the estimation of the relative efficiency of $D^0 \rightarrow K^- K^- K^+ \pi^+$ decay.

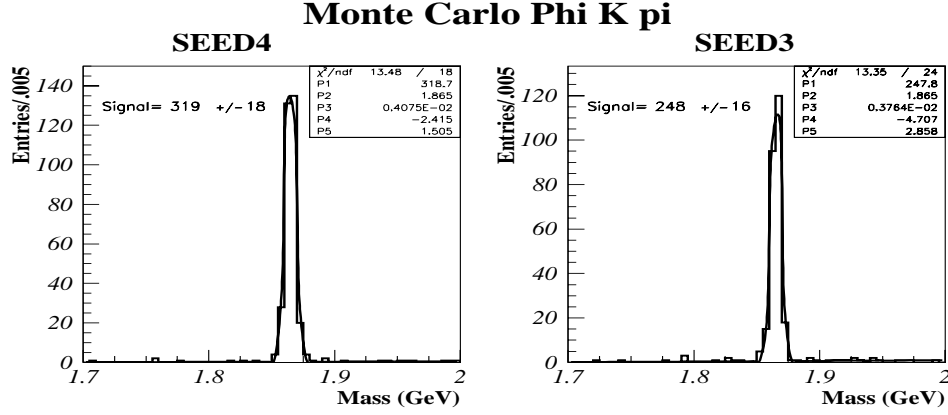


Figure 5.2: SEED4 (left) and SEED3 (right) mass histograms made by running $D^0 \rightarrow K^- K^- K^+ \pi^+$ analysis algorithm on Monte Carlo $D^0 \rightarrow \phi K^- \pi^+$; $\phi \rightarrow K^- K^+$ data with final cuts.

To look into this matter, 500,000 (250,000 in each charge state) Monte Carlo $D^0 \rightarrow \phi K^- \pi^+$; $\phi \rightarrow K^- K^+$ were generated and the relative efficiency of the detector was recalculated using those data. Fig. 5.2 show the SEED4 (left) and SEED3 (right) histograms made by running the $D^0 \rightarrow K^- K^- K^+ \pi^+$ algorithm on $D^0 \rightarrow \phi K^- \pi^+$; $\phi \rightarrow K^- K^+$ data with the optimized cuts. Table 5.12 shows the number of signal events obtained by fitting these mass histograms along with the number of signal events obtained from non resonant $D^0 \rightarrow K^- K^- K^+ \pi^+$ fits (Figs. 4.26 and 4.27 and Table 5.2).

The SEED4 and SEED3 signal event summation of the resonant decay, S' and that for non-resonant decay, S are thus given by (Table 5.12),

	$D^0 \rightarrow K^- K^- K^+ \pi^+$	$D^0 \rightarrow \phi K^- \pi^+; \phi \rightarrow K^- K^+$
SEED4	299 ± 18	319 ± 18
SEED3	295 ± 18	248 ± 18

Table 5.12: Number of signal events obtained by fitting the mass histograms made by running the $D^0 \rightarrow K^- K^- K^+ \pi^+$ analysis algorithm on Monte Carlo $D^0 \rightarrow K^- K^- K^+ \pi^+$ data and $D^0 \rightarrow \phi K^- \pi^+; \phi \rightarrow K^- K^+$ data.

$$S' = (319 \pm 18) + (248 \pm 18) = 567 \pm 25 \quad (5.28)$$

$$S = (299 \pm 18) + (295 \pm 18) = 594 \pm 25 \quad (5.29)$$

Thus,

$$|S' - S| = 27 \pm 35 \quad (5.30)$$

This shows that S and S' are consistent within statistical errors. Further, we have already taken the systematic error caused by the statistical fluctuations in Monte Carlo data in to consideration; therefore, the difference shown in here due to statistical fluctuations should not count as another source of systematic uncertainty. Hence, we conclude that the systematic error caused by ignoring $D^0 \rightarrow \phi K^- \pi^+; \phi \rightarrow K^- K^+$ in the calculation of the relative efficiency of the detector is insignificant compared to that due to the statistical fluctuations in Monte Carlo data.

5.2.6 In Summary

Table 5.13 summarizes correction factors to the relative efficiency calculated with Monte Carlo data for reconstructing $KKK\pi$ and $K\pi\pi\pi$ final states. The relative efficiency used for determining the relative branching ratio, $\epsilon_{KKK\pi}/\epsilon_{K\pi\pi\pi}$, will be 0.85 times that found from the Monte Carlo. The total correction factor has been obtained by multiplying the individual correction factors. Table 5.14 summarizes all the factors that contribute significantly to the systematic errors and their contributions. The total systematic uncertainty which is 13% has been estimated by adding each individual contribution in quadrature.

systematic variation due to	raise $\epsilon_{KKK\pi_{rel}}$ by	correction factor
kaon Čerenkov efficiency	-18%	0.82
SEED4 and SEED3 fractions	+2.5%	1.025
SDZ cut	+1.1%	1.011
PTBL cut	+0.5%	1.005
total correction factor	-15%	0.85

Table 5.13: Summary of corrections to the relative efficiency from Monte Carlo for reconstructing $KKK\pi$ and $K\pi\pi\pi$ final states. The relative efficiency used for determining the relative branching ratio, $\epsilon_{KKK\pi}/\epsilon_{K\pi\pi\pi}$, will be 0.85 times that found from the Monte Carlo. The total correction factor has been calculated by multiplying the individual correction factors.

difference in Monte Carlo and real data:	
kaon Čerenkov efficiency	10%
tracking and vertexing efficiencies	5%
SEED4 and SEED3 fractions	1.8%
SDZ cut	1.1%
PTBL cut	0.5%
sub total	11.4%
statistical fluctuations in Monte Carlo data	4.7%
Signal and Background Shape	4.3%
FOM predictions	1.5%
$D^0 \rightarrow \phi K^- \pi^+; \phi \rightarrow K^- K^+$	within statistical fluctuations
total (added in quadrature)	13%

Table 5.14: Summary of systematic errors. The total has been calculated by adding the individual contributions in quadrature.

5.3 KK Resonance

Some of the $D^0 \rightarrow K^- K^- K^+ \pi^+$ decay events might have actually come from the $D^0 \rightarrow \phi K^- \pi^+; \phi \rightarrow K^- K^+$ resonance decay. This was studied by reconstructing the $K^- K^+$ masses from $D^0 \rightarrow K^- K^- K^+ \pi^+$ decays. Each $D^0 \rightarrow K^- K^- K^+ \pi^+$ decay

has two kaons with equal charge and one with the opposite charge; thus, one event has two possible K^-K^+ combinations. The algorithm reconstructed both combinations.

Fig. 5.3 shows the K^-K^+ mass histograms constructed from real data (top plots), $D^0 \rightarrow \phi K^- \pi^+; \phi \rightarrow K^- K^+$ Monte Carlo data (bottom left), and $D^0 \rightarrow K^- K^- K^+ \pi^+$ non-resonant Monte Carlo data (bottom right). The bottom plots and the top left plot have been made with the events from $KKK\pi$ signal region ($1.855 < M_{KKK\pi} < 1.875$) while the plot on the top right has been made with event from $KKK\pi$ real data background region (*i.e.* all the events outside the signal region). The histogram from $D^0 \rightarrow K^- K^- K^+ \pi^+$ non-resonant Monte Carlo data was made to make sure that the algorithm did not create a false KK signal out of non-resonant decay events.

The top left histogram of Fig. 5.3 shows clear evidence of the KK signal (*i.e.* the evidence of $D^0 \rightarrow \phi K^- \pi^+; \phi \rightarrow K^- K^+$). A toy model was used to roughly estimate the number of $D^0 \rightarrow K^- K^- K^+ \pi^+$ events that actually came from $D^0 \rightarrow \phi K^- \pi^+; \phi \rightarrow K^- K^+$ resonance decay. Fig. 5.4 shows the plots that were used to make this estimate. In this estimation, the area of the KK mass distribution that came from $D^0 \rightarrow K^- K^- K^+ \pi^+$ background events was normalized to 2×4.5 ; 4.5 is the number of background events we observed under the $KKK\pi$ real data signal

(Fig. 5.1) and 2 comes about since we constructed two KK combinations from one $KKK\pi$ event. The area of the the KK mass distributions that came from Monte Carlo $D^0 \rightarrow \phi K^- \pi^+; \phi \rightarrow K^- K^+$ and Monte Carlo non-resonant $D^0 \rightarrow K^- K^- K^+ \pi^+$ were normalized to $2 \times x \times 18.4$ and $2 \times (1 - x) \times 18.4$ respectively; 18.4 is the total number of $KKK\pi$ signal events observed and x is the fraction of resonance decay signal events that might be in the total signal. the estimation was done for three value of x : .3, .6, and .9. The top right, bottom left, and bottom right plots of Fig. 5.4 show the corresponding plots respectively.

In these plots, all three scaled KK mass distributions: the distributions that came from $D^0 \rightarrow K^- K^- K^+ \pi^+$ real data background events, non-resonant $D^0 \rightarrow K^- K^- K^+ \pi^+$ Monte Carlo signal events, and resonant $D^0 \rightarrow \phi K^- \pi^+; \phi \rightarrow K^- K^+$ Monte Carlo signal events have been plotted cumulatively (*i.e.* adding one after the other; not superimposing). The plot on top left show the KK mass distribution for real data. Fig. 5.5 shows the real data mass distribution overlapped on the toy model mass distributions for comparison. Plots with higher background levels were also tried, but they did not seem to improve the modeling. From these plots, one may conclude that about $(60 \pm 30)\%$ of $D^0 \rightarrow K^- K^- K^+ \pi^+$ events come from $D^0 \rightarrow \phi K^- \pi^+; \phi \rightarrow K^- K^+$ resonance decay; given the statistics of this experiment, this estimate can not be precise.

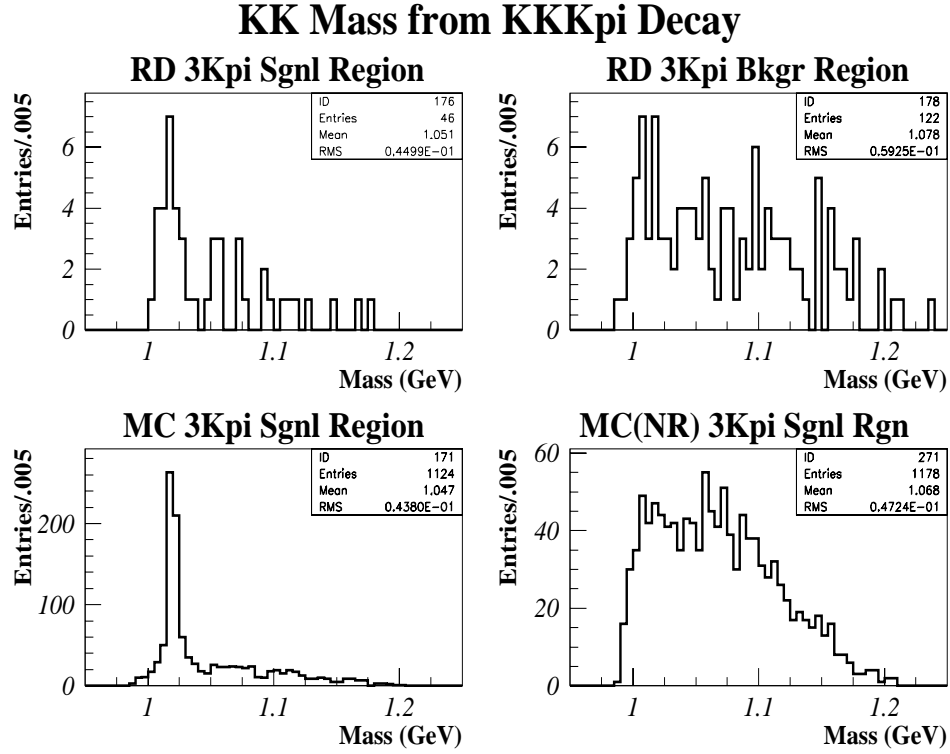


Figure 5.3: KK mass histograms from $KKK\pi$ decays. The histograms were made from real data (top plots), $D^0 \rightarrow \phi K^- \pi^+$; $\phi K\pi$ Monte Carlo data (bottom left), and non-resonant $D^0 \rightarrow K^- K^- K^+ \pi^+$ Monte Carlo data (bottom right). The events for the bottom plots and the top left plot came from $KKK\pi$ signal region ($1.855 < M_{KKK\pi} < 1.875$) while those for the top right histogram came from $KKK\pi$ background region.

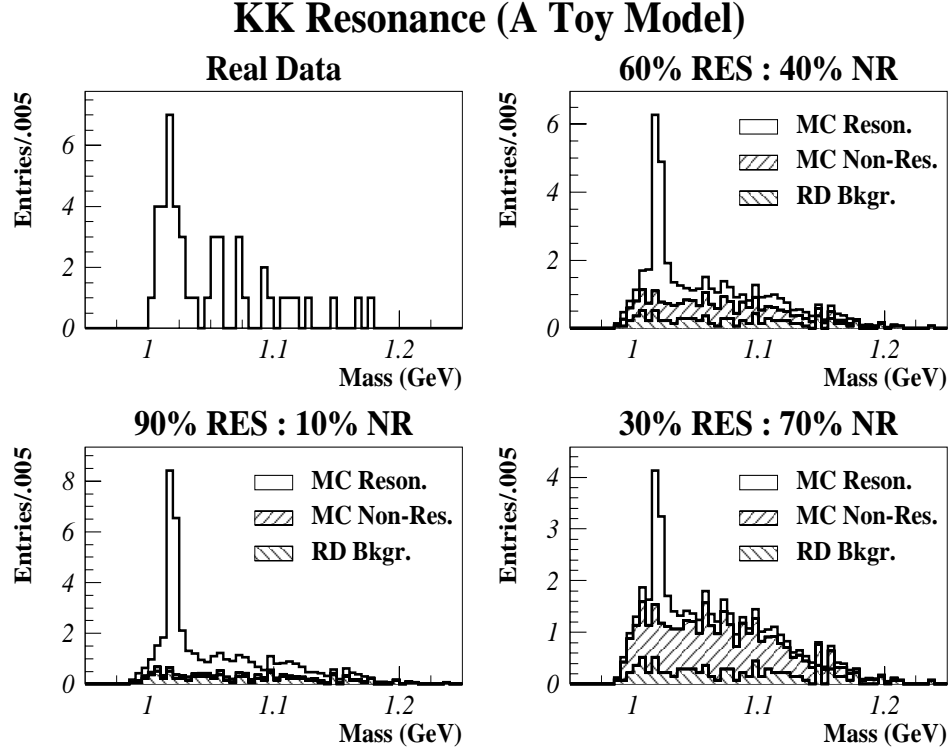


Figure 5.4: KK mass distribution from real data and that from a toy model. The top right, bottom left, and bottom right plots corresponds to signal events from resonant $D^0 \rightarrow \phi K^- \pi^+; \phi \rightarrow K^- K^+$ and non-resonant $D^0 \rightarrow K^- K^- K^+ \pi^+$ decay with the ratios 60%:40%, 90%:10%, and 30%:70% respectively. These three plots contain KK scaled mass distributions from $KKK\pi$ real data background, Monte Carlo $D^0 \rightarrow \phi K^- \pi^+; \phi \rightarrow K^- K^+$ signal, and Monte Carlo non-resonant $D^0 \rightarrow K^- K^- K^+ \pi^+$ signal events.

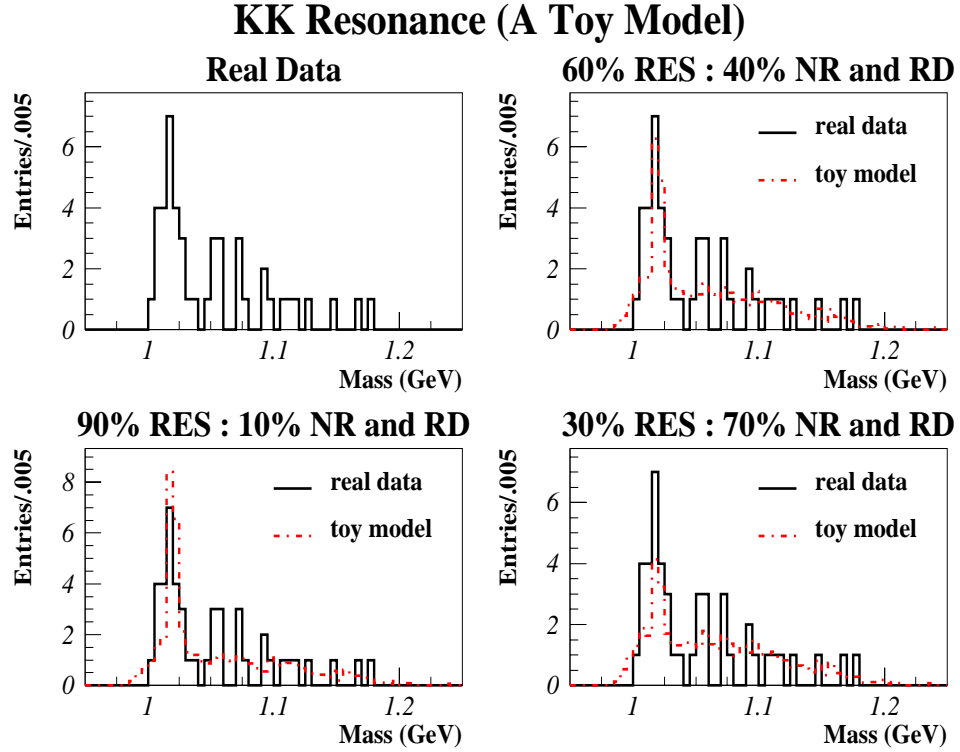


Figure 5.5: KK mass distribution from real data and that from a toy model. The top right, bottom left, and bottom right plots corresponds to signal events from resonant $D^0 \rightarrow \phi K^- \pi^+; \phi \rightarrow K^- K^+$ and non-resonant $D^0 \rightarrow K^- K^- K^+ \pi^+$ decay with the ratios 60%:40%, 90%:10%, and 30%:70% respectively. These three plots contain real data mass distribution (solid lines) superimposed over the toy model mass distributions (dashed lines).

Chapter 6

Conclusions

From the analysis described in this thesis, the branching ratio of the $D^0 \rightarrow K^- K^- K^+ \pi^+$ decay relative to the normalization channel $D^0 \rightarrow K^- \pi^- \pi^+ \pi^+$, before corrections to the systematic variation in relative efficiency, is estimated to be,

$$\frac{\mathcal{B}(D^0 \rightarrow K^- K^- K^+ \pi^+)}{\mathcal{B}(D^0 \rightarrow K^- \pi^- \pi^+ \pi^+)} = 0.0046 \pm 0.0013 \quad (6.1)$$

where the uncertainty is that only due to statistical fluctuations. When the 15% correction to the systematic variations in the relative efficiency is applied and 13% systematic uncertainty is included, the final result for the branching ratio of $D^0 \rightarrow K^- K^- K^+ \pi^+$ decay relative to $D^0 \rightarrow K^- \pi^- \pi^+ \pi^+$ decay becomes,

$$\frac{\mathcal{B}(D^0 \rightarrow K^- K^- K^+ \pi^+)}{\mathcal{B}(D^0 \rightarrow K^- \pi^- \pi^+ \pi^+)} = (0.54 \pm 0.13 \pm 0.07)\% \quad (6.2)$$

where the first and second uncertainties are statistical and systematic. The measurement from Fermilab E687 experiment is $(0.28 \pm 0.07 \pm 0.01)\%$ [7]. The difference between this result and the E687 result is $(0.26 \pm 0.16)\%$, so the two results are consistent with being the same. The fractional errors for the two measurements are 0.27 (this work) and 0.25 (E687) where the statistical and systematic errors have been added in quadrature.

With the Particle Data Group value for the branching ratio of $D^0 \rightarrow K^- \pi^- \pi^+ \pi^+$, $\mathcal{B}(D^0 \rightarrow K^- \pi^- \pi^+ \pi^+) = (7.6 \pm 0.4)\%$, the branching ratio of $D^0 \rightarrow K^- K^- K^+ \pi^+$ decay turns out to be (including all the errors),

$$\mathcal{B}(D^0 \rightarrow K^- K^- K^+ \pi^+) = (0.041 \pm 0.011)\% \quad (6.3)$$

which is again consistent within 2σ level with the current PDG value, which is $(0.021 \pm .005)\%$ and comes from the E687 results.

As shown in Fig. 1.3, one can get a Feynman diagram of the $D^0 \rightarrow K^- K^- K^+ \pi^+$ decay when the right light quark pair of a $K\pi\pi\pi$ decay diagram is replaced by an $s\bar{s}$ pair. On this ground, one can assume that all the terms except the terms related to

phase space and the probability of the vacuum popping up either an $s\bar{s}$ or a light quark pair cancel out in the expression for the ratio of branching ratio of $D^0 \rightarrow K^- K^- K^+ \pi^+$ and $D^0 \rightarrow K^- \pi^- \pi^+ \pi^+$. This is to say that,

$$\frac{\Omega_{KKK\pi}}{\Omega_{K\pi\pi\pi}} = \frac{\Omega_{KKK\pi}}{\Omega_{K\pi\pi\pi}} \times R \quad (6.4)$$

where $\Omega_{KKK\pi}$ and $\Omega_{K\pi\pi\pi}$ stand for the the phase space integral for $D^0 \rightarrow K^- K^- K^+ \pi^+$ and $D^0 \rightarrow K^- \pi^- \pi^+ \pi^+$ respectively, and R is the factor related to the probabilities of the vacuum popping up either an $s\bar{s}$ pair or a light quark pair.

With an existing algorithm that calculates the phase space integrals, the ratio of $\Omega_{KKK\pi}$ and $\Omega_{K\pi\pi\pi}$ has been found to be $\Omega_{KKK\pi}/\Omega_{K\pi\pi\pi} = 0.0077/0.5372$. With this result in Eqn. 6.4, one can make an hand-waving estimate of R to be,

$$R = 0.321 \pm 0.093 \quad (6.5)$$

If we go one step further and factorize R as

$$R = \frac{P_{s\bar{s}}}{P_{u\bar{u}/d\bar{d}} + P_{NoPop}} \quad (6.6)$$

where $P_{s\bar{s}}$, $P_{u\bar{u}/d\bar{d}}$, and P_{NoPop} respectively come from the $D^0 \rightarrow K^- K^- K^+ \pi^+$ terms that pop an $s\bar{s}$ pair out of the vacuum, corresponding $D^0 \rightarrow K^- \pi^- \pi^+ \pi^+$ terms that

pop either a $u\bar{u}$ or a $d\bar{d}$ pair, and $D^0 \rightarrow K^-\pi^-\pi^+\pi^+$ terms that do not show such corresponding $q\bar{q}$ creation. Since we have already taken the phase space differences into consideration, we may assume that $P_{s\bar{s}} \approx P_{u\bar{u}/d\bar{d}} = P_{q\bar{q}}$. With this assumption and Eqns. 6.6 and 6.5 we get,

$$R = 0.321 = \frac{P_{q\bar{q}}}{P_{q\bar{q}} + P_{NoPop}} \quad (6.7)$$

which —when rearranged— gives,

$$\frac{P_{q\bar{q}}}{P_{NoPop}} = 0.47 \quad (6.8)$$

If we go to two other extremes by replacing $P_{u\bar{u}/d\bar{d}}$ by $2P_{q\bar{q}}$ and 0 we get,

$$\frac{P_{q\bar{q}}}{P_{NoPop}} = 0.90 \quad \text{and} \quad \frac{P_{q\bar{q}}}{P_{NoPop}} = 0.32 \quad . \quad (6.9)$$

From these numbers we can conclude that $P_{q\bar{q}}/P_{NoPop}$ is between 30% and 90%.

There is also clear evidence of $D^0 \rightarrow \phi K^-\pi^+; \phi \rightarrow K^-K^+$. About $(60 \pm 30)\%$ of the $D^0 \rightarrow K^-K^-K^+\pi^+$ decay events seem to come from $D^0 \rightarrow \phi K^-\pi^+; \phi \rightarrow K^-K^+$, but there are not enough statistics to make a precise estimate.

Appendix A

Sphericity

Sphericity is essentially a measure of the summed p_T^2 w.r.t. the Direction of Sphericity which is the one around which the summed p_T^2 is a minimum. Sphericity and its direction are calculated using the Sphericity Tensor which is defined by,

$$S^{\alpha\beta} = \frac{\sum_i p_i^\alpha p_i^\beta}{\sum_i p_i^2}$$

where p_i is the momentum of the i^{th} daughter track. α and $\beta = 1, 2$ and 3 corresponding to x, y and z components. By diagonalizing S, one can find the eigen values; $\lambda_1 > \lambda_2 > \lambda_3$ and the corresponding eigen vectors; σ_1, σ_2 and σ_3 of S. By construction,

$$\lambda_1 + \lambda_2 + \lambda_3 = 1$$

The direction of σ_1 , which is the eigen vector with the highest eigen value, is defined as the Direction of Sphericity¹. The Sphericity of the event is defined by,

$$S = \frac{3}{2}(\lambda_2 + \lambda_3)$$

that has the range $0 < S < 1$.

If $\lambda_1 = 1$ then $S = 0$, which implies that σ_i 's and hence the event have the least Sphericity. On contrary, if $\lambda_1 = \lambda_2 = \lambda_3 = 1/3$, then $S = 1$, which implies the maximum sphericity.

¹This is also referred to as Sphericity Axis or Event Axis.

Appendix B

Kaon Čerenkov Efficiencies

Table B.1 shows the kaon Čerenkov efficiencies at $\text{CVK} > 0.2$ for a set of p and p_T ranges. These values have been obtained from $D^0 \rightarrow K^- \pi^+$ and $D^0 \rightarrow K^- \pi^- \pi^+ \pi^+$ real data. Reference [23] gives a complete list of kaon Čerenkov efficiencies for the E791 experiment.

p (GeV)	p_T (GeV)		
	< 0.50	$0.50 - 0.75$	> 0.75
< 10	62.7%	50.5%	36.5%
10 - 14	78.8%	81.6%	81.5%
14 - 18	80.0%	91.3%	92.3%
18 - 22	71.5%	78.7%	93.7%
22 - 26	62.0%	72.2%	84.6%
26 - 30	63.8%	70.3%	74.3%
30 - 34	60.5%	71.7%	72.1%
34 - 38	59.2%	62.8%	65.8%
38 - 42	49.6%	54.7%	61.2%
42 - 46	53.0%	47.4%	47.6%
46 - 51	48.6%	45.6%	43.7%
51 - 56	33.6%	41.2%	36.7%
56 - 62	32.0%	31.2%	29.5%
68 - 68	22.2%	20.6%	23.0%
68 - 74	17.3%	19.5%	16.4%
> 74	13.3%	11.4%	14.1%

Table B.1: Kaon Čerenkov efficiencies at $\text{CVK} > 0.2$ for a set of p and p_T ranges. These values have been obtained from $D^0 \rightarrow K^- \pi^+$ and $D^0 \rightarrow K^- \pi^- \pi^+ \pi^+$ real data.

Bibliography

- [1] D. Griffiths, *Introduction to Elementary Particles*, John Wiley and Sons, Inc. (1987).
- [2] S. A. Bludman, *Nuovo Cimento* **9**, 443 (1958).
- [3] F. J. Hasert et al. *Phys. Lett.* **46B**, 138 (1973); *Nucl. Phys.* **B73**, 1 (1974).
- [4] N. Cabibbo, *Phys. Rev.* **10**, 531 (1963).
- [5] S. L. Glashow, J. Iliopoulos, and L. Maiani, *Phys. Rev.* **D2**, 1585 (1970).
- [6] M. Kobayashi and K. Maskawa, *Prog. Theor. Phys.* **49**, 652 (1973).
- [7] P. L. Frabettin et al, *Phys. Lett.* **B354** 486 (1995), *Fermilab-Pub-95/114-E*
- [8] E769 Collaboration, G. A. Alves et al. Atomic Mass Dependence of D^\pm and $D^0 \bar{D}^0$ production in 250 GeV π^\pm Nuclear Interactions. *Phys. Rev. Lett.* **70:1** (1993).

- [9] Carrol et al, Absorption cross section of π^\pm , K^\pm , p , and \bar{p} on nuclei between 60 and 280 GeV. *Phys. Lett.* **B80:319** (1979).
- [10] J. Dinkel et al, *Nuclear Instruments and Methods A138*, **567** (1976)
- [11] D. Bartlett et al, Performance of the Čerenkov Counters at the Fermilab Tagged Photon Spectrometer Facility, *Nuclear Instruments and Methods in Physics Research A260* **55** (1987)
- [12] V. K. Bharadwaj et al, *Nuclear Instruments and Methods A228* **361** (1985)
- [13] J. A. Appel et al, *Nuclear Instruments and Methods A243* **361** (1986)
- [14] S. Amato et al, *Nuclear Instruments and Methods A324* **535** (1993)
- [15] E791 offline document 239, S. Bracker et al, *Nuclear Instruments and Methods* (1995)
- [16] E791 offline document 115, A. Tripathi
- [17] E791 offline document 140, P. Kasper
- [18] E791 offline document 263, A. Schwartz
- [19] Pythia 5.7 and Jetset 7.4 *Physics Manual*, *CERN-TH-7112/93* (1993)

- [20] Louis Lyons, *Statistics for Nuclear and Particle Physicists*, Cambridge University Press, (1989).
- [21] W. R. Leo, *Techniques for Nuclear and Particle Physics experiments*, Springer-Verlag **34** (1992)
- [22] E791 offline document, M. Purohit
- [23] E791 offline documnet 333, S. Kwan
- [24] E. M. Aitala et al, *Phys. Lett.* **B462** 225-236 (1999), *FERMILAB-PUB-99-185-E*
16pp (June 1999)